Electrophoretic deposition (EPD) of functional metal oxide nano/micro-structures for VOC sensor devices

by

Yoonsung Chung

A dissertation submitted to the Graduate Faculty of
Auburn University
in partial fulfillment of the
requirements for the Degree of
Doctor of Philosophy

Auburn, Alabama
August 6, 2016

Keywords: Electrophoretic deposition, ZnO hollow microsphere, NiO film, gas sensor, flexible substrate

Copyright 2016 by Yoonsung Chung

Approved by

Dong-Joo Kim, Chair, Professor of Materials Engineering
Bart Prorok, Professor of Materials Engineering
ZhongYang Cheng, Professor of Materials Engineering
Dongye Zhao, Professor of Civil/Environmental Engineering

Abstract

In this dissertation, two nano/micro-structured functional metal oxides, ZnO and NiO, were synthesized by a simple hydrothermal and precipitation method. Synthesized particles were then electrophoretically deposited as a film and used as sensing materials for sensor applications. Based on the fundamental study of the electrophoretic deposition (EPD) process, this study explored an optimized process condition for improved deposition rate and properties of deposits, and this condition was compared with the empirical equations. The researcher further studied the selection of adequate solvent and additives to achieve a stable suspension by DC/AC EPD with aqueous suspension and a mixture of water and ethanol suspensions. Also, this study explored process conditions with flexible substrates, such as metallic or metal coated fiber, carbon fabric, and carbon papers, to improve deposition rate and properties of deposits, and these conditions were compared with the empirical equation. The effect of frequency on the kinetics of AC-EPD was investigated with ZnO in aqueous suspensions and ethanol suspensions.

Different morphologies of ZnO and NiO, such as cubes, rods, and flakes, and hollow microspheres, were used to grow nano/micro-structured materials in order to fabricate highly sensitive and selective VOC sensor devices. Also, this study explored the synthesis of ZnO by the precipitation method at low temperatures with controlling morphology to apply the in-situ EPD process. Synthesized ZnO and NiO materials were characterized by FE-SEM, TEM, XRD, EDS, DSC, FT-IR, BET, zeta potential analyzer, impedance analyzer, and Keithley 2400 source

meter to examine the surface morphology, crystalline phase, atomic composition, chemical bonding, and electrical resistance change.

Gas sensing properties of nanostructured metal oxides were studied with different morphologies. Three different gases (ethanol, acetone, and ammonia) mixed with synthetic air were tested in a closed chamber by continuously flowing gases. ZnO and NiO films were electrophoretically deposited from synthesized particles on gas sensing properties. Geometric effects of the oxides on the gas sensing properties were investigated by inducing additives or surfactants. ZnO hollow microspheres were prepared by a simple precipitate method by inducing sodium citrate. Different morphologies of NiO were synthesized by a simple hydrothermal method using triethanolamine. Higher specific area of particles appeared to be a dominant factor for gas sensing applications. In addition to controlling the selectivity and sensitivity, silver nanoparticles as a metallic catalyst were decorated on ZnO hollow microspheres.

Acknowledgments

First and foremost I wish to express my gratitude to my advisor, Dr. Dong-Joo Kim. I could not have completed this work without his invaluable encouragement and support. I appreciate all his contributions of time and ideas to help me pursue a Ph. D. Not only did his mentorship improve by academic and research performance, but he also advised me as an elder in life. He is one of my role models in science and my research field. I also would like to acknowledge my dissertation committee members, Dr. Bart Prorok, Dr. Zhongyang Cheng, Dr. Dongye Zhao, and Dr. Minseo Park, for their valuable suggestions and guidance.

I would like to show thanks to my group alumni and members, Dr. Hosang Ahn, Dr. Seon-Bae Kim, Dr. Hyejin Park, Dr. Seokhee Lee, Ms. Eunji Lee, Mr. Soohyun Ahn, Mr. Doohee Lee, and Mr. Christopher Lincoln, for their co-work and help through all these years. I especially thank Mr. Steve Moore for a great deal of help during the experiments. My time at Auburn University was made enjoyable in large part due to my friends that became a part of my life. Thank you to Doyoung Kim, Dr. Min Hea Kim, Dr. Seul Gi Park, and Dr. Young Suk Choi for their friendship and support.

Lastly, I would like to give appreciation to my parents, Dong-Ho Chung and Bok-Sun Lee; my sister, Ji-Yun Chung; and my brother, Baek-Gwang Chung. Although the distance between them and me is far, the love and support of my family sustained me during my study. I could have not reached this point without my family. Thank you so much and I love you.

Table of contents

List of tables

List of figures

List of abbreviations

EPD Electrophoretic Deposition

VOC Volatile Organic Compound

DC Direct Current

AC Alternative Current

EDL Electrical Double Layer

PDC Pulsed Direct Current

CDC Continuous Direct Current

ELD Electrolytic Deposition

IEP Isoelectric Point

ZnO Zinc Oxide

NiO Nickel Oxide

PEI Polyethyleneimine

HMT Hexamethylenetetramine

TEA Trethanolamine

SSP Stainless Steel Plates

FE-SEM Field Emission- Scanning Electron Microscopy

TEM Transmission Electron Microscopy

XRD X-Ray Diffraction

EDS Energy Dispersive X-ray Spectroscopy

FTIR Fourier Transform Infrared Spectroscopy

DSC Differential Scanning Calorimetry

UV-vis DRS Ultraviolet-Visible Diffuse Reflectance Spectroscopy

PL Photoluminescence

BET Brunauer–Emmett–Teller

RF Radio Frequency

MFC Mass Flow Controller

Chapter 1. Introduction

1.1 Motivation and research background

The controlled structure and function of materials at the nanoscale are continuously being explored due to their great potential for a wide range of applications, such as energy conversion devices, electronic components, data storage devices, biosensors and biomedical applications [1, 2]. As a method to build nanostructures, electrophoretic deposition (EPD) is attractive due to various advantages, such as its being a simple deposition process with low cost equipment, high versatility for coating diverse materials, less restriction on the substrate's shape, and easy control of the thickness and the microstructure of the deposited layer [3-5]. Uniform coating of electrophoretically deposited materials has been demonstrated on three-dimensional, porous, and even flexible substrates [4-6]. Some researchers have reported applying EPD to coat metal oxides on flat and hard substrates, but few studies have focused on coating functional oxides on fabrics. As the wearable electronics industry develops, methods to embed or coat nanostructured functional materials can be crucial for realizing diverse functions in wearable devices [7-9]. Semiconducting nano-scale metal oxides such as tin oxide [10], zinc oxide [1], nickel oxide [11], and copper oxide [12] have been developed as gas sensors that measure changes in electrical conductivity upon exposure to the gas. Since the properties of semiconducting metal oxide gas sensors are strongly related to surface reactions, parameters such as chemical components, surface modification and microstructures of sensing layers, and temperature can influence the sensing properties. Numerous researchers have investigated techniques to enhance the selectivity

and sensitivity of gas sensors and to lower operation temperature. Chemical components have been modified by doping elements such as noble metals and transition metals to enhance the gas sensitivity. Microstructures of sensing layers have been manipulated by varying nanostructures such as nanorods, nanowires, and nanotubes to achieve higher specific surface area [1, 13-15]. Recent research has focused on hierarchical nanostructured oxides, more complicated structures to fully utilize surface area [16-18]. Some researchers have explored the lowering of the operation temperature by modifying both structure and composition because metal oxide gas sensors are potentially limited in usefulness for portable and wearable applications.

1.2 Research objectives

1.2.1 Development of EPD for an environmentally friendly process

A crucial parameter for EPD is the selection of adequate solvent and additives to achieve a stable suspension. While water has many advantages as a medium, its usefulness is restricted due to the electrolysis of water, which can cause poor deposition due to bubbling [5]. This research studies approaches to using an aqueous suspension system to achieve a stable suspension for EPD, specifically to increase deposition rates and modify deposition layers. Organic solvents are widely used in the EPD process in order to avoid the electrolysis of water. However, water is still a favorable solvent because of low cost and low required electrical potential. Also, because the H^+ and OH^- ions created by electrolysis of water can act as a surfactant [19], using water can reduce the effect from impurities without polymer additives. Thus, some studies have suggested a mixture of organic solvent and water systems. In this study, a mixture of water and ethanol is used as a solvent and zinc oxide nanoparticles are explored as starting materials. Zinc oxide is studied and used on sensor platforms. Based on the fundamental study of the EPD process, an

optimized process condition is explored for improved deposition rate and properties of deposits, and this process condition is compared with two empirical equations, the Hamaker equation [20] and Zhang's equation [21]. Also, several research groups have used alternating current (AC) to deposit from aqueous suspensions [22, 23]. Thus, pure water suspensions as well as a mixture of ethanol and water suspensions are studied using AC electric fields.

1.2.2 Conductive and flexible substrates for EPD

One remarkable advantage of the EPD process is little restriction of substrate shapes [5]; it allows the use of three-dimensional, porous, and even flexible substrates [4, 5]. Also, the use of EPD to coat metal oxides on solid substrates has been extensively studied [24, 25], but few researchers have studied its use on nonconductive substrates. In addition, additives are used to improve the stability of suspensions and the property of coating layers [26, 27], but most such additives are polymers and heat treatment is required to remove them. However, heat treatment is not suitable for low temperature applications which use polymer, fabric, or fiber substrates. One of the limitations in the EPD process is the conductivity of substrates. Several approaches exist to using nonconductive materials as a working electrode, including supporting conductive layers, such as coating a metallic layer on glass [28], mounting glass fibers on a metal plate [29], coating polymer film on a metal plate [30]; or using a low frequency AC electric field [31, 32]. In order to apply the EPD process to wearable devices, flexible substrates, including various types of fibers or fabrics, are needed. However, most of the fundamental study of the EPD process is focused on using conductive solid substrates. Thus, this study explores process conditions with metallic or metal coated fiber to improve deposition rate and properties of deposits, and these process conditions are compared with the empirical equation by Hamaker.

Also, an AC electric field is applied to use nonconductive substrates for the EPD process. The results of this research will be helpful to predict the EPD process of using nonconductive and messy substrates.

1.2.3 Development of synthesis methods for ZnO and NiO

A number of researchers have studied ways to synthesize metal oxide nanostructures, including chemical [33-35], electrochemical [35, 36], and physical deposition techniques [37, 38]. Among many nanosized metal oxide preparation routes, a solution based synthesis method [34, 35] was chosen for this study. Since an important issue in synthesizing nanoparticles is preventing agglomeration of particles, a low processing temperature is preferred. Among metal oxides, diverse morphologies of ZnO crystal structures by the precipitation method are well known to be possible at relatively low processing temperatures [34, 35, 39]. In this work, synthesis of ZnO by a precipitation method and NiO by a hydrothermal method is studied with controlling morphology to apply the in-situ EPD process. Also, the effect of particle morphologies on the properties of deposited layers by EPD is studied.

1.2.4 Gas sensing properties of different morphologies of metal oxides

Recently, interest in wearable devices has increased significantly. A portable and wearable gas sensor system is one area of interest. Integration of fabric and gas sensors for a wearable breath monitoring system could monitor signature gases from patients' breath such as acetone, ammonia, or ethanol [40-42]. Therefore, a great demand exists for diverse sensing materials with good selectivity and sensitivity that could be integrated into wearable/flexible substances.

The sensitivity of gas sensors is significantly influenced by the morphology and structure of the sensing materials [43, 44]. Among various sensing materials, ZnO has been widely studied as an n-type semiconducting metal oxide because of its excellent electric properties. For ZnO gas sensors, researchers have investigated 1-D structures, such as nanorods, nanotubes, and nanowires, to understand morphology-driven properties. ZnO is easily formed as an anisotropic structure because it has a preferred growing direction along the c-axis. However, this study explores gas sensing properties of isotropic ZnO microspheres with porous and hollow structures which show an enhanced sensitivity due to large surface-to-volume ratio and reduced transport lengths for both mass and charge transport [45, 46]. Also, the catalytic effect of silver nanoparticles on ZnO porous and hollow microspheres is explored. Meanwhile, despite shortcomings of p-type gas sensors, they have attracted attention due to interest in forming p-n junction structures [43, 47]. NiO, which shows p-type semiconducting behavior, is a promising material. Although n-type gas sensing materials have been widely studied, the morphological effect on NiO gas sensors has not yet been intensively explored. Unlike ZnO, NiO grows with isotropic structure. However, this study explores gas sensing properties of different aspect ratios of NiO such as flakes, cubes, and rods.

1.3 Structure of dissertation

Chapter 1 outlines this dissertation, providing the motivation, research objectives, and dissertation structure.

Chapter 2 covers the background of this research: electrophoretic deposition, solution based synthesis methods of nanostructured metal oxide, and the use of nanostructured metal oxide for gas sensor applications.

Chapter 3 describes the details of experimental methods and explains the process of electrophoretic deposition, synthesis of nano/micro-structured metal oxide, material characterization, device preparation, and procedures to measure the gas sensing properties.

Chapter 4 describes the investigation of EPD for an environmentally friendly process and studies the EPD process for using water as a liquid medium.

Chapter 5 describes the EPD kinetics on various types of substrates, demonstrates the EPD process using nonconductive and flexible substrates, and examines the properties of electrophoretically deposited layers.

Chapter 6 investigates different morphologies of ZnO and NiO particles. It describes how the metal oxide particles were synthesized by a simple chemical solution method and characterizes their properties.

Chapter 7 investigates ZnO and NiO for the fabrication of flexible VOC sensor devices, the gas sensing properties of different morphologies of ZnO and NiO sensors, and the effect of silver as a catalyst to enhance sensitivity.

Chapter 9 summarizes the achievements of this study and future research directions that may further advance the field.

Chapter 2. Background and literature review

2.1 Electrophoretic deposition (EPD)

2.1.1 Mechanisms

Even though EPD has been steadily studied and successfully employed in various applications, its mechanisms are still not clearly understood [5, 48]. Briefly, EPD is a two-step process: a migration step in which the electric field is applied and a deposition step in which charge is lost at the electrode. Several researchers have explained the mechanism and phenomena of the EPD process. First, Hamaker and Verwey [49] suggested that deposition by EPD is similar to flocculation by particle accumulation under the applied electric field. The pressure derived by incoming particles overcomes the interparticle repulsion between deposited particles. This mechanism can explain deposition on porous membranes rather than electrodes.

According to Grillon *et al*. [50], particles are neutralized when they contact an electrode or deposit. This mechanism is feasible at the beginning of the process and in a very dilute suspension.

Koelmans [2, 5] suggested an electrochemical particle coagulation mechanism. According to this theory, the repulsive force between particles is reduced due to increasing electrolyte concentration near the electrode, so that Koelmans' mechanism is not valid without an increase in electrolyte concentration near the deposition electrode.

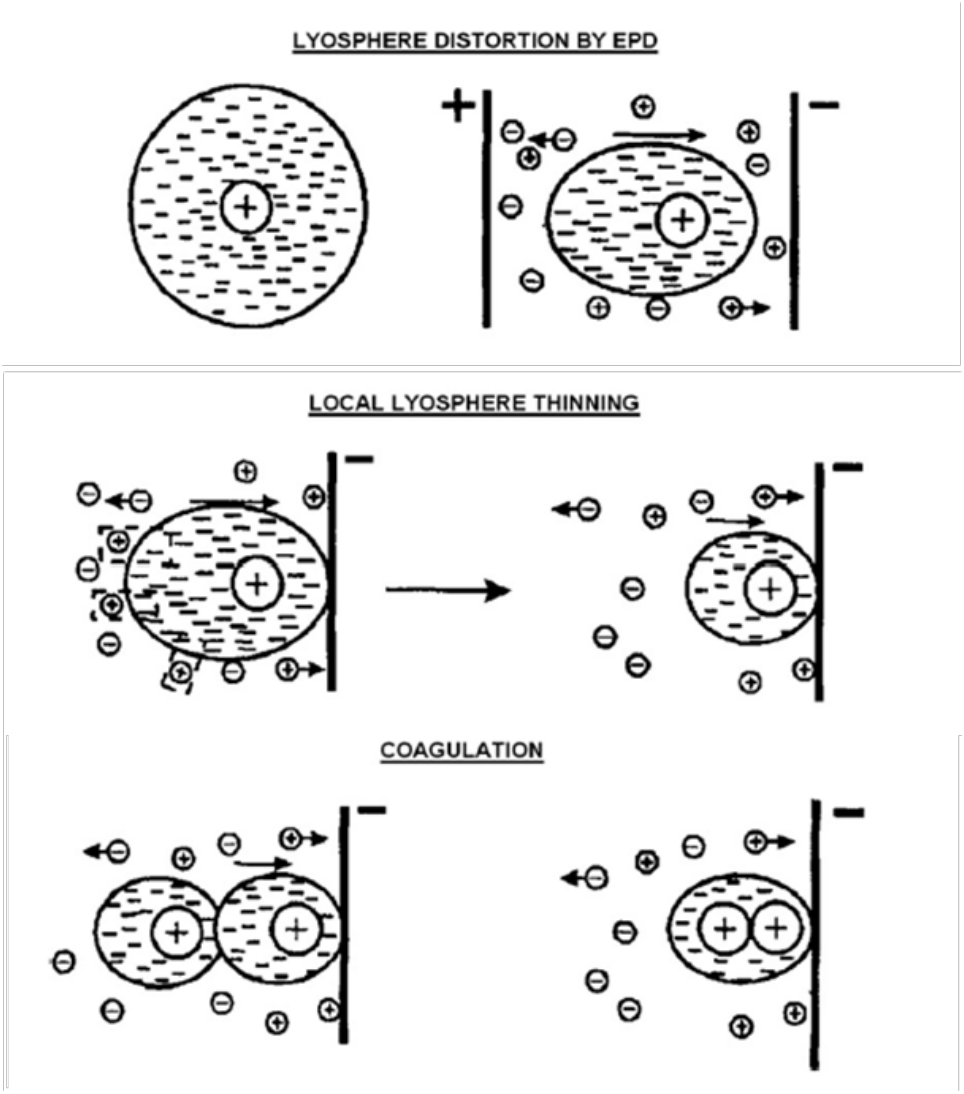

Figure 1. Electrical double layer distortion and thinning mechanism for electrophoretic deposition [51]

Sarkar and Nicholson [51] developed an electrochemical particle coagulation mechanism to explain the electrical double layer (EDL) distortion and thinning mechanism as shown in Figure 1. They employed the particle lyosphere system, in which a thin layer of liquid is formed around a charged colloidal particle, and considered the movement of a positively charged particle towards the cathode.

2.1.2 Kinetic models

Studying the kinetics of EPD is important in order to apply the EPD process to various applications. Some researchers have suggested semi-empirical models for describing the kinetics of EPD [20, 21, 52]. Hamaker's study [20] was the first attempt to study the relationship between the deposition yield and different influencing parameters for electrophoretic cells with planar geometry. The resulting Hamaker equation is a linear relationship between the deposited weight (W) and concentration of the suspension (C), electrophoretic mobility (μ), surface area of deposit (A), electric field (E), and deposition time (t), and can be described as follows:

$$W(t) = C\mu AEt \quad \text{(Equation 1)}$$

However, this model ignores the decrease of concentration of the suspension during the process, so that the model is only applicable at the beginning of deposition. In the early stage of the process, only a small number of particles are participated, but after significantly long periods, the concentration of the suspension decreases.

Zhang *et al*. [21] demonstrated the kinetic aspects of EPD through considering the change of suspension concentration without sedimentation, as shown in the following equation:

$$W(t) = W_0\left(1 - e^{-kt}\right) \text{ with } k = \frac{fA\varepsilon_0\varepsilon_r\xi E}{4\pi V\eta} \quad \text{(Equation 2)}$$

where W_0 is the starting weight of the particles in the suspension, k is the kinetic constant, t is deposition time, f is the efficiency factor (if all the particles near the electrode are involved in the formation of the deposit, then $f = 1$), $(\varepsilon_0\varepsilon_r)$ is permittivity, ξ is zeta potential, E is electric field, V is volume of suspension, and η is viscosity. However, the shielding effect of the growing layer is ignored in this model.

Although most empirical studies have focused on the EPD process under potentiostatic or constant-voltage conditions, some studies have suggested using galvanostatic or constant-current

conditions during the EPD process to avoid the effect of increased deposit resistivity of the effective electrical force acting on particles. In this condition, while the voltage drop across the two electrodes increases with time, the voltage/unit distance in the suspension is constant. This condition was proposed experimentally by Ma and Cheng [52]. The relationship between the kinetics parameter and the applied current intensity is determined as follows:

$$k = k_0\left(e^{i/i_0} - 1\right) \quad \text{(Equation 3)}$$

where i is the current density and i_0 and k_0 are the reference conditions from which the expression predicts the kinetics constant under other applied currents, facilitating more effective modelling and controlling of the process.

Table 1. Summary of kinetic equations and experimental expressions

Kinetics milestones	Experimental expressions	Eq.	Ref.
Basic equation	$W(t) = C\mu AEt$	(1)	[20]
Considering the solid loading variation	$W(t) = W_0(1 - e^{-kt})$ with $k = \frac{fA\varepsilon_0\varepsilon_r\xi E}{4\pi V\eta}$	(2)	[21]
Experimental expression determining the variation of the kinetics parameter vs. the current applied	$k = k_0\left(e^{i/i_0} - 1\right)$	(3)	[52]

2.1.3 Types of EPD

Traditionally, EPD has been studied with organic suspensions, which show high quality coatings due to low conductivity, good chemical stability of the suspension, and no electrochemical reactions at the electrodes. However, organic solvents have disadvantages, including cost, volatility, toxicity, and flammability. In particular, the low dielectric constant of organic solvents

requires a high electric field to achieve enough electrophoretic mobility for the suspended particles.

EPD of aqueous system has been suggested an alternative because water is both more economical and more environmentally friendly. Furthermore, the high dielectric constant of water enables a deposition process with low electric fields. However, the main drawback to EPD of aqueous suspension is the electrolysis of water. The gas bubbles at the electrodes due to water electrolysis can be included in the coated layer and cause a poor quality deposit.

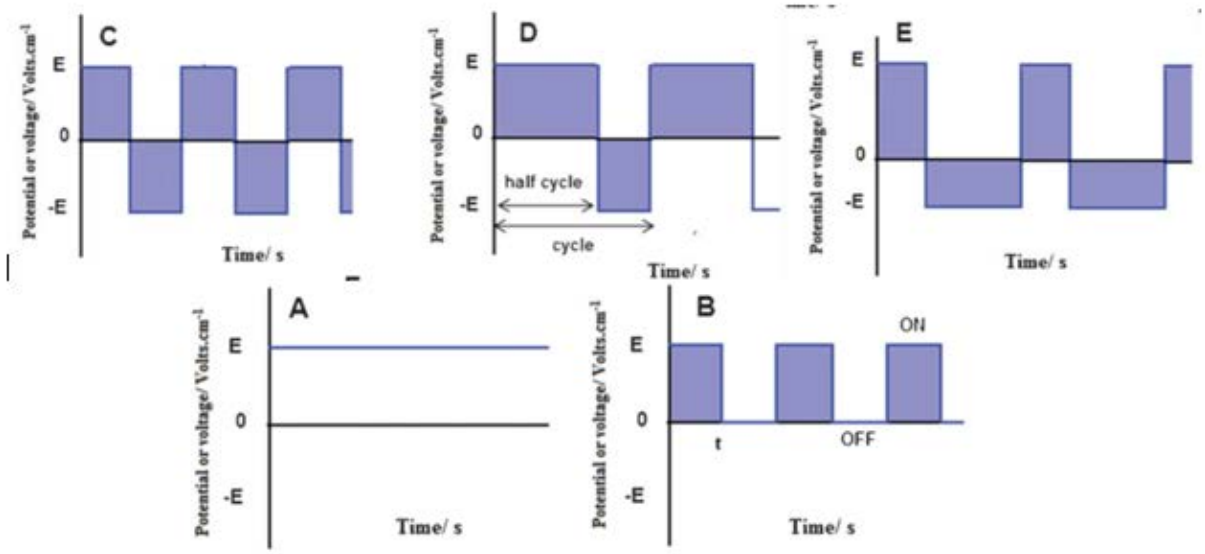

Figure 2. Schematic representation of some electrical signals: (A) continuous direct current (CDC), (B) pulsed direct current (PDC), (C) symmetrical alternating current (AC) with no net DC component, (D) asymmetrical AC signal with net DC component, and (E) asymmetrical AC wave with no net DC component [22].

In order to overcome this obstacle, several approaches have been proposed, such as the use of different substrates which are less vulnerable to gas bubbles, including palladium [25] and membrane [53] electrodes; low applied voltage [54]; or chemical additives [55]. However, the quality and homogeneity of the deposited layer are still poor. Recent research has focused on EPD using modulated electric fields [22], such as pulsed direct current (PDC) and alternating current (AC), that can decrease the number of gas bubbles at the electrodes and allow homogenous deposits from aqueous suspensions.

Figure 2 shows some examples of electric signals. As shown in Figure 2, while the voltage of continuous direct current (CDC) is roughly constant, that of PDC continually varies with a cycle. However, both a DC wave and a PDC wave have the same sign of the voltage. The advantages of PDC over CDC for EPD is that PDC reduces coalescence between gas bubbles and aggregations between particles. Bersa *et al*. controlled bubble incorporation and obtained bubble-free deposits from alumina aqueous suspensions by PDC-EPD [56]. Naim *et al*. demonstrated a aggregation/disaggregation of aqueous suspended polystyrene latex particles using PDC-EPD [57]. However, the obvious problem of a low deposition rate remains with PDC-EPD.

In an AC electric field, the sign of voltage periodically reverses between positive and negative values. AC waveform can be divided by the symmetry and area of both half-cycles: symmetrical AC with no net DC component (Figure 2 C), asymmetrical AC with net DC component (Figure 2 D), and asymmetrical AC with no net DC component (Figure 2 E). In symmetrical AC (Figure 2 C), the particles move a certain distance, x, during the first half-cycle. Then they return to their original position, - x. That is, the net migration of particles theoretically becomes zero because the particles oscillate at a fixed position between two electrodes. Therefore, the efficiency of EPD with symmetrical AC modes is low. Hence, this study investigates EPD with asymmetrical

AC signals. The difference in cycle length and voltage strength between the positive and the negative half-cycles can be motivation energy [58, 59]. Besides allowing uniform deposits by suppressing the formation of gas bubbles due to the electrolysis of water, as shown in Figure 3 [59], EPD under asymmetrical AC signals has other important characteristics. EPD with asymmetrical AC with net DC component allows high probability of orientation. Yue *et al*. [60] controlled the orientation of particles by employing a strong AC signal and improved microstructures of Ag-sheathed $Bi_2Sr_2CaCu_2O_\delta$ tapes. Raissi *et al*. [61] demonstrated dynamic separation of the particles based on shapes in a desired direction for sensor applications.

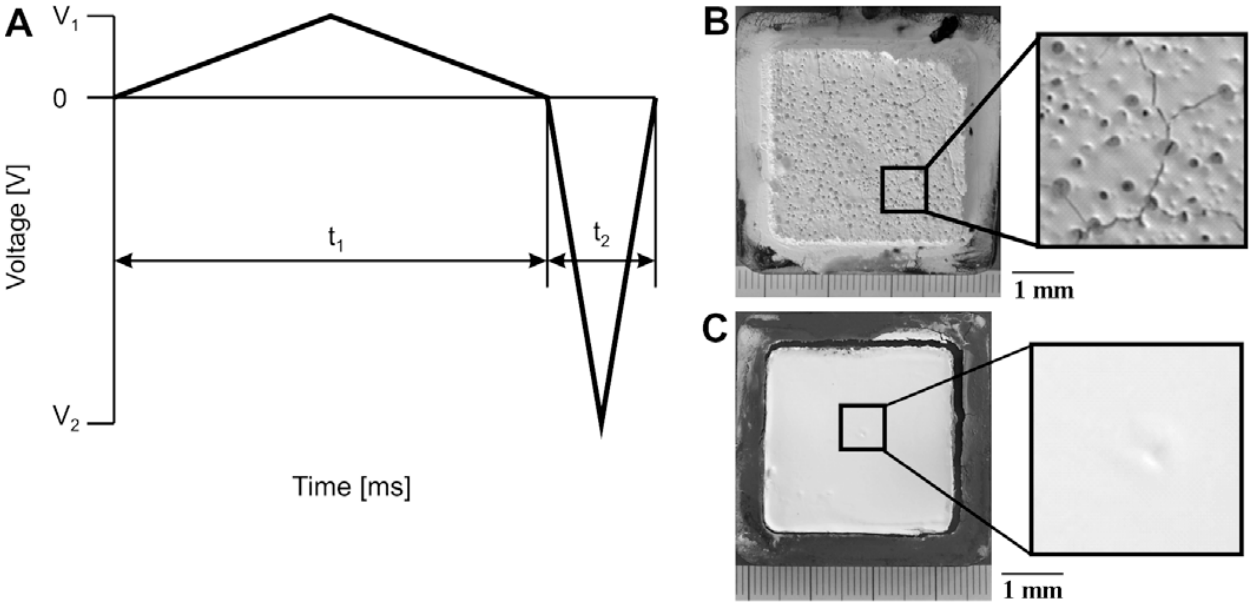

Figure 3. (A) One period of the applied asymmetric AC signal, (B) α-Al_2O_3 deposits formed using 100 V DC for 1200 s, and (C) α-Al_2O_3 deposits formed using 50 Hz 500 Vp-p asymmetric AC field with asymmetry factor 4 [59].

In an AC field, there are two competition mechanisms, the electrochemical reactions and the current that flows through the double layer capacitance. When sufficient frequency is applied to

the suspensions, the current flowing through the double layer is dominant and the electrochemical reactions is suspended [59]. It has been reported [62] that the reaction rate of the electrochemical reactions decreases because hydrogen ions and hydroxyl ions not only involve the reduction of hydrogen ions to hydrogen molecules and the oxidation of hydroxyl ions to oxygen molecules but also participate in the electron transfer and the molecular rearrangement. Thus, an AC field reduces the gas bubbles formed by the decomposition of water.

While in DC fields the electric charge flows only in one direction, in AC fields the movement of the electric charge periodically reverses direction between the positive and negative. Thus, predicting particle behaviors in suspensions under an AC field is much more complicated than in DC. Even though few kinetic studies have been done of AC-EPD, Oddy and Santiago [63] compared the displacement of particles under a DC electric field and an AC electric field. The displacement of a particle, x_{DC}, for a finite time Δt under a DC electric field can be expressed as follows:

$$x_{DC} = \mu_{eph} E_{DC} \Delta t + x_0 \quad \text{(Equation 4)}$$

where μ_{eph} is the electrophoretic mobility, E_{DC} is a DC electric field, and x_0 determines the initial location of the particle. Meanwhile, in case of an AC electric field, the amplitude of the peak-to-peak displacement, x_{AC}, is determined as follows:

$$x_{AC} = -[(\mu_{eph}/E_{AC})/sin(\omega t)\,]/\omega + x_1 \quad \text{(Equation 5)}$$

where E_{AC} is the peak to peak amplitude, ω is the applied angular frequency, and x_1 is the center of the trajectory.

Currently, the focus of research has switched from DC-EPD to AC-EPD. Several studies have reported smooth and thick deposition by using AC electric fields, as summarized in Table 2. Moreover, the use of AC electric fields is attractive due to the possibility of separating the

particle size and controlling the alignment and orientation of nanostructured materials, as well as coating on nonconductive substrates. Therefore, AC-EPD has the potential to be used in a variety of applications.

Table 2. Summary of investigations on the applications of AC-EPD in inorganic material deposition.

Application	Material	Medium	Substrate	Ref
Aqueous suspension	Al_2O_3	Water	Stainless steel	[59]
	TiO_2	Water	Stainless steel	[23]
	PAA-TiO_2	Water	Stainless steel	[64]
	$BaTiO_3$	Water	Aluminium foil	[65]
	SiC	Water	Stainless steel	[66]
	SnO_2	Water	Carbon film base electrode	[67]
Particle separation (size-selectivity)	SnO_2	Acetone	Glass with gold electrode	[61]
Particle separation (shape-selectivity)	ZnO (cubiv and rod)	Acetone	Glass with gold electrode	[68]
Particle separation (conductivity-selectivity)	MWCNT	Water + Alcohol	Electrode coated glass	[69]
Particle separation (controlling density)	Hydroxyapatite	Butanol	Titanium	[70]
Nonconductive substrate	WO_3	Acetone	Alumina	[31]
	TiO_2	Acetone	Alumina	[32]

2.1.4 Application of EPD

Generally, EPD can be applied to coating any type of solids, including metals, ceramics, and polymers, that are dispersed in a medium. Even though there is no general restriction on the

particle size, some researchers regard the range of 1–20 μm as suitable for deposition [5]. However, with increasing research on nanostructured materials, EPD has been extended to assemble nanosized particles.

EPD is attractive for fabricating solid oxide fuel cells, solar cells, batteries, and gas sensors. EPD has great potential for the design of thin, dense, and gas tight electrolytes as well as porous electrodes. Thus, various researchers have investigated EPD techniques for coating protective layers and depositing electrode materials.

The EPD process allows multilayered coating for applications such as laminated materials and functionally graded materials. Layered materials can be obtained by preparing different suspensions and immersing the working electrode in different suspensions.

2.2 Solution based synthesis methods of nanostructured metal oxide

2.2.1 Zinc oxide (ZnO)

Zinc oxide (ZnO) has been widely used in various fields because of its outstanding properties such as a large direct band gap (3.37 eV) and the electrical properties of n-type semiconductors, as well as excellent chemical and thermal stability [1, 39, 71]. Thus, ZnO is attractive for applications in gas sensors, solar cells, photonic crystals, surface acoustic wave filters, light-emitting diodes, and optical devices [1, 39, 71, 72].

A considerable number of researchers have investigated ways to synthesize ZnO nanostructures, including thermal evaporation, chemical vapor deposition, electrochemical, and physical deposition techniques. Among many nanosized ZnO preparation routes, a solution based synthesis method was chosen for this research because of much lower growing temperatures (<200 °C) than other techniques and its usefulness for large scale production [39].

The crystal structure of ZnO is the hexagonal close packing of zinc and oxygen atoms. This structure includes three main crystal planes: a top polar zinc (0001) plane, six symmetric nonpolar zinc – oxygen $10\bar{1}0$ planes, and a basal polar oxygen $(000\bar{1})$ plane. Because of the difference of the structural anisotropy and surface polarity, the growth rates along different planes follow the order: $(0001)>10\bar{1}0>(000\bar{1})$. Thus, ZnO crystals grow preferentially along the [0001] direction and rod-like structures are synthesized normally along the c-axis [73]. The formation of ZnO crystals is explained as follows [1]:

$$Zn^{2+} + OH^- \underset{\Delta}{\rightarrow} ZnO + H_2O \qquad \text{(Equation 6)}$$

To control the morphology of ZnO crystals, the capping effect is important. When citrate anions ($C_3H_5O(COO)_3^{3-}$) exist in the solution, the growth along the $[0001]$ direction is suppressed [74, 75]. Thus, ZnO crystals become nanodisks. Since -COO- and -OH groups in citrate anions preferentially adsorb on the polar zinc (0001) plane, the contact between the growth unit and the polar zinc (0001) plane is interrupted. In this case, growth along the six symmetric directions (preferential equatorial growth) is dominant over the growth along c-axis, allowing the hexagonal disk-like ZnO to be obtained [76]. This effect has also be achieved by introducing citric acid ($C_6H_8O_7$) [77], malate ion ($C_3H_4O_2(OH)COO^-$) [78], sodium bis(2-ethylhexyl) sulfosuccinate (NaAOT) [79], or carboxyl-functionalized polyacrylamide (PAM-COOH) [80].

Table 3. Summary of investigations on the synthesis of disk-like ZnO.

Approach	Precursor	Synthesis method	Ref
Citrate ion	Zinc nitrate + HMT + sodium citrate aqueous solution	Teflon-lined autoclave at 95 °C for 1 day	[74]
	Zinc acetate + ammonia + citrate potassium aqueous solution	Teflon-lined autoclave at 120 °C for 8 hours	[75]
	Zinc acetate + NaOH + sodium citrate aqueous solution	Teflon-lined autoclave at 95 °C for 12 hours	[81]
	Zinc nitrate + HMT + triethyl citrate aqueous solution	Temperature-controlled microwave at 90 °C for 15 min	[39]
	Zinc nitrate + HMT + tripotassium citrate aqueous solution Ammonia + tripotassium citrate aqueous solution	Conversion of amorphous zinc citrate sphere into ZnO disk	[76]
Citric acid	Zinc acetate + NaOH + citric acid aqueous solution	Teflon-lined autoclave at 200 °C for 20 hours	[77]
Malate ion	Zinc acetate + ammonia + sodium malate aqueous solution	Teflon-lined autoclave at 120 °C for 8 hours	[78]
AOT template	Zinc nitrate + ammonia + NaAOT aqueous solution 1-butanol	Microemulsion Reacting at 70 °C for 5 day	[79]
Polymer control	Zinc nitrate + HMT + PAM-COOH aqueous solution	Reacting at 70 °C for 30 min with refluxing then keeping for 5 hours without stirring	[80]

2.2.2 Nickel oxide (NiO)

Nickel oxide (NiO) has been intensively studied as a transition metal oxide because of its useful electronic, magnetic and catalytic properties. NiO is a promising candidate for electrode materials in fuel cells and batteries as well as catalysts, electrochemical capacitors, gas sensors, and magnetic materials [82, 83].

As with the preparation of ZnO nanoparticles, many researchers have studied solution based synthesis methods of NiO nanoparticles. In general, the synthesis of NiO nanoparticles by a solution method includes two steps: 1) the precipitation of nickel precursor and 2) the decomposition to NiO by thermal treatment.

Table 4. Summary of investigations on the synthesis of nanosized NiO by precipitation methods.

Approach	Precursor	Synthesis method	Ref
Organic solvent	Nickel nitrate + oxalic acid in ethanol solution	Precipitated at RT and calcined at 400 °C for 1 hour	[82]
Ammonium precipitation	Nickel sulfate + ammonia aqueous solution	Precipitated at RT and calcined at 300 °C for 1 hour	[83]
	Nickel chloride + ammonium bicarbonate aqueous solution	Precipitated at 40 °C and calcined at 400 °C for 1 hour	[84]
	Nickel chloride + ammonia aqueous solution	Precipitated at RT and calcined at 400 °C for 1 hour	[85]
Urea precipitation	Nickel sulfate + urea aqueous solution	Precipitated at 95 °C and calcined at 400 °C for 2 hours	[86]
Coordination precipitation	Nickel nitrate + ethylendiamine + sodium hydroxide aqueous solution	Precipitated at RT and calcined at 400 °C for 1 hour	[87]
NaOH precipitation	Nickel nitrate + sodium hydroxide aqueous solution	Precipitated at RT and calcined at 500 °C for 6 hours	[88]
Microwave-meditated technique	Nickel nitrate + CTAB + urea aqueous solution	Precipitated with microwave at 120 °C for 15 min and calcined at 300 °C for 3 hours	[45]

2.3 Nanostructured metal oxide for gas sensor applications

Semiconducting nano-scale metal oxides such as tin oxide [10], zinc oxide [1], nickel oxide [11], and copper oxide [12] have been developed as gas sensors that measure the change in electrical conductivity upon exposure to a gas. Tin oxide and zinc oxide are representative n-type semiconducting gas sensing materials; meanwhile, nickel oxide and copper oxide are

representative p-type semiconducting gas sensing materials. A schematic of the formation of electronic core–shell structures in n-type and p-type oxide semiconductors is shown in Figure 4.

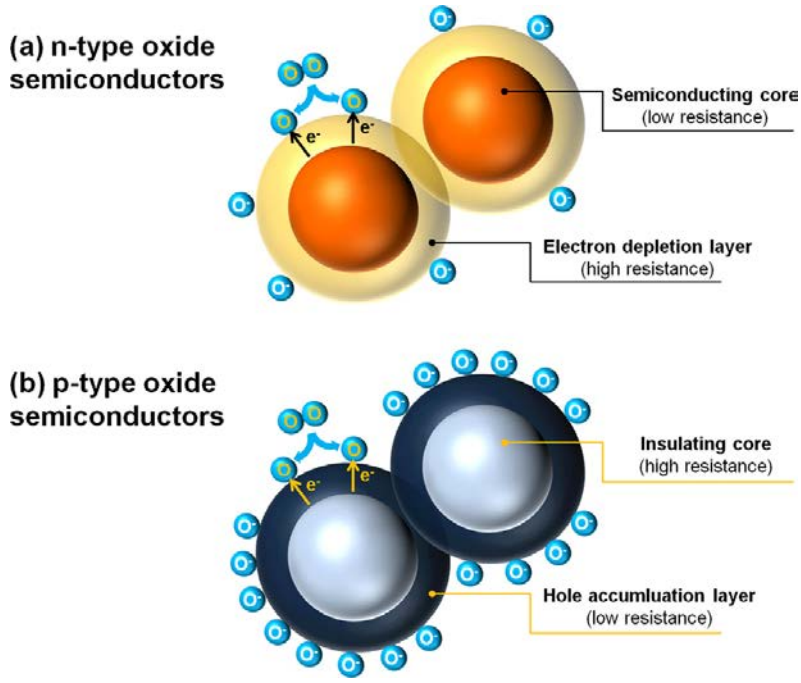

Figure 4. Formation of electronic core–shell structures in (a) n-type and (b) p-type oxide semiconductors [43].

A semiconducting metal oxide gas sensor has a relatively high optimum operating temperature of about 250-350 °C [44, 46, 89]. If the temperature of the sensor is increased about 100-200 °C, oxygen molecules in the atmosphere are adsorbed on its surface. Then, oxygen ion molecules are formed by attracting an electron from the conduction band, as shown in the following equation:

$$O_2(gas) + e^- \Leftrightarrow O_2^-(adsorb). \quad \text{(Equation 7)}$$

However, at higher temperatures, about 250-350 °C, the oxygen ion molecules dissociate into oxygen ion atoms with singly or doubly negative electric charges by attracting an electron again from the conduction band of the sensor, as shown below:

$$\frac{1}{2}O_2 + e^- \Leftrightarrow O^-_{ads}, \quad \text{(Equation 8)}$$

$$\frac{1}{2}O_2 + 2e^- \Leftrightarrow O^{2-}_{ads}. \quad \text{(Equation 9)}$$

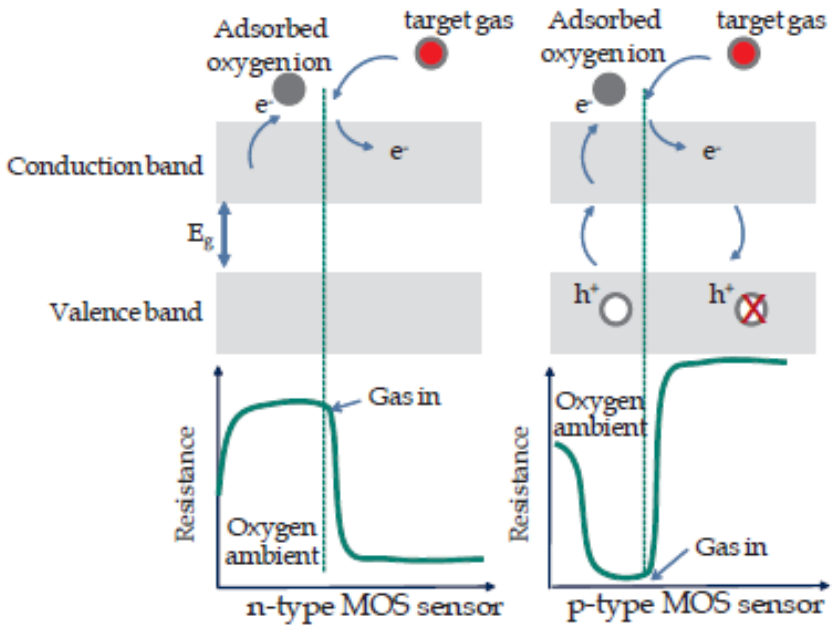

Figure 5. Schematic diagram for change of the sensor resistance upon exposure to the target gas (reducing gas) in the cases of n-type and p-type MOS sensors [89].

Then, the oxygen ions on the surface of the sensor react with the target gas molecules by giving up the electrons from the sensor, as shown in the following equation:

$$X + O^{b-}_{ads} \Leftrightarrow X' + be^-, \quad \text{(Equation 10)}$$

where X and X' are target gas and out gas, respectively, and the b value is the number of electrons.

Because of the chemical reaction between target gas molecules and oxygen ions, the sensor resistance changes as the carrier concentration in the conductivity changes. The change of sensor resistance depends on the type of semiconducting metal oxide gas sensor, as shown in Figure 5. Among various types of metal oxides, zinc oxide, which shows n-type behavior, is an excellent candidate for gas sensors because of its electric properties, such as wide band gap and high electron mobility [1, 39, 71]. Various morphologies for ZnO nanostructures, such as nanorods, nanotubes, and nanowires, have been investigated to understand morphology-driven properties. Recently, some researchers have fabricated hollow micro/nanosphere ZnO and investigated its properties [90, 91]. Such a structure has a large surface-to-volume ratio and reduced transport lengths for both mass and charge transport, making it suitable for applications such as dye-sensitized solar cells, photocatalts, high performance electrodes, and gas sensors [90-94]. J. Rao et al. [94] investigated precision detection of ethanol and acetone with low concentration. The gas response values of ZnO hollow microspheres are 2.2 in 5 ppm ethanol and 2 in 5 ppm acetone, respectively, as shown in Figure 6.

Some researchers have reported enhanced gas selectivity of ZnO hollow microspheres. D. Wang et al. [91] achieved good selectivity to ethanol with hierarchical hollow ZnO microspheres, as shown in Figure 7 (a). In addition, these microspheres showed a fast response time of 1 sec and a fast recovery time of 19 sec. Also, X. Li et al. [93] found that ZnO hollow microspheres showed significant selectivity toward alcohols, such as methanol and ethanol, as shown in Figure 7 (b). Those results indicated that the mesoporous and hollow structure of a ZnO microsphere can enhance its gas sensitivity and selectivity.

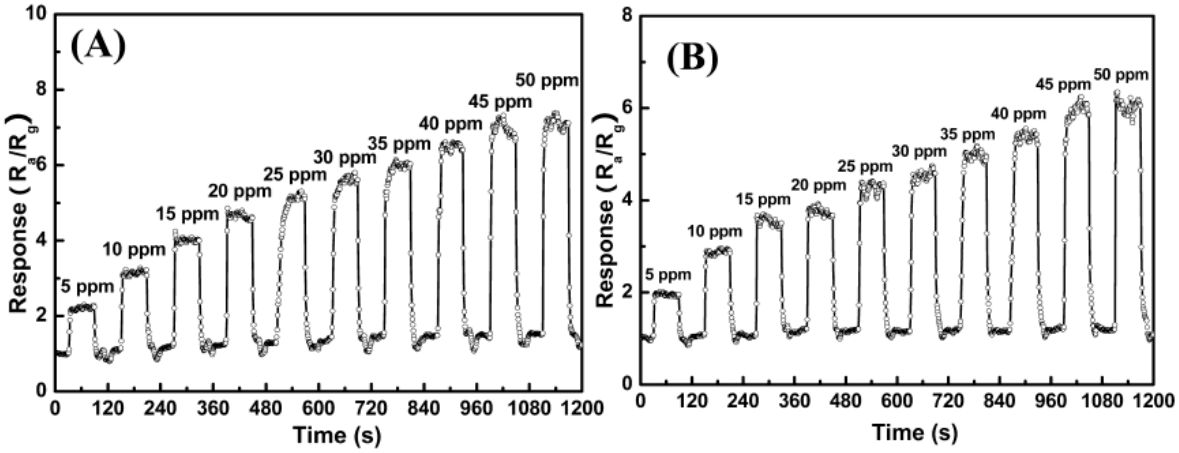

Figure 6. Gas response value curves of the ZnO hollow microspheres sensor to (A) ethanol and (B) acetone [94].

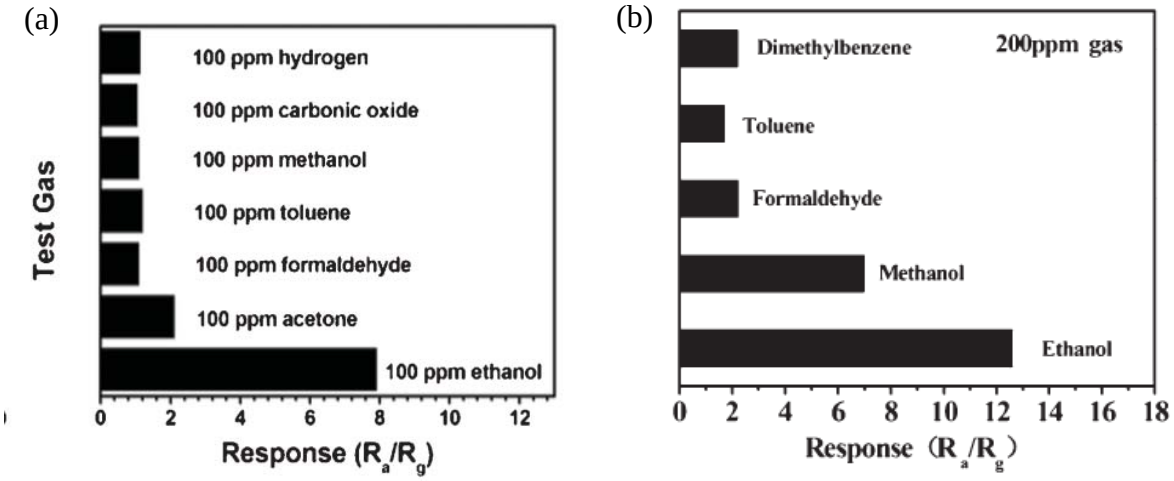

Figure 7. (a) Comparison of the responses to various test gases at 275 °C (b) Response of the sensor to various test gases at 350 °C

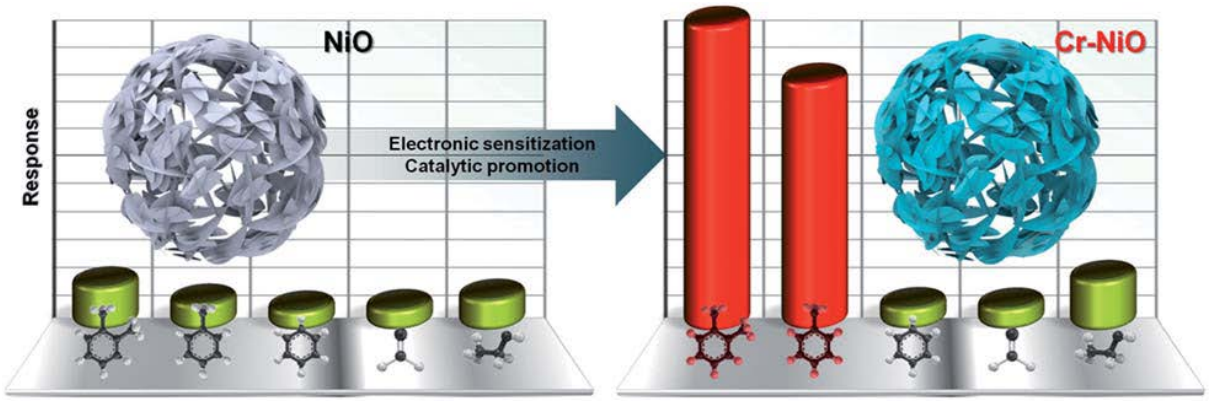

Figure 8. Design of ultraselective and highly sensitive methyl benzene sensors for indoor air monitoring using Cr-doped NiO hierarchical nanostructures [17].

On the other hand, nickel oxide shows a p-type semiconducting behavior. Despite some shortcomings, p-type oxide semiconductors have great potential for use in gas sensors due to their reliable and reproducible switch in electrical conductivity between the air atmosphere and target gas, chemical stability with a highly electroactive nature, and low cost and toxicity [12, 13, 43, 95, 96]. Some researchers have reported enhanced gas selectivity of p-type oxide semiconductors. H. -J. Kim *et al*. [17] achieved high selectivity and response to xylene and toluene with 1.15 at% Cr-doped NiO hierarchical nanostructures, as shown in Figure 8. K. -M. Kim *et al*. [97] investigated the gas selective detection of pure CuO nanosheets and Cr-doped CuO nanorods. They found that 2.2 at% Cr-doped CuO nanorods showed highly sensitive and selective detection of NO_2, as shown in Figure 9. The results indicate that the selectivity and sensitivity of p-type oxide semiconductors can be enhanced with the combination of dopants.

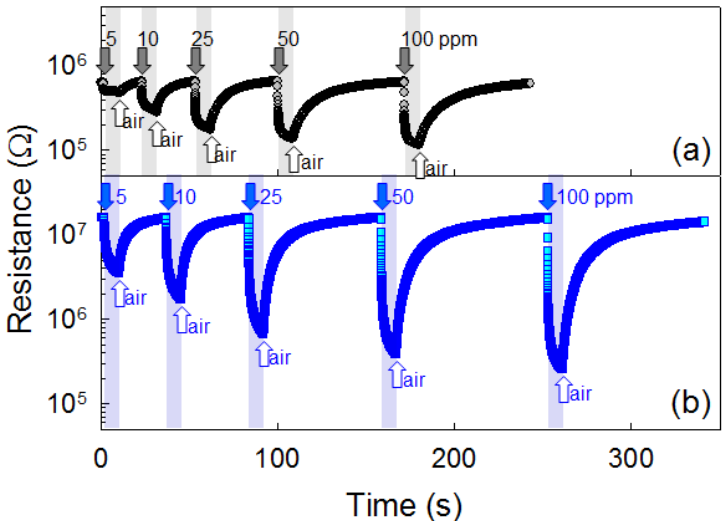

Figure 9. (a) Sensing transients of CuO nanostructures over the range 5–100 ppm NO_2 at 275 °C, (b) Sensing transients of 2.2 Cr-CuO nanostructures over the range 5–100 ppm NO_2 at 275 °C

In addition, heterostructured gas sensors using oxide p-n junctions have been one of the most promising areas of research because various combinations of p- and n-type oxide semiconductors have demonstrated higher performance than those with only one of the two types [43]. C. W. Na *et al*. [98] found that n-type ZnO nanowire with p-type NiO nanoparticles showed significantly enhanced gas response. H. -R. Kim *et al*. [47] suggested that NiO-functionalized SnO_2 hollow spheres achieved rapid recovery. Decorating p-type oxide semiconductors on n-type oxide semiconductors can enhance not only the gas response and selectivity but also the recovery kinetics by transferring charge carriers between p- and n-type oxide semiconductors.

Chapter 3. Experimental method

3.1 EPD process

3.1.1 Materials

Commercially available ZnO powders (Sigma-Aldrich) with different sizes (average size: 50, 100, 200 and 400 nm), anhydrous ethanol (Fisher Scientific) and distilled water were used to prepare suspensions. The prepared ZnO in ethanol suspension is presented in Figure 10.

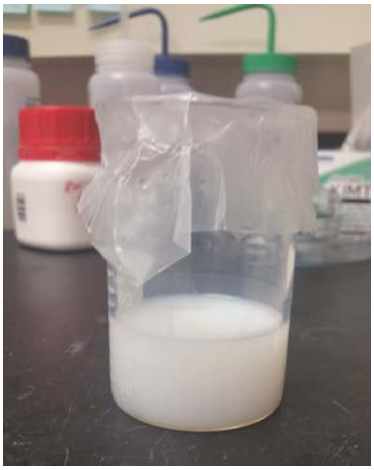

Figure 10. ZnO in ethanol suspension with concentration of 0.02 g/ml.

The particle size distribution of commercially available ZnO powders were described in histograms obtained from the SEM images as shown in Figure 11. Polyethyleneimine (PEI, molecular weight = 25,000, Alfa Aesar) was added as a dispersant. The pH levels of the suspensions were adjusted with ammonium hydroxide (Sigma-Aldrich) and measured by a pH

meter (Fisher Scientific™ accumet™ AB15+) and pH test strips (BDH®). The suspensions were ultrasonicated for 1 hour to improve dispersion, then were immediately used for EPD.

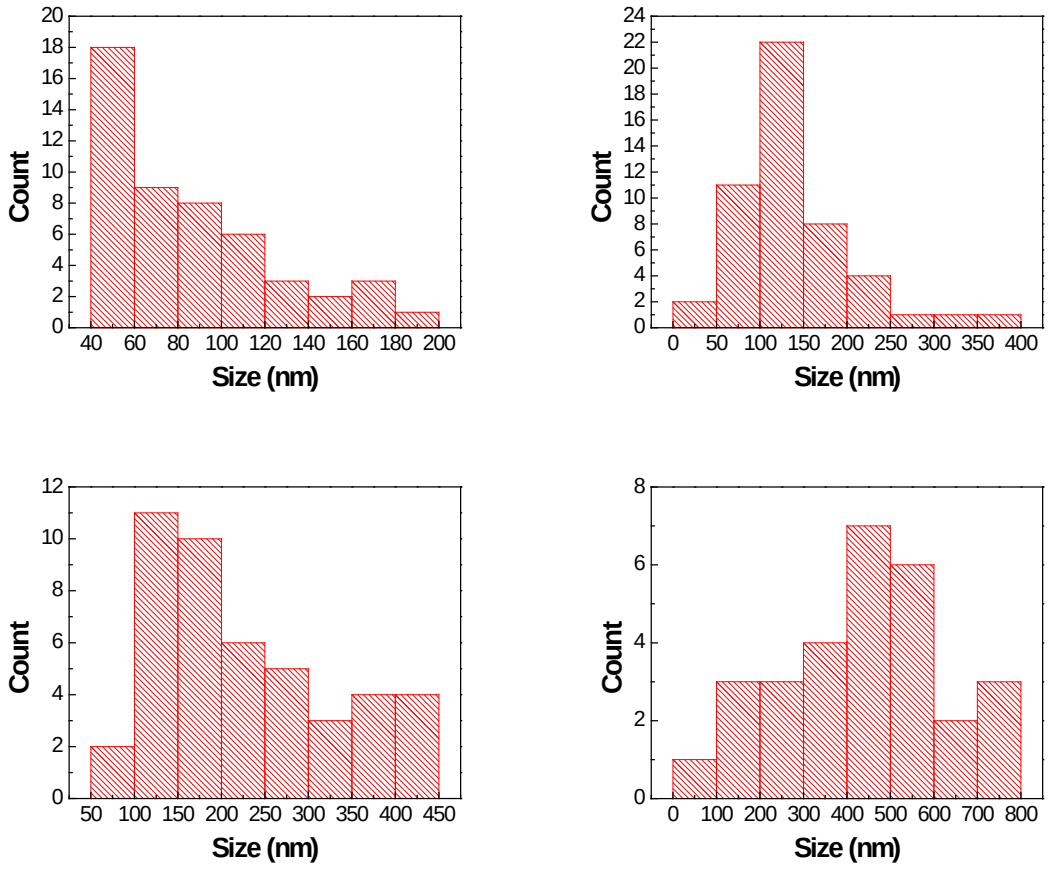

Figure 11. Particle size distribution of commercially available ZnO powders: Histogram obtained from the SEM images.

3.1.2 EPD process

The deposition cell was comprised of a glass beaker containing a stainless steel counter electrode and a working electrode as shown in Figure 12. The working electrodes used for EPD included 301 tempered stainless steel plates (Lyon industry), carbon fabrics (Zoltek), and copper plated fabrics (PCPTF, LessEMF). All substrates were cleaned with ethanol and DI water prior to

deposition. The area of each electrode was 1 cm^2 and the distance between the two parallel-plate electrodes was kept constant at 1 cm.

Figure 12. The deposition cell of the EPD process

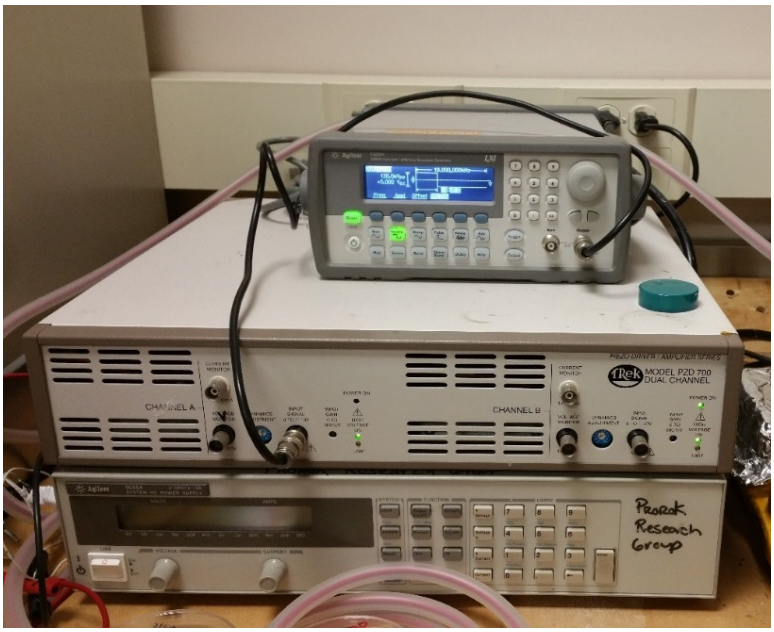

Figure 13. Function generator, AC power amplifier, and DC power supply used for the EPD process

During the EPD process, various DC and AC electric fields were applied across the electrodes. The setup for generating the DC and AC electric fields is shown in Figure 13. For DC EPD, a DC power supply (Agilent 6645A) was used to generate an electric field of 10-100 V/cm. For AC EPD, the square wave form was generated by a function generator (Agilent 33220A) and the strength of the electric field was amplified by an AC power amplifier (Trek PZD 700). After deposition, the coated substrates were air-dried for 24 hours at room temperature and the weight change was measured.

3.2 Synthesis of porous and hollow microsphere zinc oxide

3.2.1 Materials

For the synthesis of porous and hollow microsphere zinc oxide, zinc nitrate hexahydrate ($Zn(NO_3)_2 \cdot 6H_2O$, Fisher Chemical), hexamethylenetetramine (HMT, $C_6H_{12}N_4$, Aldrich), and sodium citrate ($Na_3C_6H_5O_7$, Sigma-Aldrich) were used as starting materials.

3.2.2 Synthesis process

Zinc nitrate hexahydrate ($Zn(NO_3)_2 \cdot 6H_2O$, Fisher Chemical), hexamethylenetetramine (HMT, $C_6H_{12}N_4$, Aldrich), and sodium citrate ($Na_3C_6H_5O_7$, Sigma-Aldrich) were stirred in DI water. The mixed solution was kept in a hot water bath (Iso Temp 202, Fisher Scientific), as shown in Figure 14 (a), at 70 ℃ for 3 hours and dried at 85 ℃ overnight. The resulting precipitates were collected and washed several times with DI water. After drying, the precipitates were calcined in a tube furnace (Lindberg/Blue M), as shown in Figure 14 (b), at 300 ℃ for 1 hour.

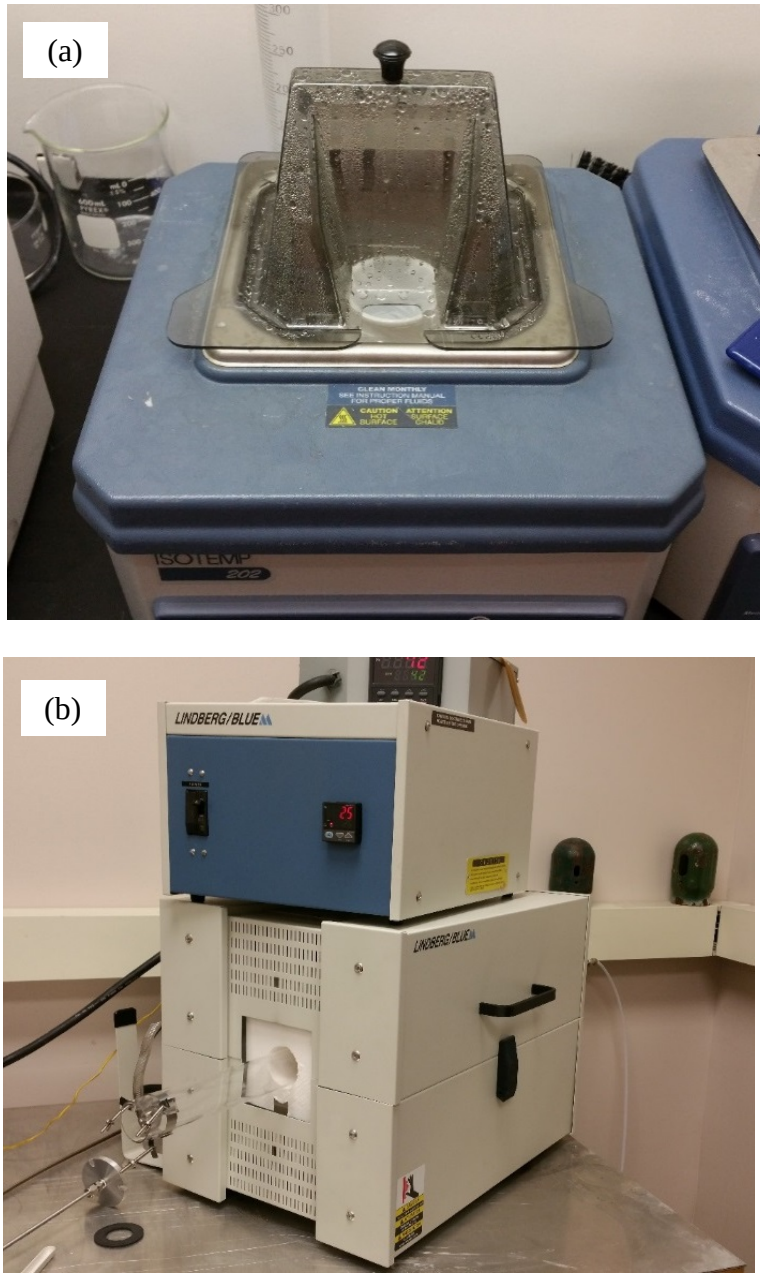

Figure 14. (a) Hot water bath and (b) tube furnace used for the power synthesis

3.3 Synthesis of nickel oxide

3.3.1 Materials

Nickel chloride ($NiCl_2$, Alfa-Aesar) and ammonium oxalate ($(NH_4)_2C_2O_4$, Sigma-Aldrich) were separately dissolved and mixed in DI water. Triethanolamine (TEA, Sigma) was added into one solution for altering NiO morphology.

3.3.2 Synthesis process

Two different morphologies of NiO particles were prepared by a hydrothermal method. Nickel chloride ($NiCl_2$, Alfa-Aesar) and ammonium oxalate ($(NH_4)_2C_2O_4$, Sigma-Aldrich) were separately dissolved and mixed in 10 ml distilled water. One ml of triethanolamine (TEA, Sigma) was added into one solution for altering NiO morphology.

Figure 15. Stainless steel autoclave and oven.

Both solutions were transferred to Teflon containers and autoclaved at 120°C for 10 hours as shown in Figure 15. The two resulting batches of precipitate were collected, washed several times with water, and then calcined at 300°C for 1 hour.

3.4 Material characterization

Zeta potentials of the suspensions were measured using a zeta potential analyzer (Malvern Zetasizer 2000). The morphology of the samples was examined by a field emission scanning electron microscope (FESEM, JEOL JSM-7000F) and a transmission electron microscopy (TEM, Tecnai G2 F30 S-Twin). The crystalline phase of the ZnO was analyzed by X-ray diffraction (XRD, Bruker D8 Discover). Dielectric measurement was performed at frequencies ranging from 100 Hz to 1 MHz and at 100 mV_{osc} using an impedance analyzer (Agilent 4294A). Chemical bonding structure was analyzed by FTIR (Fourier transformation infrared) and the bonding change was analyzed by DSC (differential scanning calorimetry). Room temperature micro-Raman spectroscopy was employed using the 441.6 nm line (80 mW) from He-Cd laser (Kimmon Electric). The ultraviolet-visible diffuse reflectance spectroscopy (UV-vis DRS) was measured with the commercial AvaSpec-2048-USB fiberoptic UV-vis spectrometer. The spectra were measured from 245 to 800 nm. Barium sulphate was used as a white reference material. The room temperature photoluminescence (PL) spectrum was measured with 325 nm line (20 mW) from a continuous-wave He-Cd laser (Kimmon Electric). Specific surface areas were determined using the Brunauer–Emmett–Teller (BET) method with a surface area and pore size analyzer (NOVA 2200e Quantachrome Instruments).

3.5 Device preparation

The process of preparing the electrodes is described in Figure 16.

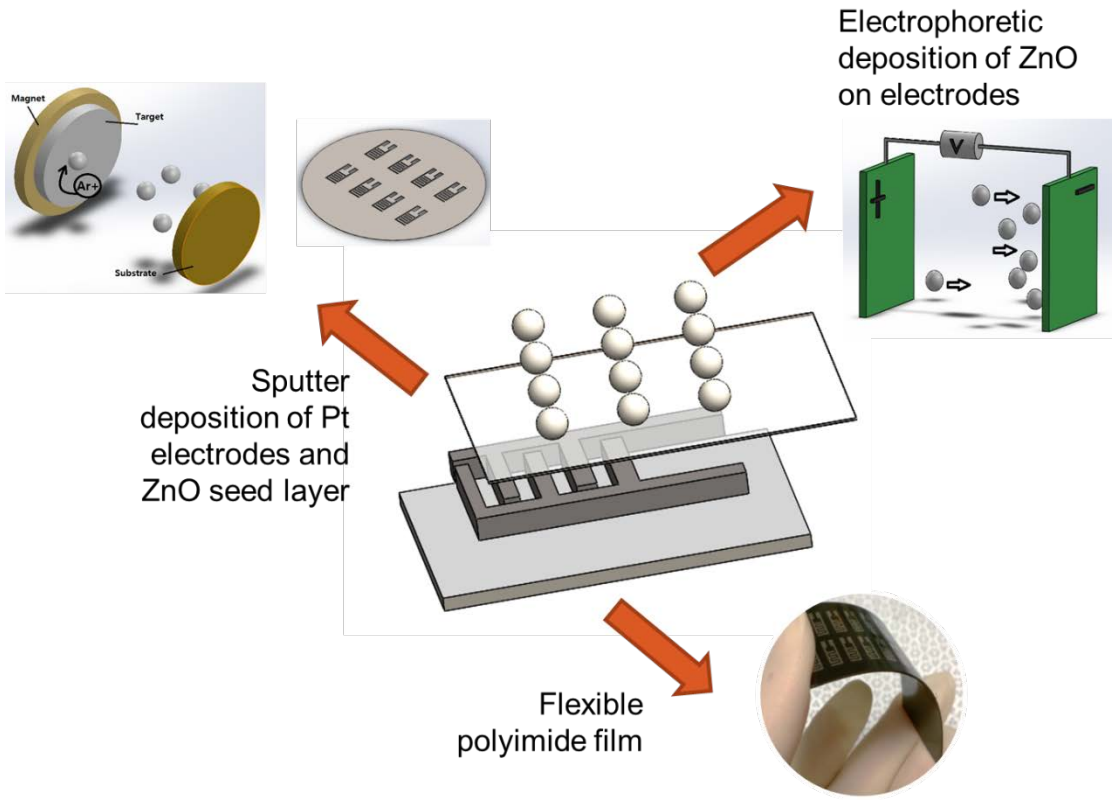

Figure 16. The illustration of the process of preparing electrodes.

To measure gas sensing ability, conductive electrodes must be patterned on the substrates to measure the change of electrical signal. The interdigitated electrodes, which were designed to enlarge the surface area in same dimension resulting in larger conductivity, were patterned on substrates to measure the resistance through sensing layers. The arrays of electrodes were engraved on stainless steel. Each electrode had a width of 500 μm and a distance of 400 μm between electrodes. Each device was 10 x 5 mm. A stainless steel shadow mask of interdigitated electrodes and the patterned Pt electrodes on polyimide film are shown in Figure 17.

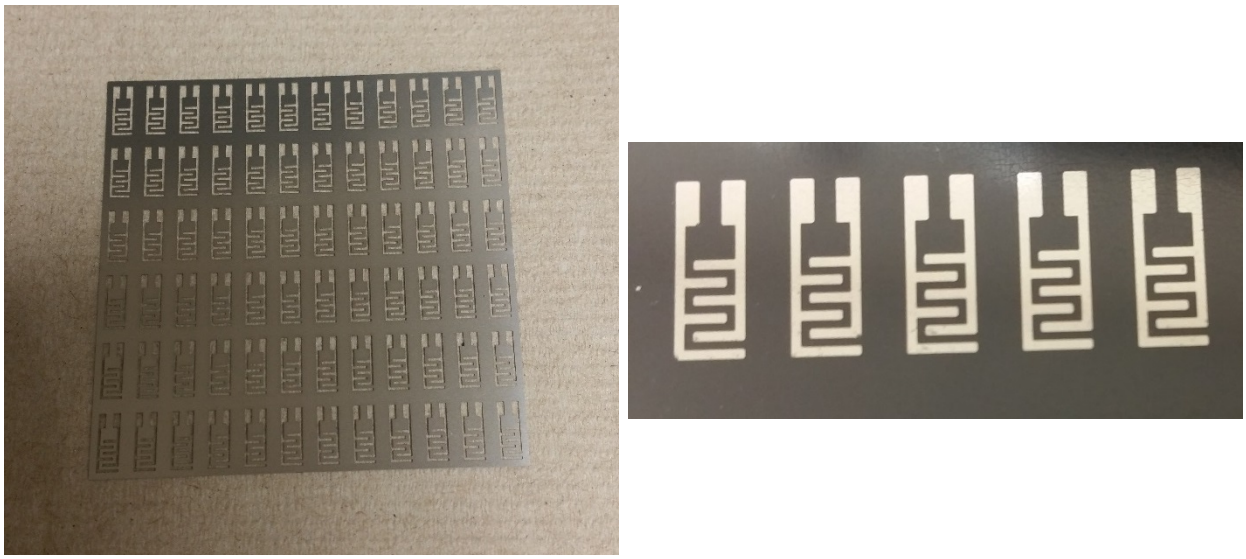

Figure 17. A shadow mask of interdigitated electrodes and patterned electrodes on polyimide film

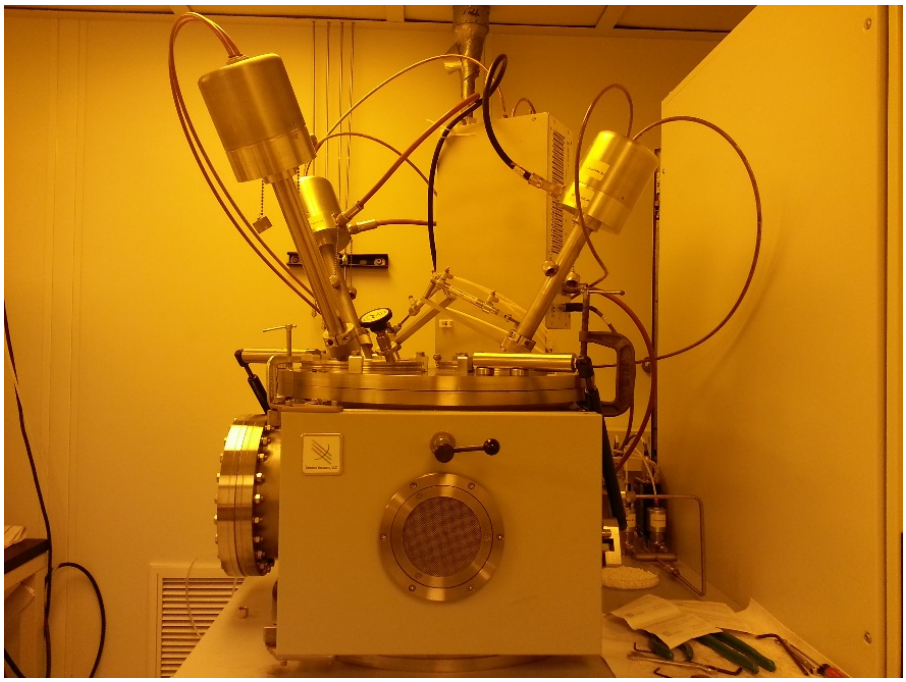

Figure 18. Denton Discovery 18 rf/dc sputtering system

The substrates were placed inside a magnetron-sputter chamber (Discovery 18, Denton Vacuum) as shown in Figure 18. Pt target (Lasker, 99.9 %) was used as the electrode materials because it has good electrical conductivity and resistance to being oxidized [99]. Sputter deposition was performed when the chamber vacuum became below 5 x 10^{-5} mTorr.

3.6 Gas sensing property measurement

Gas sensing behaviors were measured as described in Figure 19.

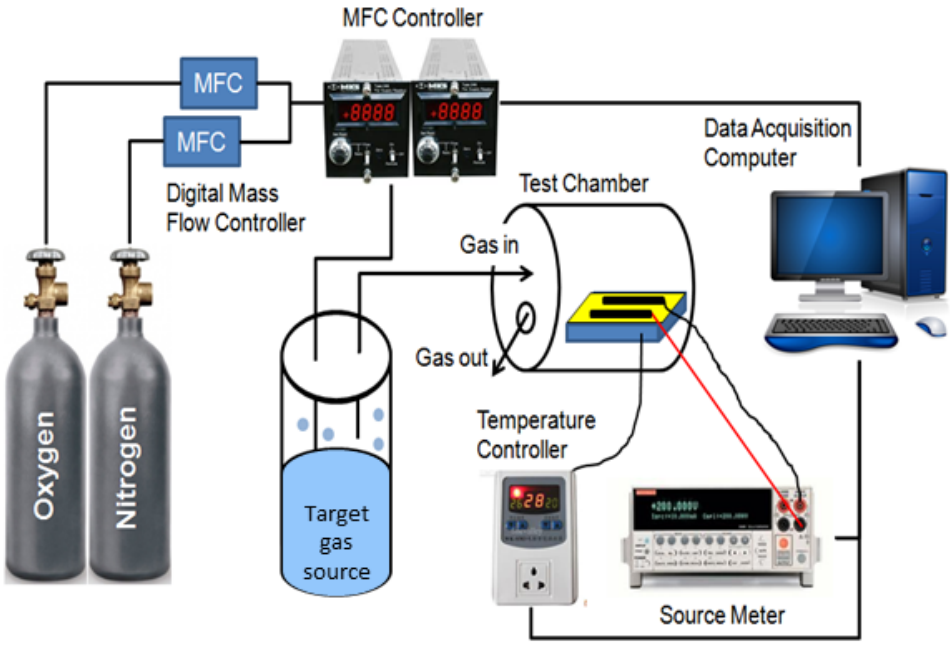

Figure 19. Schematic diagram of configured parts, gas cylinders, temperature controller, MFC (Mass Flow Controller), and data acquisition computer run by NI Lab VIEW.

For a gas delivery, the target gas was injected by nitrogen. Cylinders of oxygen and nitrogen were prepared to produce a synthetic air. The amount and flow rate of the gases were controlled by a MFC (mass flow controller). Once the air mixture flowed into the liquid source, spherical

bubbles were generated and flowed into the gas chamber. The resistance change of the sensor was measured by a digital multimeter (Model 2400-LV SourceMeter, Keithley Instruments Inc.). Two conductive pin points located on the interdigitated electrode were used to detect the resistance signals, and the data was recorded on a personal computer running custom Labview software. For elevating temperature, an aluminum stage with two heaters was designed as shown in Figure 20 and the sensing temperature was controlled by a temperature controller.

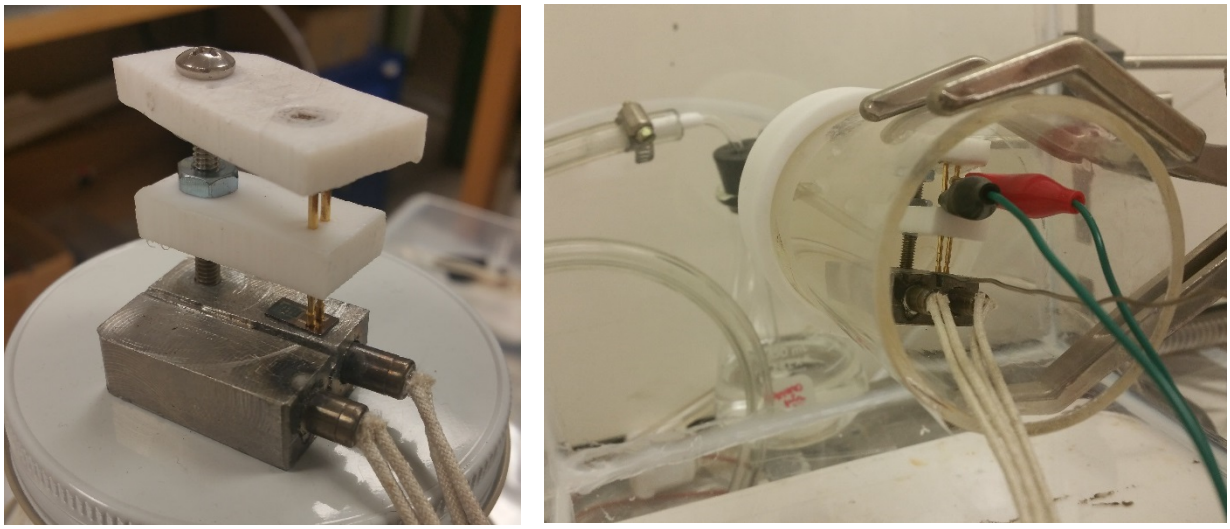

Figure 20. The aluminum stage for elevating temperature and the sensing chamber

Then the gas responses were calculated by the following equation (7):

Gas response = R_a/R_g (Equation 7)

where R_a is the resistance of the air atmosphere and R_g is the resistance of the target gas atmosphere [1].

Chapter 4. Development of EPD for an environmentally friendly process

4.1 Introduction

Based on the governing equations by Hamaker (1) [20] and Zhang (2) [21], zeta potential, time, and electric field are key parameters in the EPD process. These empirical equations are based on suspensions with organic solvents and planar metallic substrates. Thus, prior to studying aqueous systems for EPD, the parameters of the EPD process were studied using commercial zinc oxide powders with different sizes suspended in ethanol deposited on stainless steel plates.

4.2 Experimental method

Commercially available ZnO powders (Sigma-Aldrich) with different sizes (average size: 50, 100, 200 and 400 nm), anhydrous ethanol (Fisher Scientific), and distilled water were used to prepare suspensions. Polyethyleneimine (PEI, molecular weight = 25,000, Alfa Aesar) was added as a dispersant. The pH levels of the suspensions were adjusted with ammonium hydroxide (Sigma-Aldrich) and measured by a pH meter (Fisher Scientific™ accumet™ AB15+) and pH test strips (BDH®). The suspensions were ultrasonicated for 1 hour to improve dispersion, then were immediately used for EPD.

The deposition cell was comprised of a glass beaker containing a stainless steel counter electrode and a working electrode. For both working and counter electrodes, 301 tempered stainless steel plates (Lyon industry) were used. All substrates were cleaned with ethanol and DI water prior to

deposition. The area of each electrode was 1 cm^2 and the distance between two parallel-plate electrodes was kept constant at 1 cm.

During the EPD process, various DC and AC electric fields were applied across the electrodes. For DC EPD, a DC power supply (Agilent 6645A) was used to generate electric fields of 10-100 V/cm. For AC EPD, the square wave form was generated by a function generator (Agilent 33220A) and the strength of the electric field was amplified by an AC power amplifier (Trek PZD 700). After deposition, the coated substrates were air-dried for 24 hours at room temperature and the weight change was measured.

4.3 Results and discussion

4.3.1 EPD with zeta potential

Figure 21 shows the deposition weight of ZnO nanoparticles with different particle sizes at pH ranges of 8-11 under a constant voltage of 50 V for 5 min. The deposition weights from all suspensions sharply decreased at pH levels over 10 and the deposition weights increased as the particle size decreased.

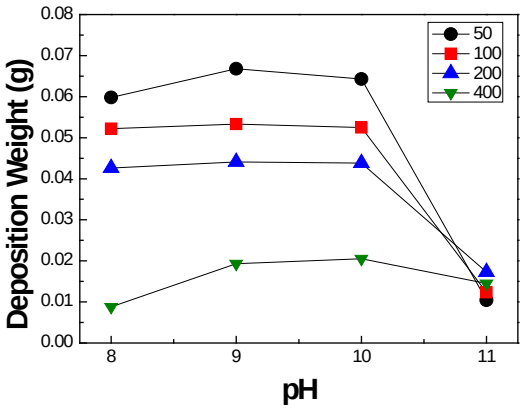

Figure 21. Deposit weight of ZnO nanoparticles with different sizes

This relationship can be explained by zeta potential. Figure 22 (a)-(b) shows the zeta potential with different pH and particle sizes. The operating pH was fixed to pH 9, which shows the highest zeta potential in Figure 22 (a), for all suspensions. The zeta potential values of the suspensions are presented in Figure 22 (b). The values of zeta potential decreased from 25.6 mV to 12. 6 mV as particle size increased from 50 nm to 400 nm. The increase of zeta potential in small particle size could result from a larger specific surface area that tends to adsorb more protonated PEI molecules. Previous research has indicated that PEI charges ZnO surface positively by adsorbing protons at the imido functional group (-NH) in aqueous suspensions. The protonated PEI is maintained at basic pH conditions and modifying the ZnO surfaces increases the isoelectric point (IEP) [26, 27]. In previous work [100, 101], the following reaction on the positive charge of PEI was considered in ethanol solutions, with results similar to a water solution:

$$(-CH_2 - CH_2 - NH -)_n + C_2H_6OH^+ \rightarrow (-CH_2 - CH_2 - NH_2^+ -)_n + C_2H_5OH \quad \text{(Equation 8)}$$

The kinetic equation proposed by Hamaker (1) [20] and Zhang (2) [21] can also explain the effect of particle size on the deposition behavior. Once stable suspensions are obtained, the electrophoretic mobility (μ) is directly proportional to the zeta potential (ζ), as shown in the following equation:

$$\mu = \frac{\xi\varepsilon}{4\pi\eta} \quad \text{(Equation 9)}$$

where ε is permittivity and η is the viscosity of the suspension. Therefore, slower deposition in larger particles can be attributed to reduced electrophoretic mobility driven by zeta potential.

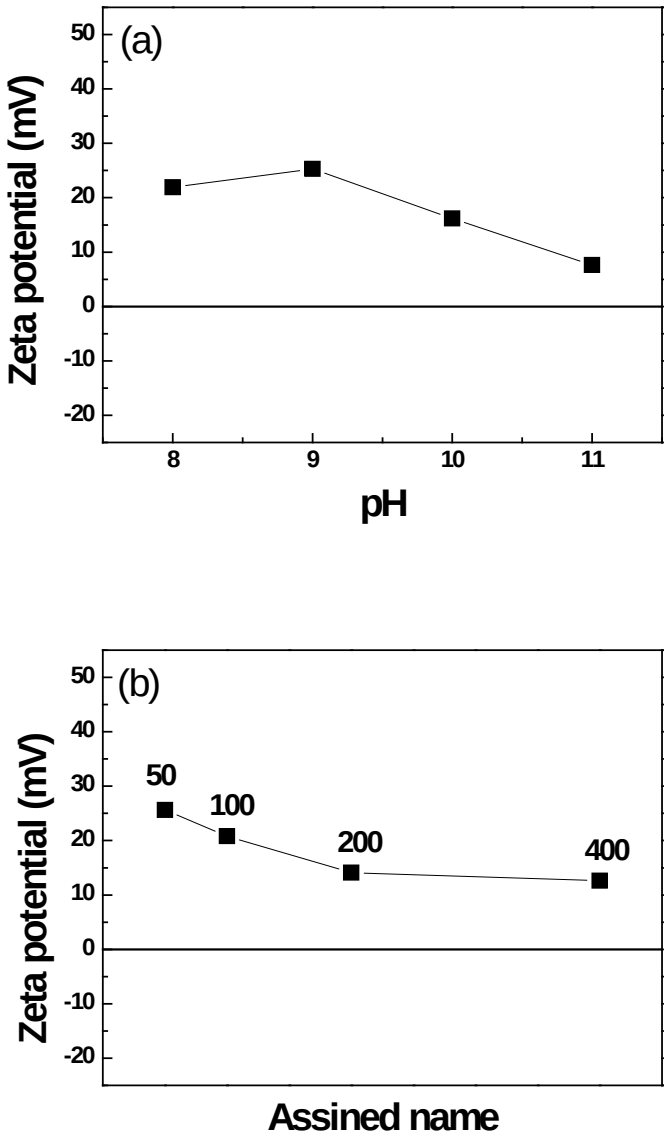

Figure 22. Zeta potential of ZnO nanoparticles dispersed in ethanol with PEI (a) at different pH and (b) with different sizes

4.3.2 EPD with varying voltage

The effect of applied voltage during the EPD process was verified as shown in Figure 23 (a)-(d). EPD was performed with 40, 80, 200, and 400 nm ZnO powders at pH 9 for 1 min with the

applied voltage of 10-100 V. Figure 23 (a)-(d) shows the effect of the applied voltage on the deposition weight. The experimental results were compared with Zhang's equation (2) [21]. As expected, the deposition weight increased as the voltage increased, and the results were mostly consistent with Zhang's equation (2). However, in the case of 40 nm ZnO, the deposition yield was smaller than the expected value. It is possible that smaller particles agglomerate so that they behave as if they are larger particles. To confirm this possibility, analysis of particle size in the suspension is required.

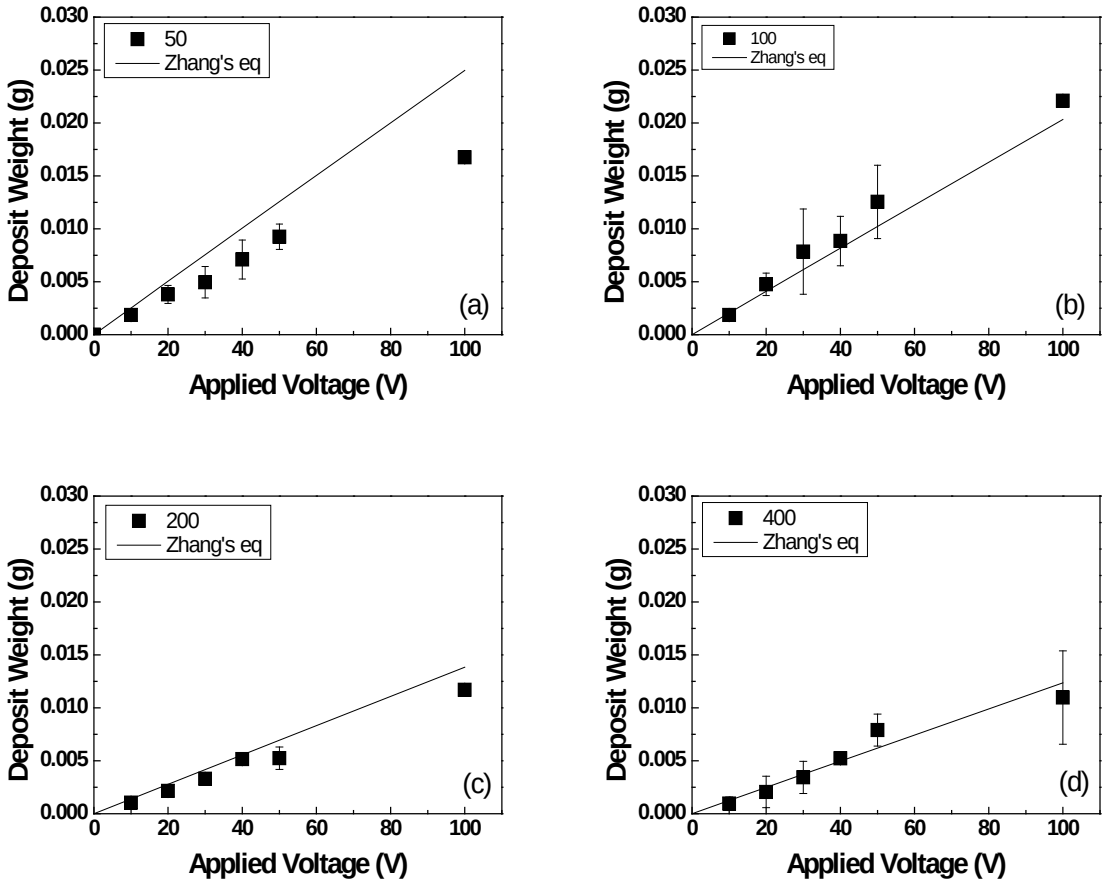

Figure 23. Deposit weight with increasing applied voltage at pH 9 for 1 min: (a) 50 nm, (b) 100 nm, (c) 200 nm, and (d) 400 nm.

4.3.3 EPD with ZnO suspension in mixture of ethanol and water

In previous studies [19, 102], water was regarded as a catalyst. Added water could create H^+ and OH^- ions by electrolysis and then H^+ ions would be a charging agent by adsorbing on the surface of the metal oxide particles. Because of the interaction between H^+ ions and negative ions in the diffuse layer, the electrical double layer could be reduced. Then the particles could move more rapidly due to the increase of Van der Waals forces. However, too high a concentration of ions in the suspension decreases the particle mobility. Thus, the EPD result might have a maximum as a function of added water amount.

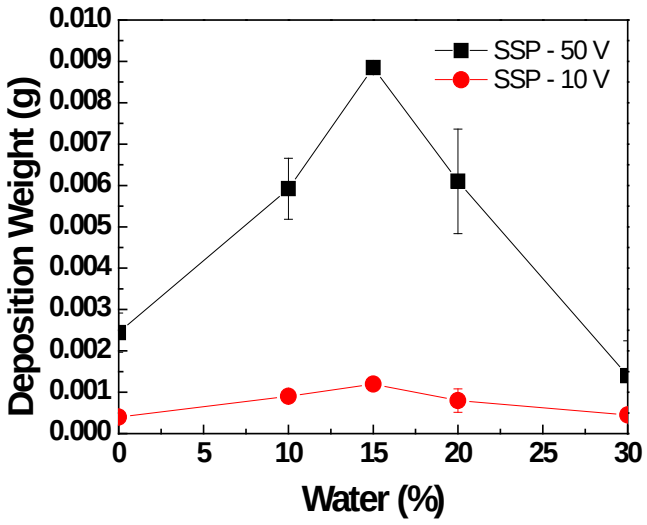

Figure 24. Deposit weight of ZnO nanoparticles dispersed in mixture of ethanol and water (0, 10, 15, 20 and 30 % of water) by EPD on stainless steel plate.

For the feasibility study, 100 nm of ZnO particles were dispersed in mixtures of ethanol and water (0, 10, 15, 20 and 30 % of water) in Figure 24. The EPD process was carried out on stainless steel plates (SSP) at 10 and 50 V for 1 min. Up to 15 vol % of water, deposition weight

increased as the amount of water increased, but at higher percentages, deposition weight decreased. When more than 20 vol % of water was added, the suspensions were not stable and particles agglomerated. Thus, the deposition layer was not smooth and chunks of powder were deposited on the substrate. Also, these cases showed large data deviations. It is possible that too many H^+ and OH^- ions by the electrolysis of water hinders the deposition of particles in suspensions.

4.3.4 EPD with ZnO suspension in water

To achieve an eco-friendly aqueous EPD system, the aqueous EPD process imposes AC electric fields which can reduce the gas bubbles formed by the decomposition of water. An important parameter to consider in AC-EPD is frequency. In previous studies [66, 103, 104], the deposition rate varied with frequency and several aqueous suspensions were found to have a maximum deposition yield due to the reduced wave cycles at low frequency and the insufficient deposition time at high frequency. However, the effect of frequency on the deposition rate has not yet been systemically investigated. In this work, the effect of frequency on the kinetics of AC-EPD is studied by comparing ZnO in aqueous suspensions and ethanol suspensions.

The variation of deposit yield versus frequency is shown in Figure 25. 100 nm of ZnO particles were dispersed in water and ethanol was deposited by AC-EPD with rectangular wave. The AC-EPD process was carried out on stainless steel plates at 50 V for 1 min with frequency increasing from 0.1 Hz to 10 kHz. In the case of ethanol suspensions, frequency up to 100 Hz had no significant effect, but above 100 Hz, the deposition yield decreased. However, for water suspensions, the maximum deposition rate showed at 100 Hz.

In previous studies [66, 103, 104], AC-EPD with aqueous systems showed a maximum deposition yield because the reduced wave cycles at low frequency caused electrolysis of water and too rapid vibration of particles at high frequency caused insufficient deposition time. However, for ethanol systems, since there was no effect of electrolysis of the medium, frequency did not affect deposition yield.

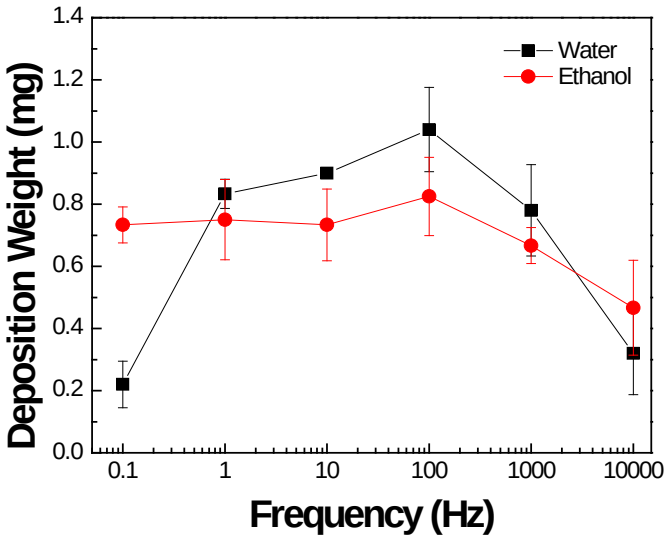

Figure 25. Deposit weight of ZnO nanoparticles dispersed in water and ethanol by AC-EPD on stainless steel plate with frequency (0.1 – 10,000 Hz).

Unlike ethanol suspensions, water suspensions showed a maximum deposition condition at 50V and 100 Hz. The results showed that in AC-EPD using an aqueous solution, which is environmentally safe and economically feasible, deposition kinetics can be controlled through frequency to deposit either thin or thick metal oxide films as needed for many applications.

4.4 Summary and conclusions

Prior to studying EPD with aqueous suspensions, ZnO nanoparticles suspended in ethanol were used to study the parameters of zeta potential and applied voltage. The deposition weights sharply decreased at pH levels over 10 and deposition weights increased as particle size decreased due to an enhanced zeta potential. Although the deposition weight showed a linear relationship with applied voltage, the dried morphology of the ZnO nanoparticle layers showed more uniform packing at smaller size and lower applied voltage.

Based on these findings, ZnO nanoparticles suspended in a mixture of ethanol and water systems were deposited to study the effect of adding water. The EPD result showed a maximum as a function of added water amount. The charging agent effect of H^+ ions formed by water electrolysis competed with reducing particle mobility by too high a concentration of ions in the suspension.

To achieve an environmentally benign aqueous EPD system, this study identified approaches for an aqueous EPD process conducted with AC electric fields which can reduce the gas bubbles formed by the decomposition of water. The effect of frequency, which is a key parameter, on the kinetics of AC-EPD was compared with ZnO in aqueous suspensions and ethanol suspensions. AC-EPD with an aqueous system showed a maximum deposition yield because the reduced wave cycles at low frequency caused electrolysis of water and too rapid vibration of particles at high frequency caused insufficient deposition time. However, for ethanol systems, low frequency had no significant effect on deposition yield.

Chapter 5. Conductive and flexible substrates for EPD

5.1 Introduction

Much efforts to control the structure and function of materials at the nanoscale have made due to their great potential for a wide range of applications, such as energy conversion devices, electronic components, data storage devices, biosensors and biomedical applications [1, 2]. As methods to build nanostructures on the surface of materials, coating from solution precursors such as electrolytic deposition (ELD) and electrophoretic deposition (EPD) has been applied [105]. In particular, the electrophoretic deposition (EPD), one of colloid techniques provides various advantages in the processing of ceramic materials because of its high versatility for coating a wide variety of compounds with different structures as well as low cost equipment [3-5, 106]. Uniform coating of electrophoretically deposited materials has been demonstrated on three-dimensional, porous, and even flexible substrates [5]. In case of flexible fibers or wire substrates for EPD, there are reports on bohemite coating on stainless steel fiber mats [107] and alumina on stainless steel wires [108]. The applicability of EPD by coating metal oxides on solid substrates has been well studied, but few studies have been performed on fabrics. The use of fabrics for embedding or coating nanostructured functional materials could leverage wearable multi-functional devices [7-9].

In this study, ZnO nanoparticles were coated by EPD on flexible fabric and solid plate substrates. The effects of particle size, applied voltage, and substrate type on the EPD kinetics and

morphological properties were investigated. Stable ZnO suspensions were formed by characterizing the zeta potential, indicating controlled electrostatic interactions between the particles dispersed in ethanol. The deposition kinetics of the ZnO particles were evaluated by examining the zeta potential and the electric field for different particle sizes. The structural, optical properties, and dielectric properties of deposit ZnO layers by EPD were also examined by X-ray diffraction (XRD), Micro-Raman spectroscopy, ultraviolet-visible diffuse reflectance spectroscopy (UV-Vis DRS), photoluminescence (PL) spectroscopy, and impedance analyzer.

5.2 Experimental method

Commercially available ZnO powders (Sigma-Aldrich) with different sizes and anhydrous ethanol (Fisher Scientific) were used to prepare suspensions. Polyethyleneimine (PEI, molecular weight = 25,000, Alfa Aesar) was added as a dispersant. The pH levels of the suspensions were adjusted with ammonium hydroxide (Sigma-Aldrich), and the pH for suspensions with different particle sizes was kept at 9. The suspensions were ultrasonicated for 1 hour to improve dispersion and were immediately used for EPD. The Zeta potentials of the suspensions were measured by using a zeta potential analyzer (Malvern Zetasizer 2000). The substrates used for EPD included 301 tempered stainless steel plates (Lyon industry), copper plates (Sigma-Aldrich), carbon fabrics (Zoltek), and copper plated fabrics (PCPTF, LessEMF). All substrates were cleaned with ethanol and DI water prior to deposition. The deposition cell was comprised of a glass beaker containing a stainless steel counter electrode and a working electrode. The area of each electrode was 1 cm^2 and the distance between two parallel-plate electrodes was kept constant at 1 cm. During EPD process, various voltages were applied across the electrodes. After

deposition, the coated substrates were dried in air for 24 hours at room temperature, and the weight change was measured.

The morphology of the deposited ZnO layer was examined by using a field emission scanning electron microscope (FESEM, JEOL JSM-7000F). The crystalline phase of the ZnO was analyzed by using X-ray diffraction (XRD, Bruker D8 Discover) with Cu Kα radiation in the 2θ range from 20 to 80◦ with a step size of 0.02◦. In order to measure the dielectric properties, we sputtered platinum on the surface of the dried ZnO layer. The dielectric measurement was performed at frequencies ranging from 100 Hz to 1 MHz and at 100 mV*osc* by using an impedance analyzer (Agilent 4294A). Room temperature micro-Raman spectroscopy was employed using the 441.6 nm line (80 mW) from He-Cd laser (Kimmon Electric). The UV-vis DRS measurements were performed with the commercial AvaSpec-2048-USB fiberoptic UV-vis spectrometer. The spectra were measured from 245 to 800 nm. Barium sulphate was used as a white reference material. Room temperature PL spectrum was measured with 325 nm line (20 mW) from a continuous-wave He-Cd laser (Kimmon Electric).

5.3 Results and discussion

5.3.1 Electrophoretic deposition behavior of ZnO nanoparticles and their properties on conductive fabrics

Zeta potential of ZnO nanoparticles in ethanol and PEI suspensions prepared at different pH levels were characterized. Since ZnO is easily soluble in acid [26], suspensions were measured at basic pHs. Figure 26 shows that PEI charges ZnO surface positively. ZnO has a relatively high positive zeta potential at pH 9, and then it decreases with increasing pH levels. It is reported that PEI in ZnO aqueous suspension modifies the surface of ZnO particles by increasing the

isoelectric point (IEP) [26, 27]. PEI can adsorb protons in the suspension due to the imido functional group (−NH) so that PEI becomes positively charged [26, 27]. Since the protonated structure of PEI can be maintained at basic pH levels, PEI is regarded as an effective dispersant [27]. The reactions of PEI in ethanol suspensions had not been reported. But the following reaction on the positive charge of PEI in ethanol can be expected from PEI and water system [100, 101]:

$$(-CH_2 - CH_2 - NH -)_n + C_2H_6OH^+ \rightarrow (-CH_2 - CH_2 - NH_2^+ -)_n + C_2H_5OH \quad \text{(Equation 8)}$$

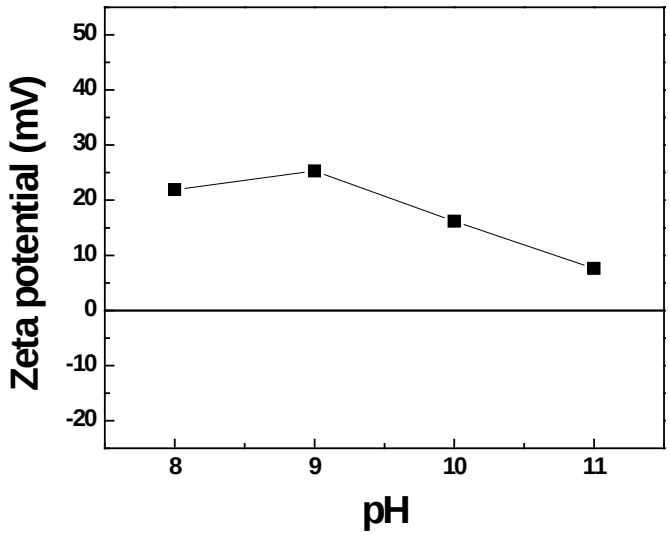

Figure 26. Zeta potential of ZnO nanoparticles dispersed in ethanol with PEI.

It is likely that ZnO surface may lose protons and zeta potential become lower at high pH. This can explain the decrease of zeta potential with pH as shown in Figure 26. Once stable suspensions are obtained, one of the important parameter to influence EPD kinetics can be the electrophoretic mobility since the mobility of particles is directly proportional to zeta potential. Therefore, pH 9 representing the highest positive charge, was kept and other parameters relating

to EPD such as voltage and time were investigated. Suspensions of ZnO nanoparticles with a concentration of 2.5 wt% in ethanol were used in this EPD.

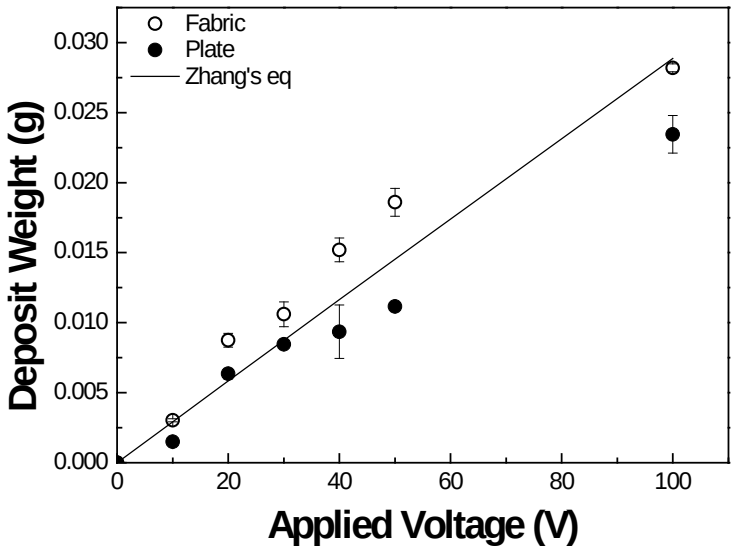

Figure 27. Deposit weight of ZnO nanoparticles by EPD on Cu coated fabric and Cu plate as a function of applied voltage.

ZnO nanoparticles were deposited on flexible fabrics and solid plates for comparative study. The weight gain of the deposit on both substrates was measured as a function of applied voltage as shown in Figure 27. The weight gain of ZnO deposits on both Cu coated fabric and Cu plate increased linearly with the applied voltage. The kinetic equation proposed by Zhang *et al*. [21] was used to observe the deposition behavior. The equation shows that the weight of the deposit (W) can be expressed as an exponential function of time of the reaction:

$$W(t) = W_0\left(1 - e^{-kt}\right) \text{ with } k = \frac{fA\varepsilon_0\varepsilon_r\xi E}{4\pi V\eta} \qquad \text{(Equation 11)}$$

where the kinetic constant is k, the deposition time is t, the deposition area is A, the volume of suspension is V, the starting weight of the particle in the suspension is W_0, the dielectric constant of the liquid is ε, the zeta potential of the particle in the solvent is ζ, the viscosity of the suspension is η, the applied voltage is E, and the voltage drop across the deposited layer is ΔE. The experimental and the calculated data indicate good agreement. But larger deposition weight of ZnO nanoparticles on Cu coated fabric was observed than the predicted values by the Zhang's equation. Larger surface area of woven fabric due to non-flat surface can be attributed to more deposition of ZnO nanoparticles. At higher applied voltage of 100 V, ZnO deposition showed smaller weight than the predicted values by the equation. The reduced potential by shielding effect [5] of pre-deposited particles can lower the deposition rate.

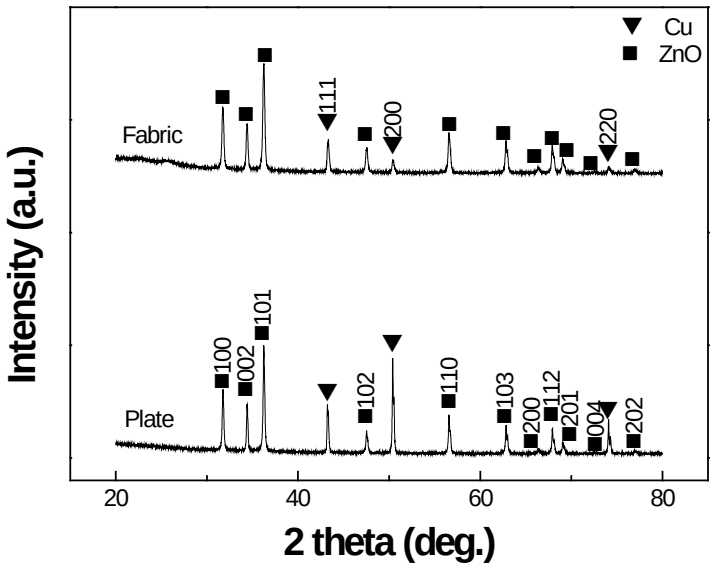

Figure 28. XRD patterns of ZnO nanoparticle layer by EPD on a Cu coated fabric and a plate.

The deposited ZnO particles on Cu plate and fabric were examined by XRD as shown in Figure 28. The deposition was performed at 10 V and 1 min. XRD patterns show only peaks of ZnO and Cu for both samples. No preferred orientation of ZnO layers was observed. Micro-Raman spectroscopy was employed to characterize ZnO nanostructure deposited by EPD on Cu plate. Lorentzian functions were used to fit Raman spectra. Figure 29 shows a very strong band at 435 cm^{-1} corresponding to E_2 vibration and a weak band at 576 cm^{-1} presenting A_1 vibration, which are typical ZnO peaks in Raman spectrum. The E_2 phonon frequency of the as-deposited ZnO layer is comparable to the report [109]. The observed E_2 vibration frequency of the ZnO layer was decreased compared to that of bulk ZnO (438.5 cm^{-1}) due to the phonon confinement or the presence of intrinsic defect on nanostructures [109].

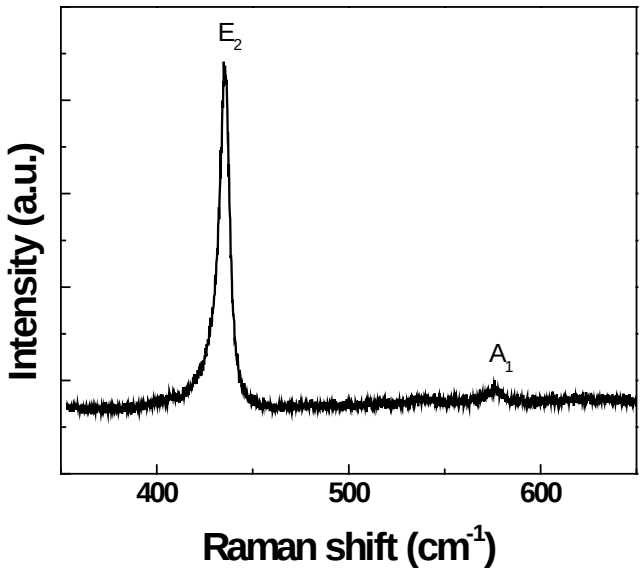

Figure 29. Micro-Raman spectrum of ZnO nanoparticle layers by EPD on a Cu plate.

The morphologies of EPD ZnO on Cu substrates are shown in Figure 30. ZnO coverage on both Cu plate and fabrics appears to be uniform. But ZnO layer deposited at 10 V shows slightly dense and less porous microstructure compared with ZnO deposited at 50 V. Higher electric field in EPD process promotes particles to be coated more quickly, but uniform and dense coating may be limited. In addition, faster EPD deposition showed cracks on the surface for both substrates as a consequence of the drying gradient. Therefore, an adequate control of the suspensions and deposition rate is necessary to obtain crack-free deposits.

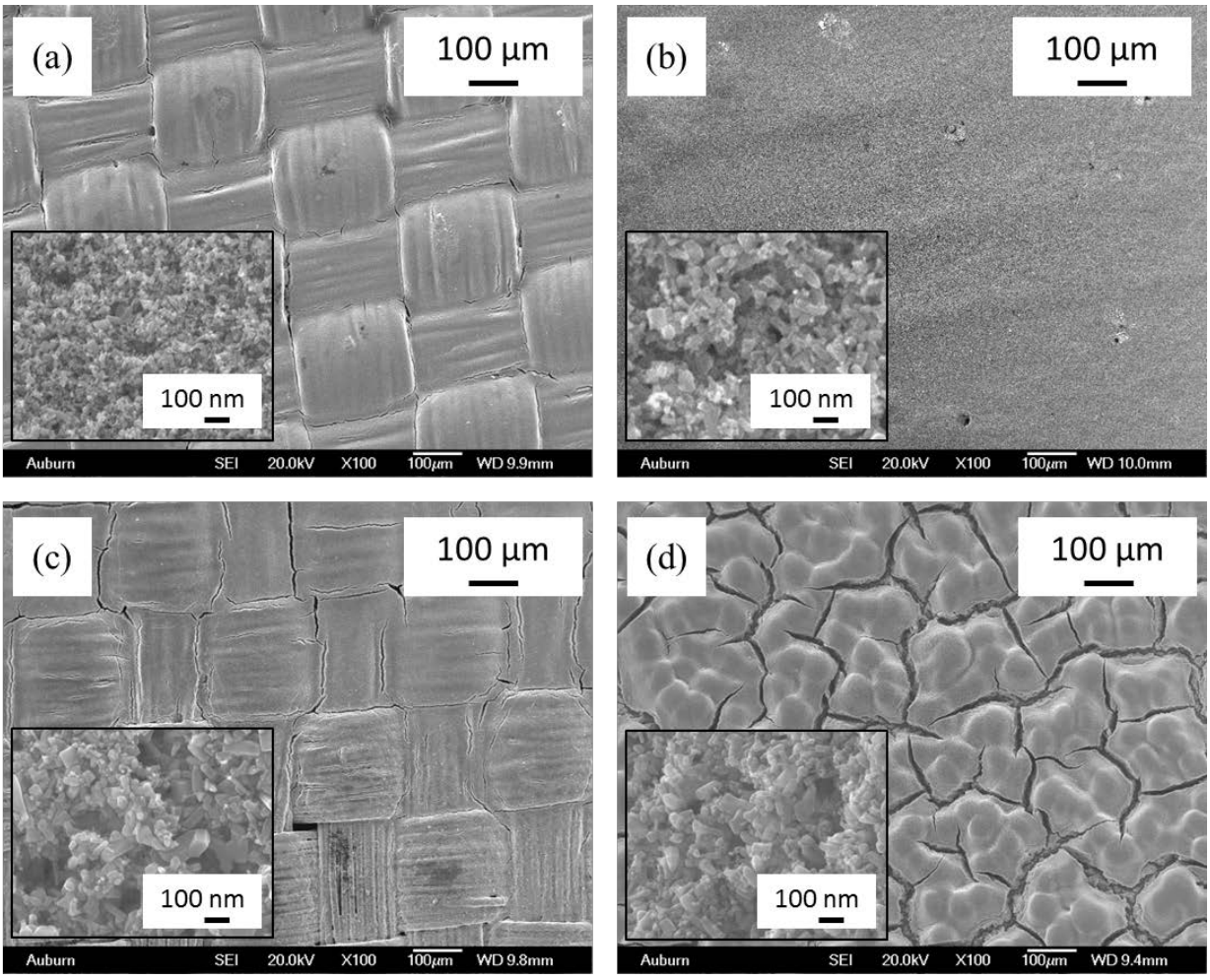

Figure 30. SEM images of ZnO layers by EPD at 10 V on (a) Cu coated fabric and (b) Cu plate and at 50 V on (c) a Cu coated fabric and (d) a Cu plate.

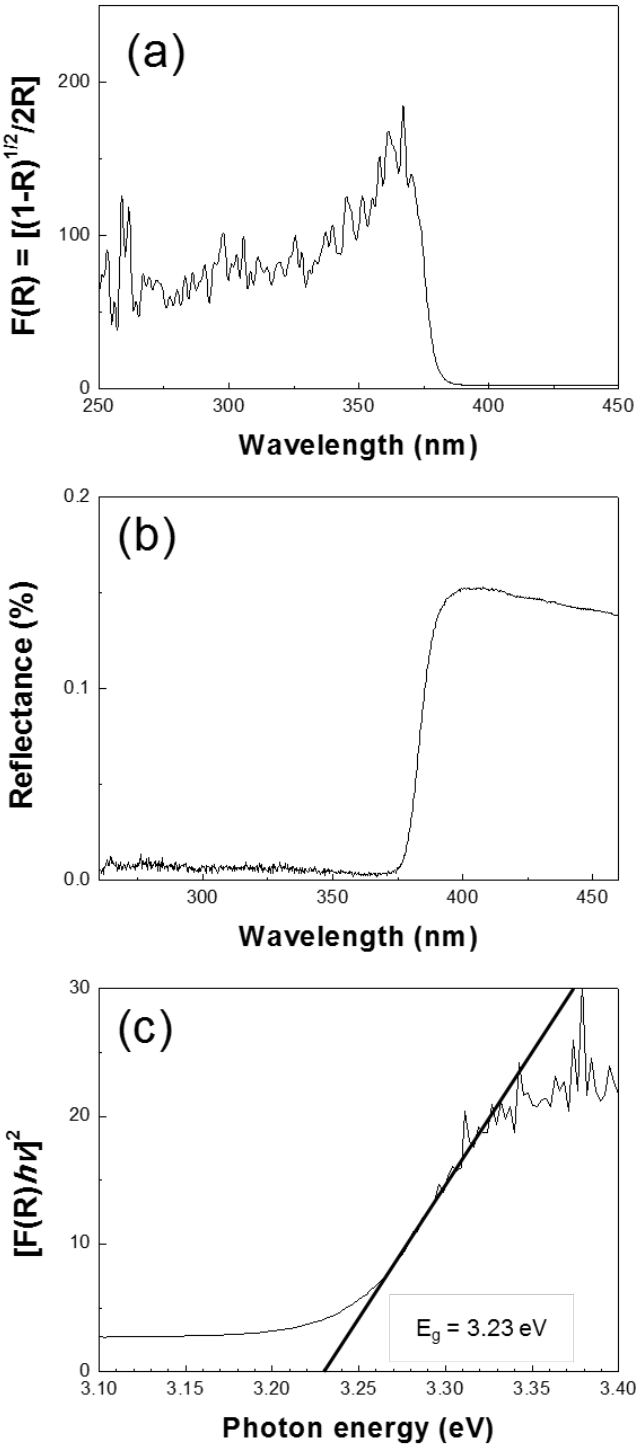

Figure 31. (a) UV-Vis absorption spectrum, (b) diffuse reflectance spectrum, and (c) Kubelka-Munk transformed reflectance spectrum of ZnO layer deposited at 10 V on Cu coated fabric.

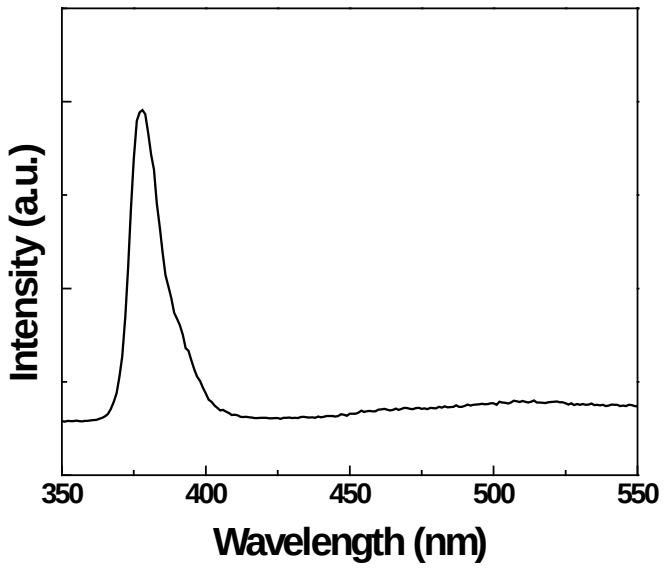

Figure 32. Photoluminescence spectrum of ZnO nanoparticle layers by EPD on a Cu plate.

The optical properties of dried ZnO layer on Cu coated fabrics deposited at 10 V was studied by UV Vis DRS as shown in Figure 31. The absorption spectra of ZnO was expressed as the Kubelka-Munk function [F(R∞)] obtained from diffuse reflectance measurements as shown in Figure 31 (a), and the diffuse reflectance spectrum of the ZnO layer is given in Figure 31 (b). In the UV-Vis absorption spectrum, a sharp decrease in intensity is observed around 390 nm, and the reflectance spectrum shows broad absorption below 400 nm. Such change is caused by band edge absorption as reported [110-112]. In Figure 31 (c), $[F(R) \cdot E]^2$ versus photon energy (E) is plotted, where F(R) is the Kubelka-Munk function with $F(R) = (1-R)^{1/2}/2R$ and R that is the observed diffuse reflectance [111]. The intersection between the linear line and the axis of photon energy represents the value to Eg [111, 113]. The band gap energy is determined to 3.23 eV, which is comparable to nanostructured ZnO [110, 111, 113]. Compared with reported bulk-

shaped ZnO (3.37 eV), the smaller value could be attributed to the presence of surface defects driven by low drying temperature and/or smaller nanoparticle size [110, 111, 113]. Photoluminescence spectrum of the ZnO layer on Cu plate by EPD is shown in Figure 32. A very strong emission peak was detected at 379 nm (3.27 eV) which is very similar to the reported values [71, 109], but the peak was slightly shifted to lower value. The peak shift in the as-deposited ZnO layer could result from higher defect density on the surface of the ZnO layer [71, 109].

5.3.2 Growth and dielectric properties of ZnO nanoparticles deposited by using electrophoretic deposition

Figure 33 shows the deposition weight of ZnO nanoparticles with different particle sizes. When the same deposition conditions of pH, time, and voltage were used, the deposition weight of the ZnO layer corresponding to the deposition rate shows a higher value for a smaller particle size. Such a relationship can be explained by the zeta potential. The values of zeta potential decrease from 25.6 mV to 12.6 mV with increasing particle size from 50 nm to 400 nm as shown in Figure 33. The increase in the zeta potential for small particle size can result from a larger specific surface area which tends to adsorb more protonated PEI molecules. PEI has been reported to charge the ZnO surface positively by adsorbing protons at the imido functional group (-NH) in aqueous suspensions. The protonated PEI is maintained at basic pH conditions and the modification of the ZnO surfaces increases the isoelectric point (IEP) [26, 27]. In a previous work [100, 101], the following reaction on the positive charge of PEI was considered in ethanol similar to that in a water solution:

$$(-CH_2 - CH_2 - NH -)_n + C_2H_6OH^+ \rightarrow (-CH_2 - CH_2 - NH_2^+ -)_n + C_2H_5OH \quad \text{(Equation 8)}$$

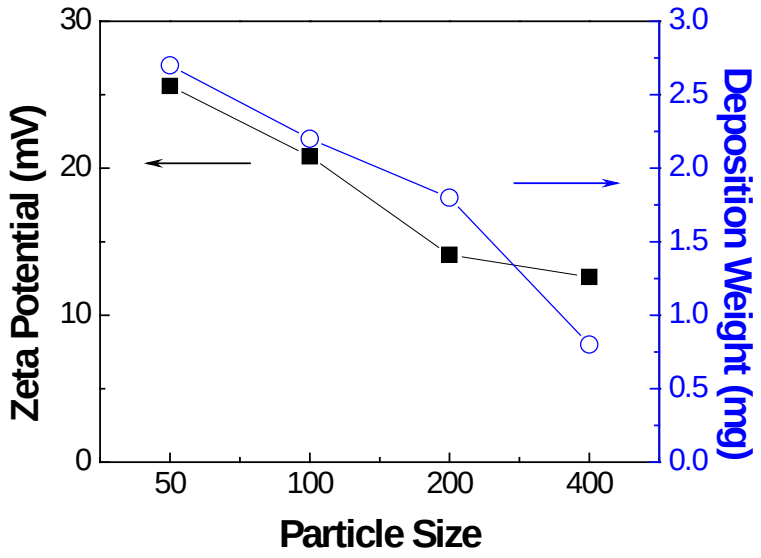

Figure 33. Zeta potential and deposition weight of ZnO nanoparticles dispersed in ethanol.

The kinetic equation proposed by Hamaker [20] can also explain the effect of particle size on the deposition behavior. The equation shows that the deposition weight (W) follows a linear function of the reaction time:

$$W(t) = C\mu AEt \qquad \text{(Equation 12)}$$

where the electrophoretic mobility is μ, the electric field is E, the deposition area is A, the particle mass concentration in the suspension is C, and the deposition time is t. Once stable suspensions are obtained, the electrophoretic mobility (μ) is directly proportional to the zeta potential (ζ):

$$\mu = \frac{\xi\varepsilon}{4\pi\eta} \qquad \text{(Equation 9)}$$

where ε is the permittivity and η is the viscosity of the suspension. Therefore, a slower deposition for larger particle can be attributed to the reduced electrophoretic mobility driven by the zeta potential.

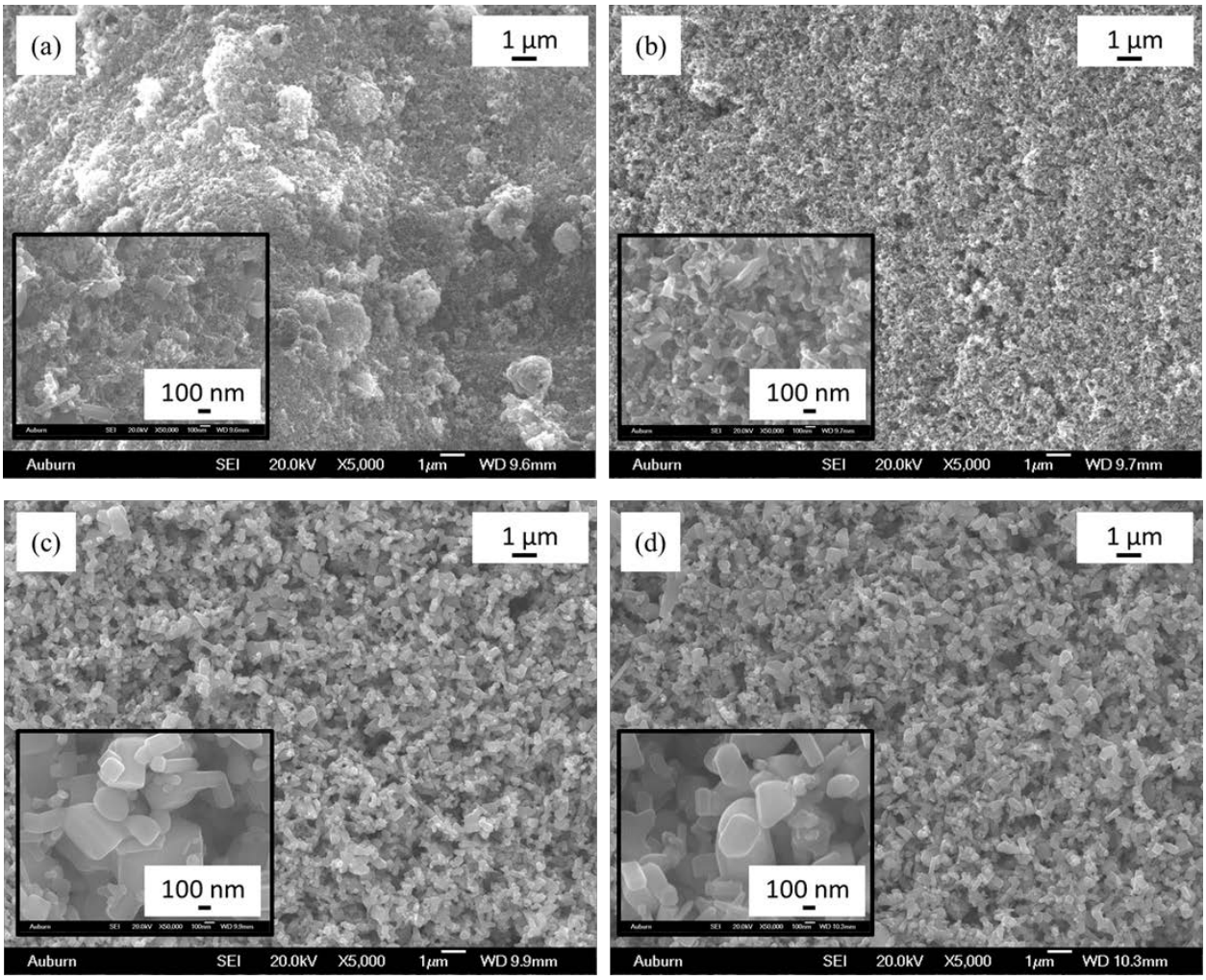

Figure 34. SEM images of deposited ZnO layers prepared from different sizes of ZnO. For average particle size of (a) 50 nm, (b) 100 nm, (c) 200 nm and (d) 400 nm.

Figure 34 shows the morphologies of the ZnO layers deposited from ZnO nanoparticles with average sizes of 50, 100, 200 and 400 nm. A smaller size of the ZnO particles gives a denser and less porous microstructure compared with a larger size of the ZnO particles. A dense microstructure for smaller particles in electphoretically deposited oxide layers can be found in previous reports. Sato *et al*. [114] deposited an yttrium barium copper oxide (YBCO) superconducting film from micronsized and submicron-sized particles by using the EPD method.

The film fabricated from a micron powder showed a porous structure. Farnoush *et al*. [106] performed EPD with submicron-sized and nano-sized hydroxyapatite. Large pores were shown in submicron samples compared with nano-sized samples. In addition, a rougher surface was obtained for the submicron sample. To determine the density of the ZnO deposit layers, we used Archimedes' principle. The calculated density decreased with increasing particle size as shown in Figure 34.

Based on the density calculation, the measured porosity was estimated at around 30 in the film formed from 50 nm particles to 50% in the films formed from 400 nm particles. Such effective packing in the film from smaller ZnO particles can result in more deposition weight, as shown in Figure 33.

The types of substrates for EPD deposition were investigated by coating ZnO nanoparticles on stainless steel planar substrates and flexible fabrics. The weight gains of the samples deposited on planar and fabric substrates were measured as functions of the applied voltage, as shown in Figure 35. The weight gains of ZnO deposited on both planar and fabric substrates increased linearly with the applied voltage. In particular, the deposition rate on the stainless steel planar substrate showed good agreement with the values predicted from Hamaker's equation (Eq. (1)). At higher voltages above 30 V, ZnO layers showed lower deposition rates than the predicted values. A reduced potential due to shielding with progressing deposition can lower the deposition rate [6]. However, the larger deposition weights of the ZnO nanoparticles on the both copper-plated fabric and the carbon fabric were observed and compared with those of the ZnO nanoparticles on planar substrate. The larger surface area of the fabric due to its non-flat and porous structure allows more deposition of ZnO nanoparticles in the fabric. When the surface area of each fabric substrate is estimated from the Hamaker equation, the surface areas of the

carbon fabric and the copper-plated fabric are estimated to be 1.5 and 1.2 times that of the planar stainless steel, respectively.

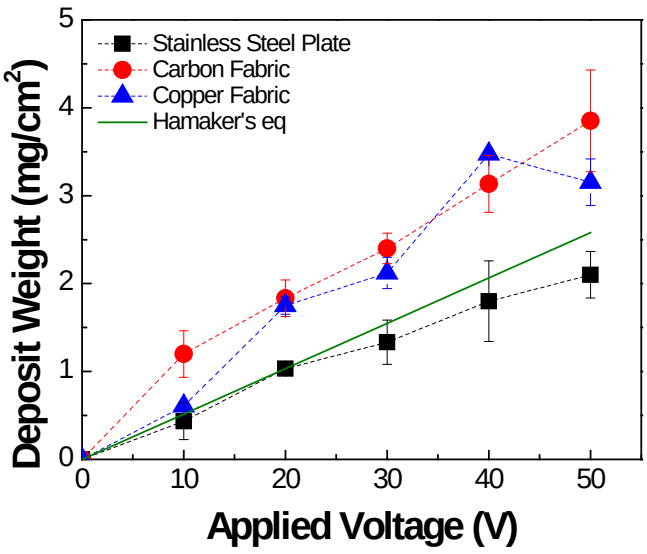

Figure 35. Deposited weight of ZnO nanoparticles fabricated by using EPD on a stainless steel planar substrate, a carbon fabric, and a copper-plated fabric as functions of the applied voltage.

The morphologies of ZnO layers on stainless steel plate, carbon fabric and copper-plated fabric are shown in Figure 36 (a)−(c). ZnO nanoparticles were uniformly deposited irrespective of substrate type, but fabric substrates yielded higher deposition rates, as presented in Figure 35. The result implies that the high deposition rate is due to the large surface area due to the woven textile structure. Careful observation from the SEM photo shows that the surface of an individual fiber, even in the inner layer of the woven fabric is uniformly coated with ZnO nanoparticles, as shown in Figure 36 (d).

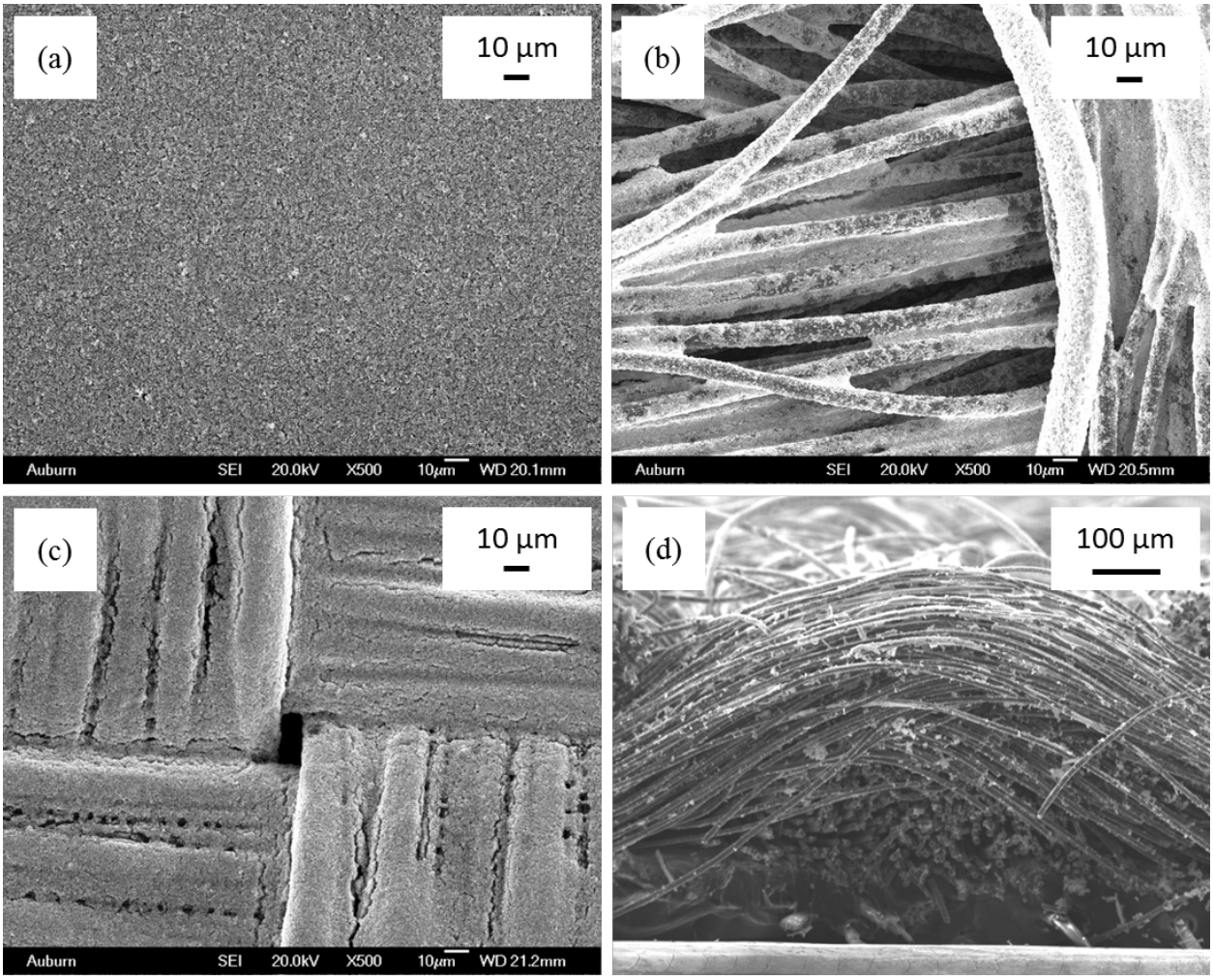

Figure 36. SEM images of ZnO layers by using EPD (a) on stainless steel planar substrate at 50 V, (b) on carbon fabric at 50 V, (c) on copper-plated fabric at 50 V, and (d) cross section of the copper-plated fabric at 50 V.

Because the EPD process uses suspended particles in a liquid medium, charged particles due to the electric field can easily penetrate through the spaces in the textile structure and be deposited on each fiber of the fabric. The ability to coat particles on complex shapes by using EPD has been used to produce fiber-reinforced ceramics and ceramic matrix composites. Boccaccini *et al.* [115] demonstrated uniform infiltration of titania and alumina particles on carbon and stainless

steel fibers. Recently, Wang and Dryfe [116] fabricated a porous structure of a hybrid graphene-carbon-nanotube layer on carbon cloth by using EPD to demonstrate flexible supercapacitors. Thus, EPD is capable of coating multifunctional oxides on flexible and wearable substrates.

The deposited ZnO particles on three different substrates were examined by using XRD, and the results were compared with those for the raw ZnO powder, as shown in Figure 37. All samples show XRD patterns consistent with ZnO of a zincite structure (JCPDS 36-1451). When the raw ZnO powder and the powder deposited by using EPD were employed, no peak shifts were found. It indicates that suspended ZnO particles contribute to deposition on the substrate without chemical reactions during the EPD process. Therefore, the XRD patterns of the deposited ZnO on three different substrates show only the peaks of ZnO and the substrates without any preferred orientation.

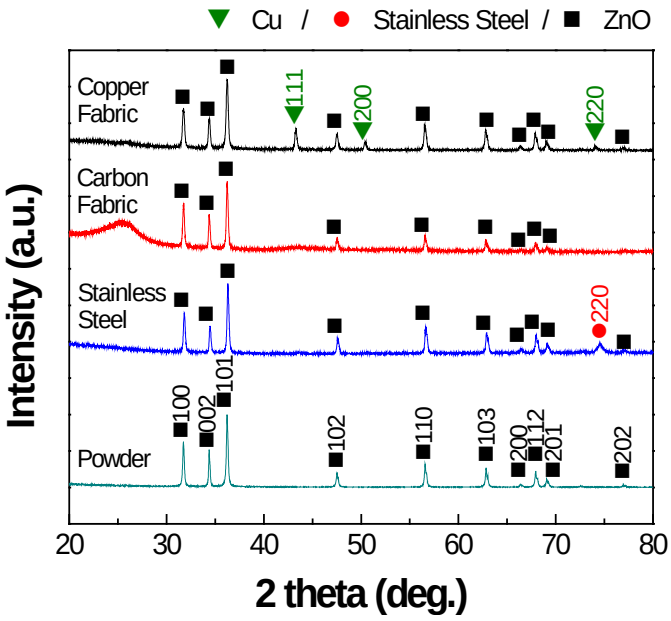

Figure 37. XRD patterns of raw ZnO nanoparticle and electrophoretically deposited ZnO layers on stainless steel planar substrate, carbon fabric, and copper plated fabric.

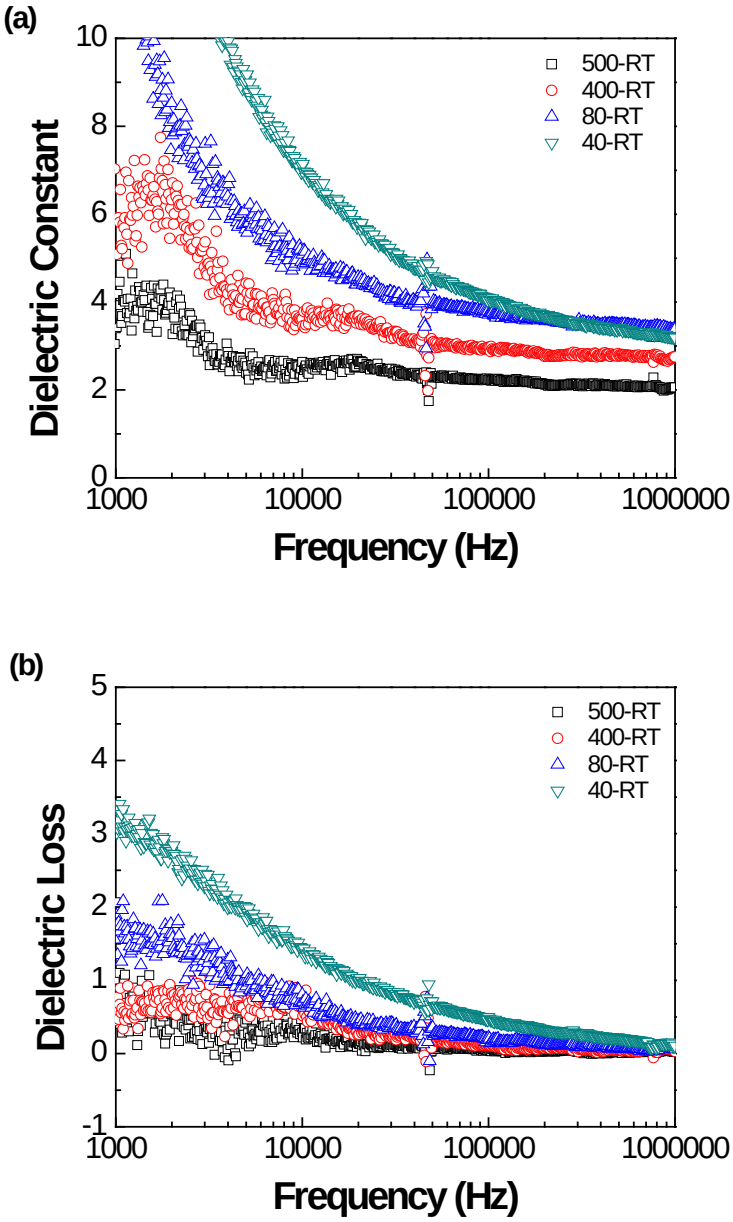

Figure 38. (a) Dielectric constant and (b) dielectric loss versus frequency of ZnO layers deposited from different sizes of ZnO particles.

The dielectric constant and the dielectric loss of the deposited ZnO layers dried at room temperature were measured in the 1 kHz − 1 MHz frequency range, as shown in Figure 38. The dielectric constants of the ZnO layer deposited from different particle sizes decrease with

increasing frequency and become almost flat at frequencies above 10 kHz. At 10 kHz, the dielectric constants increase from 2.2 to 4.1 with decreasing particle size from 500 nm to 40 nm. The measured values are lower than the reported value in sintered and bulk ZnO, $\varepsilon bulk$ = 8.66 [117], but they are comparable to the values reported for nanostructured ZnO [118, 119]. Another reason for the smaller dielectric constant in ZnO deposited from larger particles is related to low particle packing density. As more pores are introduced in the deposited ZnO, its dielectric constant decreases due to the added volume of air in the following equation describing a mixture of two parallel layers of dielectrics,

$$\varepsilon' = V_1\varepsilon_1 + V_2\varepsilon_2 \quad \text{(Equation 10)}$$

where $\varepsilon\_$ is the dielectric constant of the composite, V_1 and V_2 are the volume fractions of phases 1 and 2, respectively, and ε_1 and ε_2 are the dielectric constants of the phases [120]. As observed in Figure 34, the smaller particles show denser structures with fewer pores. Thus, controlling the deposition morphology by using the EPD process is critical in determining the dielectric properties.

5.4 Summary and conclusions

EPD was performed to deposit ZnO nanoparticles on conductive fabrics and plates from a ZnO-ethanol suspension system. The deposition behavior of ZnO nanoparticles was examined by varying the applied voltage and compared using a kinetic equation. The deposition rate increased with as particle size decreased due to an enhanced zeta potential. Although the deposition weight showed a linear relationship with applied voltage, the rough surface or larger surface area of woven fabric yielded a higher weight gain than a flat plate substrate.

The dried morphology of ZnO nanoparticle layers showed uniform at lower applied voltage, but higher voltage corresponding to a faster deposition rate caused cracks on the surface during drying. ZnO layers without preferred orientation was confirmed by XRD. Such variation in the particle packing density influenced the dielectric properties. Smaller particle size gave a denser structure in the deposited ZnO layer, and the denser structure enhanced the dielectric constant. A UV-Vis DRS showed good UV blocking properties and energy bandgap comparable to reported values. PL and Raman spectra also show similar results with bulk ZnO. Although the values in PL, UV, and Raman spectra were slightly shifted compared with bulk ZnO, this difference can be attributed to smaller particle size and defects in the as-deposited ZnO layer. EPD can be an effective method for uniform deposition of ZnO nanoparticles onto fabrics at lower temperatures. This EPD method will be useful for developing multifunctional devices on flexible substrates.

Chapter 6. Development of synthesis methods for ZnO and NiO

6.1 Introduction

A number of researchers have investigated various methods of synthesizing metal oxide nanostructures, including chemical [33-35], electrochemical [35, 36], and physical deposition techniques [37, 38]. Among many nanosized metal oxide preparation routes, a solution based synthesis method [34, 35] was chosen for this research. Since an important issue in synthesizing nanoparticles is preventing agglomeration of particles, a low processing temperature is preferred. Among metal oxides, diverse morphologies of ZnO crystal structures by the precipitation method are well known to be possible at relatively low processing temperatures [34, 35, 39]. On the other hand, in order to control different morphologies of NiO by a simple operation, some researchers have reported using a hydrothermal method. B. Liu *et al*. [95], B. Miao *et al*. [13], and L. Lin *et al*. [96] suggested a $NiCl_2$-$Na_2C_2O_4$-H_2O hydrothermal system with polyethylene glycol, ethylene glycol, and glycine as surfactants. In their work, different aspect ratios of NiO nanostructures were obtained with varying types of surfactant and hydrothermal conditions.
In this work, synthesis of ZnO by a precipitation method and NiO by a hydrothermal method is studied with controlling morphology to apply the in-situ EPD process.

6.2 Experimental method

6.2.1 ZnO by a precipitation method

ZnO hollow microspheres were prepared by a simple precipitation method. For the synthesis of porous and hollow microsphere zinc oxide, zinc nitrate hexahydrate ($Zn(NO_3)_2 \cdot 6H_2O$, Fisher Chemical), hexamethylenetetramine (HMT, $C_6H_{12}N_4$, Aldrich), and sodium citrate ($Na_3C_6H_5O_7$, Sigma-Aldrich) were used as starting materials. Zinc nitrate was used as a zinc source. HMT provided hydroxyl ions. 0.01 M of zinc nitrate, 0.01 M of HMT, and 0.002 M of sodium citrate were stirred in DI water. The mixed solution was kept in a hot water bath (Iso Temp 202, Fisher Scientific) at 70 °C for 3 hours and dried at 85 °C overnight. The resulting precipitates were collected and washed several times with DI water. After drying, the precipitates were calcined with a tube furnace (Lindberg/Blue M) at 300 °C for 1 hour.

The morphology of the particles was examined with a scanning electron microscope (SEM, JEOL JSM-7000F) and transmission electron microscopy (TEM, Tecnai G2 F30 S-Twin). The crystalline phase of the ZnO was analyzed by X-ray diffraction (XRD, Bruker D8 Discover). Chemical bonding structure was analyzed by FTIR (Fourier transformation infrared) and the bonding change was analyzed by DSC (differential scanning calorimetry).

6.2.2 NiO by a hydrothermal method

Two different morphologies of NiO particles were prepared by a hydrothermal method. 1.6638 g of nickel chloride ($NiCl_2$, Alfa-Aesar) and 0.9948 g of ammonium oxalate ($(NH_4)_2C_2O_4$, Sigma-Aldrich) were separately dissolved and mixed in 10 ml of distilled water. 1 ml of triethanolamine (TEA, Sigma) was added into one solution for altering NiO morphology. Both solutions were

transferred to Teflon containers and autoclaved. The two batches of resulting precipitate were collected, washed several times with water, and then calcined at 300°C for 1 hour.

X-ray diffraction (XRD) was used to characterize the crystalline phase and phase transition of the synthesized powders. The morphology of the deposited NiO particles was examined with a scanning electron microscope (SEM).

6.3 Results and discussion

6.3.1 ZnO porous and hollow microspheres by a precipitation method

According to the DSC profile of the as-precipitated powder, as-precipitates decomposed as shown in Figure 39. On the DSC curve, a sharp exothermic of decomposition was observed between 350 and 400 °C. According to the DSC result, the calcination temperature was determined to be 500 °C for the fully transformed process.

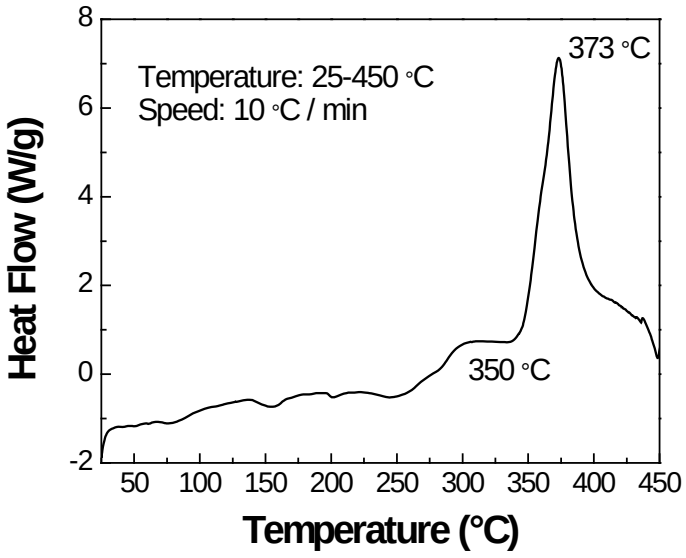

Figure 39. DSC profile of as-precipitated powder (zinc citrate)

Figure 40 shows the XRD pattern of as-precipitated and calcined powders from citrate ion modified ZnO. In Figure 40 (a), the diffraction result of the as-precipitated powders by a precipitation method showed amorphous structure, so it was considered to be zinc citrate [90]. In Figure 40 (b), the diffraction peaks of powders after calcination at 500 °C present pure ZnO phase (XRD JCPDS data file No. 36–1451) indexed as (100), (002), (101), (102), (110), (103), (200), (112), (201), and (202) lattice planes, respectively.

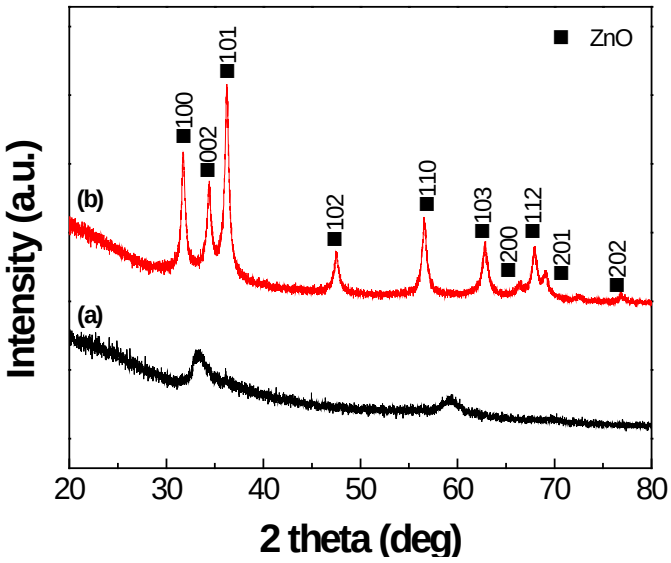

Figure 40. XRD patterns of (a) as-precipitated and (b) calcined powders from citrate ion modified ZnO.

Figure 41 shows the FTIR spectra of as-precipitated and calcined powders from citrate ion modified ZnO. FTIR spectra of an as-precipitate sample, as shown in Figure 41 (a), showed a similar result to those reported in previous literature [90]. The FTIR spectra showed strong and sharp absorption bands for the carboxylate groups of the coordinated citrates. Antisymmetric stretching vibrations, $\nu_{asym}(COO^-)$, were observed between 1568 and 1564 cm^{-1}. Symmetric

stretching vibrations, $\nu_{sym}(COO^-)$, appeared between 1414 and 1406 cm^{-1}. In addition, a strong absorption band at 3500 cm^{-1} was attributed to the vibration of the hydroxyl group of adsorbed water. This result showed that citrate ions were participated in the reaction. As shown in Figure 41 (b), the sample which was calcined at 500 °C had a strong absorption band below 500 cm^{-1}, a characteristic which corresponds to the E_2 mode of hexagonal ZnO (Raman active) [121]. The conversion of amorphous zinc citrate into crystalline zinc oxide was confirmed by XRD and FTIR.

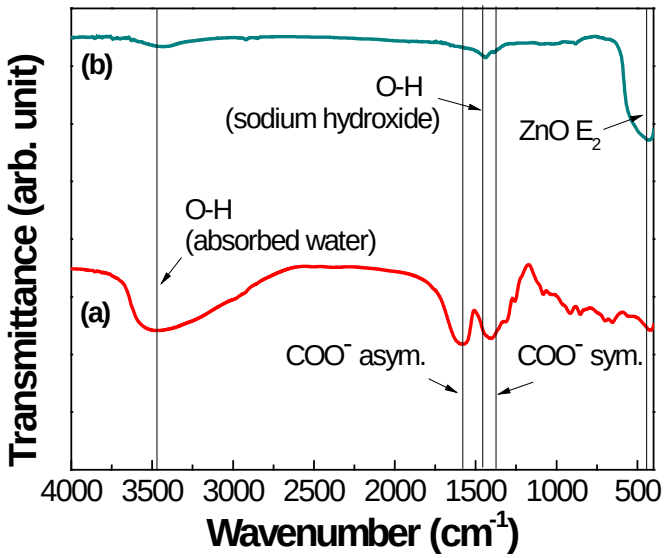

Figure 41. The FTIR spectra of (a) as-precipitated and (b) calcined powders from citrate ion modified ZnO.

Figure 46 shows SEM and TEM images of citrate ion modified ZnO by a precipitation method. The surface morphology of the as-precipitated particles shown in Figure 42 (a) presents as microspheres. As shown in Figure 42 (b), there was no obvious change of the particle morphology or diameter after calcination at 500 °C. Hemispheres appeared as well as

microspheres. For further understanding of hollow structure, TEM images were also analyzed. The morphology of the hollow shell structures was confirmed as shown in Figure 42 (c). The SAED patterns in Figure 42 (d) indicates that ZnO hollow microspheres are polycrystalline. Figure 43 shows the particle size distribution of ZnO hollow microspheres obtained from the SEM image. The SEM images revealed distribution parameters of an average diameter of 1.7±0.5 µm.

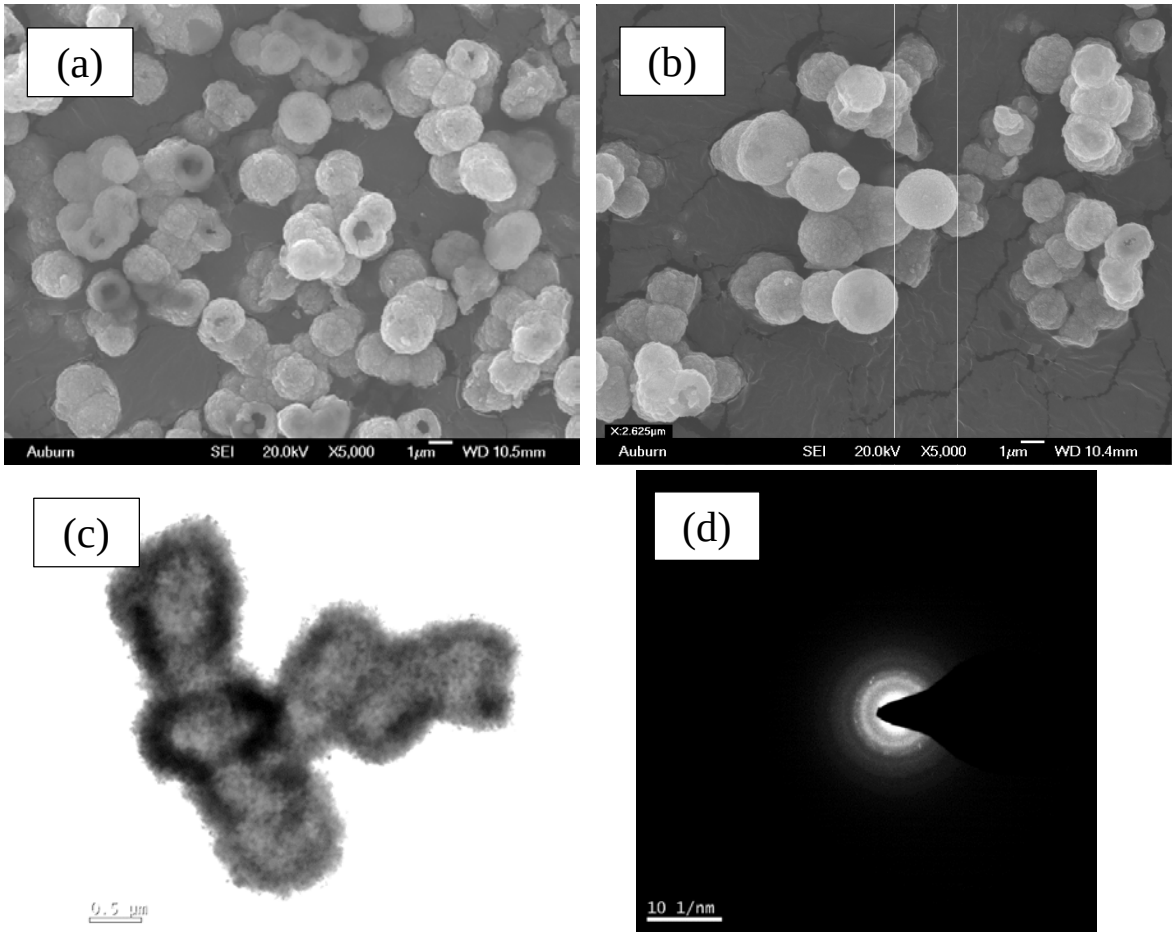

Figure 42. SEM image of (a) as-precipitated powders and (b) calcined powders, (c) TEM image of calcined powders, and (d) diffraction patterns of TEM.

The specific surface area (BET) was measured. The ZnO hollow microspheres had a BET surface area of 27.86 m^2/g. This value is larger than that of different forms of nano-structured ZnO such as nanorods and dendelions [122] and is comparable to previously reported values of ZnO hollow spheres [94, 122, 123], as summarized in Table 5.

Table 5. Specific surface area (BET) (m^2/g) of ZnO hollow microspheres.

Morphology	BET surface area (m^2/g)	Ref
ZnO dendelions	8.19	[122]
ZnO nanorods	12	[122]
ZnO hollow spheres	18.7	[122]
	17	[123]
	28.48	[94]
	27.86	This work

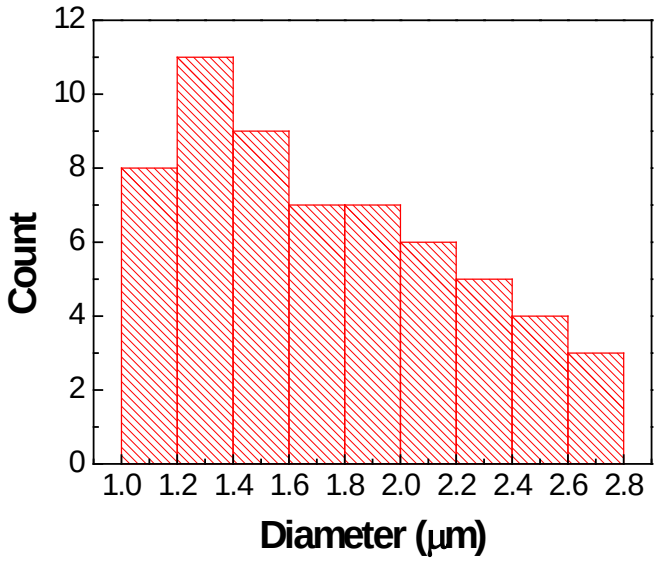

Figure 43. Particle size distribution of ZnO hollow microspheres: Histogram obtained from the SEM image.

According to the literature [90, 91], Ostwald ripening is the growth mechanism of hollow microsphere structures. ZnO hollow microspheres were obtained from zinc citrate solid microspheres through the Ostwald ripening mechanism, which occurs when smaller particles are dissolved and deposited on larger particles. The driving force of this phenomenon in particle growth is the solubility difference between larger particles and smaller particles [90, 91].

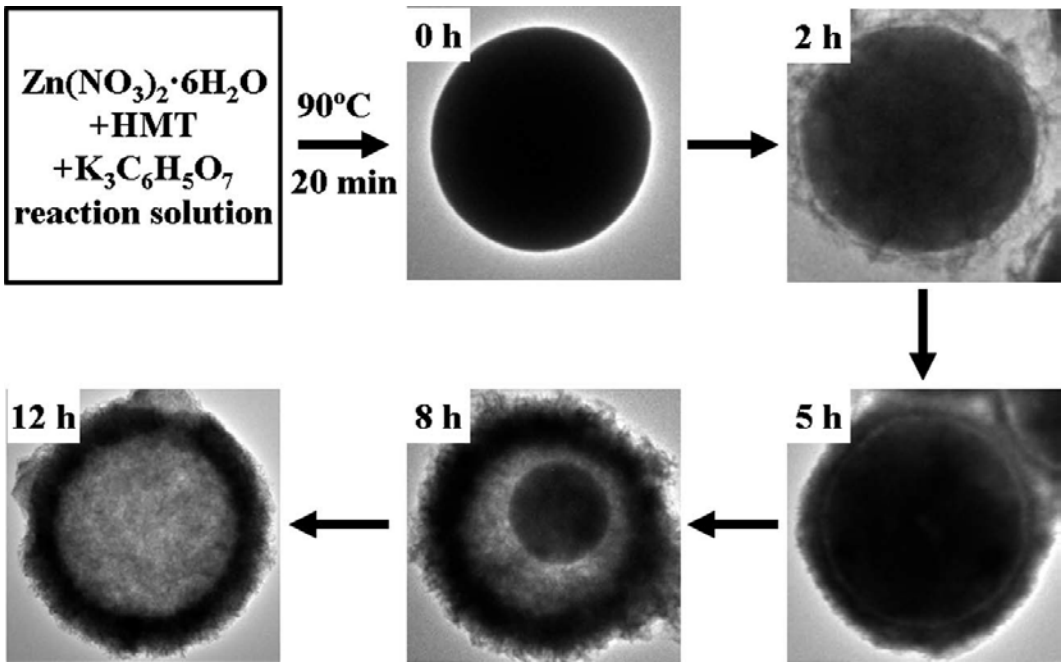

Figure 44. A schematic illustrating the evolution of the morphology for the zinc citrate microspheres with aging time (the aging time is indicated) [90].

The growth mechanism of ZnO hollow microspheres in this work can be explained based on the work by Xie *et al*. [90] as illustrated in Figure 44. After the solution was removed from the 70°C water bath, the reaction did not stop immediately, but the reaction rate slowed significantly due to the decreasing solution temperature. Thus, the initial solid microspheres grew continuously, and zinc citrate flocs formed on the surface of the solid microspheres due to the supersaturated

concentration of zinc citrate in solution. During the drying process, the flocs on the surfaces of the solid microspheres formed a dense and thick shell. This shell formation continued until a concentration of the previously supersaturated zinc citrate in solution reached equilibrium with that of solid zinc citrate. Then the shells begin redeposition by dissolving the inner cores into the solution and the shells become thicker, resulting in hollow microspheres.

6.3.2 Different morphologies of NiO by a hydrothermal method

Figure 45 shows the XRD pattern of as-synthesized precipitates and calcined powders from pristine and TEA-modified solutions.

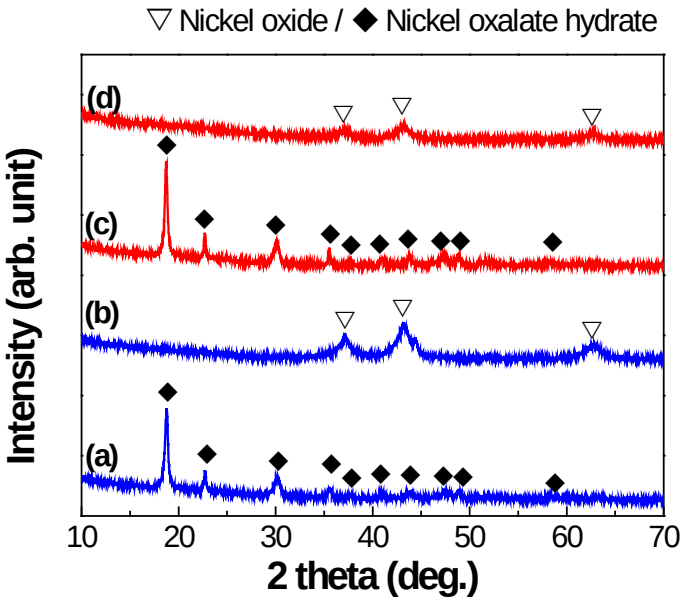

Figure 45. XRD patterns of (a) as-synthesized precipitates without TEA, (b) after calcination, (c) as-synthesized precipitates with TEA, and (d) after calcination.

The diffraction peaks of the as-synthesized powders by a hydrothermal method without TEA (Figure 45 (a)) and with TEA (Figure 45 (c)) correspond to those of nickel oxalate hydrate

(NiC_2O_4, XRD JCPDS data file No. 25–0582). The diffraction peaks of both powders after calcination at 300 °C present pure and cubic phase of NiO (XRD JCPDS data file No. 47–1049) indexed as (111), (200), and (220) lattice planes, respectively.

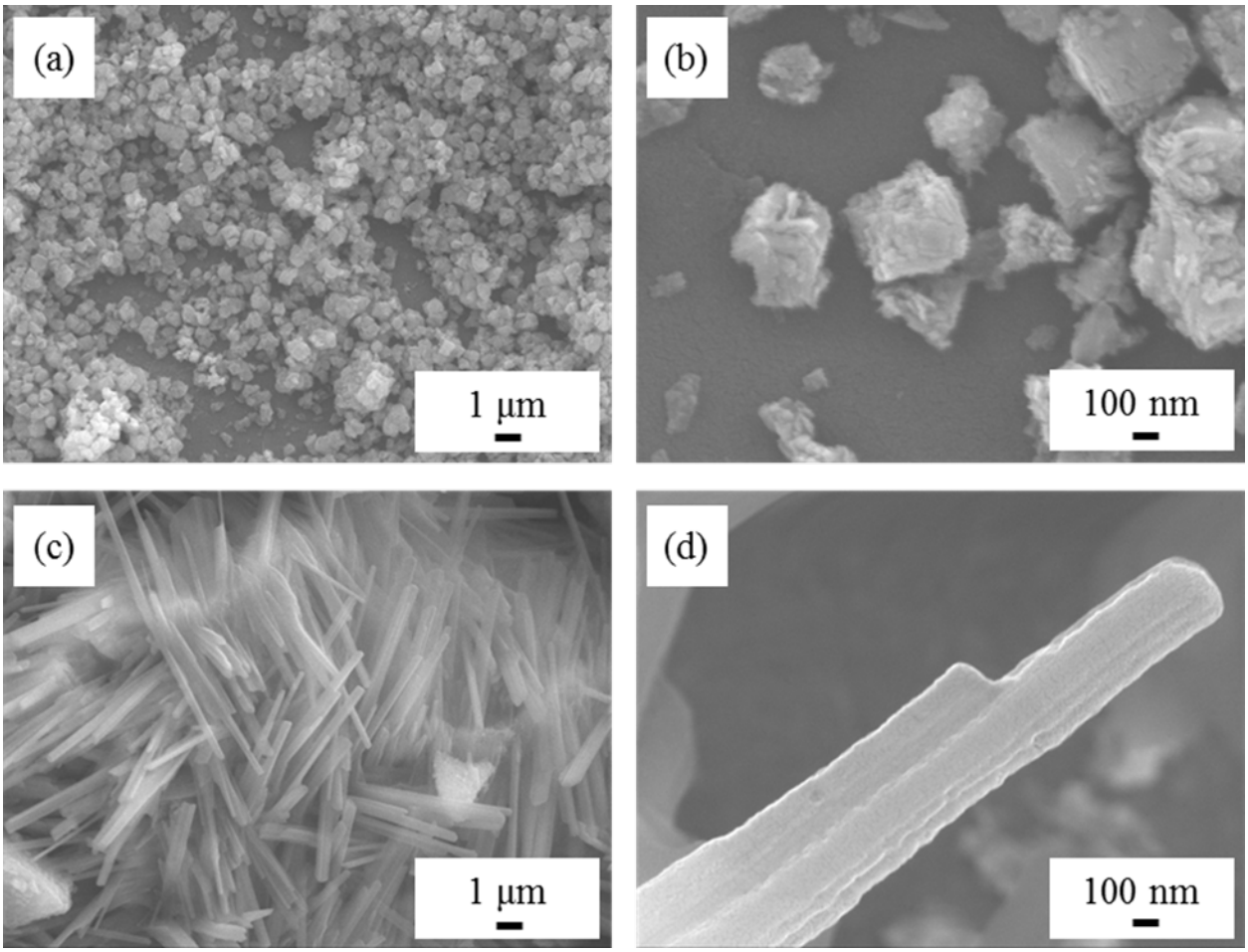

Figure 46. SEM images of synthesized NiO by hydrothermal method (a) without TEA after calcination, (b) enlarged part of (a), (c) with TEA after calcination, and (d) enlarged part of (a).

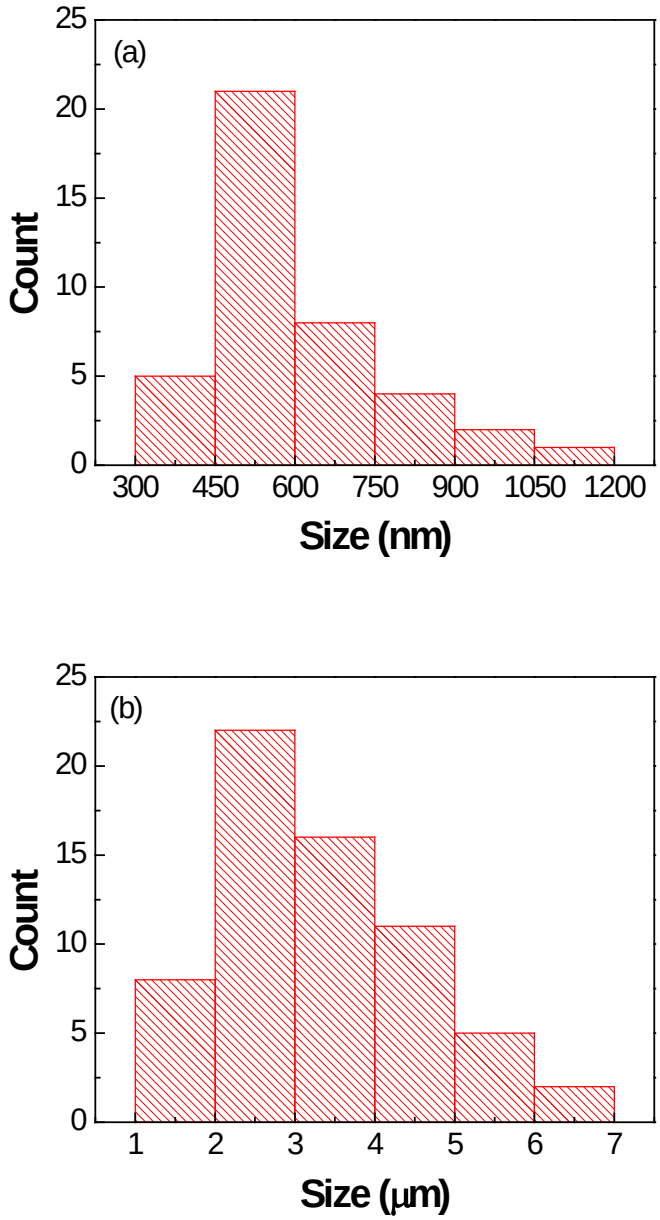

Figure 47. Particle size distribution of NiO (a) cube-like shape without TEA and (b) needle-like shape with TEA: Histogram obtained from the SEM image.

Figure 46 shows SEM images of calcined NiO by a hydrothermal method from the solution with and without TEA. The surface morphology of the resulting particles from the solution without TEA after calcination at 300 °C, as shown in Figure 46 (a-b), presents as a cube-like shape. As

shown in Figure 46 (b), each particle has a rough surface. In Figure 46 (c), the particles synthesized from the solution without TEA show a needle-like shape after calcination at 300 °C. As shown in Figure 46, the SEM images revealed the distribution parameters of cube-like NiO (Figure 47 (a)) with an average size of 0.61±0.15 μm and needle-like NiO (Figure 47 (b)) with an average size of 3.35±1.27 μm. For further understanding of the role of surface area, the specific surface area (BET) was measured. The sample synthesized with TEA has a BET surface area of 171.8 m^2/g, while the sample without TEA has a smaller BET surface area of 64.3 m^2/g. The method of synthesizing NiO nanowire mainly focused on the thermal decomposition of $NiC_2O_4 \cdot H_2O$. The $NiC_2O_4 \cdot H_2O$ nanowire was synthesized by a hydrothermal reaction of $NiCl_2$ with NaC_2O_4 and H_2O, with polyethylene glycol (PEG) and ethylene glycol (EG) added as surfactants [13, 95, 96]. B. Liu *et al*. [95] suggested a possible formation mechanism of $NiC_2O_4 \cdot H_2O$. $NiC_2O_4 \cdot H_2O$ nanoparticles, which have monoclinic structure, grow along the [101] direction and the basal and lateral planes are $(10\bar{1})$ and (010), respectively. Thus, without any surfactants, rod-like $NiC_2O_4 \cdot H_2O$ can be obtained. The addition of different surfactants can selectively control the growth of a specific crystal plane. In the presence of EG, $NiC_2O_4 \cdot H_2O$ nanowires can be obtained because the adsorption of EG on $(10\bar{1})$ and (010) planes promotes growth along the [101] direction. However, the $NiCl_2$-$Na_2C_2O_4$-H_2O-EG hydrothermal system may form nanowire bundles due to electrostatic attraction between two $NiC_2O_4 \cdot H_2O$ nanowires and EG. To avoid gathering, B. Miao *et al*. [13] introduced both EG and PEG as surfactants. PEG not only promotes crystallization along the [101] direction but also restrains the formation of nanowire bundles. Some research has reported the use of triethanolamine (TEA) as an additive to form rod and wire structures of metal and metal oxides [14, 124-126]. However, the possible formation mechanism of rod/wire-like NiO assisted by TEA has not been intensively studied.

Based on the mechanism of $NiCl_2$-$Na_2C_2O_4$-H_2O-EG hydrothermal system [95], the chemical reaction of $NiCl_2$-$(NH_4)_2C_2O_4$-H_2O-TEA hydrothermal system can be formulated as follows:

$$NiCl_2 + (NH_4)_2C_2O_4 \rightarrow NiC_2O_4 + 2NH_4Cl, \quad \text{(Equation 11)}$$

$$NiC_2O_4 + TEA \leftrightarrow [Ni(TEA)]^- + 2CO_2, \quad \text{(Equation 12)}$$

$$2NiC_2O_4 + O_2 \rightarrow 2NiO + 4CO_2. \quad \text{(Equation 13)}$$

TEA is a multidentate ligand with three –OH groups and one amine group. In the presence of TEA molecules, they may interact with Ni^{2+} to form a Ni-TEA complex, $[Ni(TEA)]^-$. This Ni-TEA complex may promote the formation of NiC_2O_4 with a higher aspect ratio.

6.4 Summary and conclusions

Synthesis of ZnO and NiO was studied with controlling morphology to apply the in-situ EPD process. Hierarchically structured ZnO was synthesized by a simple precipitation method with the addition of sodium citrate. A simple hydrothermal method was successfully implemented to synthesize NiO with tailored morphology using TEA.

When citrate ion was added to the solution for a precipitation method, hollow microsphere ZnO was fabricated. After calcination at 500 °C for 1 hour, as-precipitated particles were transformed from amorphous zinc citrate to polycrystalline ZnO phase. The citrate ions participated in the reaction and formed porous and hollow microspheres with significantly large surface areas.

When TEA was added to a solution for a hydrothermal method, highly anisotropic needle-like NiO particles were grown. After calcination at 300 °C for 1 hour, as-synthesized precipitates were transformed from NiC_2O_4 to pure NiO phase. The presence of TEA may promote the formation of NiC_2O_4 with a higher aspect ratio.

Chapter 7. Gas sensing property of different morphologies of metal oxides

7.1 Introduction

Over the past few years, researchers have intensively investigated highly miniaturized gas sensor systems that could be integrated into wearable and flexible devices. For example, a wearable breath monitoring system with integrated gas sensors would allow continuous monitoring of patients' breath gases such as acetone gas for diabetes [40], ammonia for renal disease [41], and ethanol for hepatic steatosis [42]. Therefore, a great demand exists for diverse sensing materials with good selectivity and sensitivity that could be integrated into wearable/flexible substances. Semiconducting nano-scale metal oxides such as tin oxide [10], zinc oxide [1], nickel oxide [11], and copper oxide [12] have been developed as gas sensors that measure the change in electrical conductivity upon exposure to the gas. Among them, zinc oxide, which shows n-type behavior, is an excellent candidate because of its electric properties such as wide band gap and high electron mobility [1, 39, 71]. Various morphologies for ZnO nanostructures such as nanorods, nanotubes, and nanowires have been investigated to understand morphology-driven properties. Recently, researchers have fabricated hollow micro/nanosphere ZnO and investigated its properties [90, 91]. Such a structure has a large surface-to-volume ratio and reduced transport lengths for both mass and charge transport, making it suitable for applications such as dye-sensitized solar cells, photocatalts, high performance electrodes, and gas sensors [90-94]. J. Rao et al. [94] investigated precision detection of ethanol and acetone with low concentration. The gas response values of ZnO hollow microspheres are 2.2 in 5 ppm ethanol and 2 in 5 ppm acetone, respectively. Some

researchers have reported enhanced gas selectivity of ZnO hollow microspheres. D. Wang et al. [91] achieved good selectivity to ethanol with hierarchical hollow ZnO microspheres. In addition, these microspheres showed a fast response time of 1 sec and a fast recovery time of 19 sec. Also, X. Li et al. [93] found that ZnO hollow microspheres showed significant selectivity toward alcohols such as methanol and ethanol. Those results indicated that the mesoporous and hollow structure of a ZnO microsphere can enhance its gas sensitivity and selectivity.

On the other hand, nickel oxide shows a p-type semiconducting behavior. Despite some shortcomings, p-type oxide semiconductors have great potential for use in gas sensors due to their reliable and reproducible switch in electrical conductivity between the air atmosphere and target gas, chemical stability with a highly electroactive nature, and low cost and toxicity [12, 13, 43, 95, 96]. Some researchers have reported enhanced gas selectivity of p-type oxide semiconductors. H. -J. Kim *et al*. [17] achieved high selectivity and response to xylene and toluene with 1.15 at% Cr-doped NiO hierarchical nanostructures. K. -M. Kim *et al*. [97] investigated the gas selective detection of pure CuO nanosheets and Cr-doped CuO nanorods. They found that 2.2 at% Cr-doped CuO nanorods showed highly sensitive and selective detection of NO_2. The results indicate that the selectivity and sensitivity of p-type oxide semiconductors can be enhanced with the combination of dopants.

In addition, heterostructured gas sensors using oxide p-n junctions have been one of the most promising areas of research because various combinations of p- and n-type oxide semiconductors have demonstrated higher performance than those with only one of the two types [43]. C. W. Na *et al*. [98] found that n-type ZnO nanowire with p-type NiO nanoparticles showed significantly enhanced gas response. H. -R. Kim *et al*. [47] suggested that NiO-functionalized SnO_2 hollow spheres achieved rapid recovery. Decorating p-type oxide semiconductors on n-type oxide

semiconductors can enhance not only the gas response and selectivity but also the recovery kinetics by transferring charge carriers between p- and n-type oxide semiconductors. Currently, the NiO films fabricated by physical and chemical vapor deposition and electrochemical deposition [127-130] are widely used for gas sensing application. However, in order to control different morphologies of NiO by a simple operation, some researchers have reported using a hydrothermal method. B. Liu *et al*. [95], B. Miao *et al*. [13], and L. Lin *et al*. [96] suggested a $NiCl_2$-$Na_2C_2O_4$-H_2O hydrothermal system with polyethylene glycol, ethylene glycol, and glycine as surfactants. Different aspect ratios of NiO nanostructures were obtained with varying types of surfactant and hydrothermal conditions.

In this study, NiO particles with different morphologies were investigated by a new $NiCl_2$-$(NH_4)_2C_2O_4$-H_2O-TEA hydrothermal system to form different aspect ratios of NiO nanostructures. In-situ electrophoretic deposition (EPD) was also explored to construct uniform hierarchically structured NiO films. Ethanol-sensing characteristics of the films were investigated to examine morphological properties of NiO particles.

7.2 Experimental method

7.2.1 Preparation of materials

The synthesis process of ZnO hollow microspheres, NiO cubes, and NiO rods are described in 6.2.

In addition, to study the effect of silver as a catalyst, silver particles were decorated on the surface of ZnO hollow microspheres as shown in Figure 48. Synthesized ZnO hollow microspheres were dispersed in 0.8 mM of silver nitrate solution for 12 hours. The resulting

powders were collected and washed several times with DI water. The crystal structure and morphologies of prepared powder samples were characterized by XRD, SEM, and EDS.

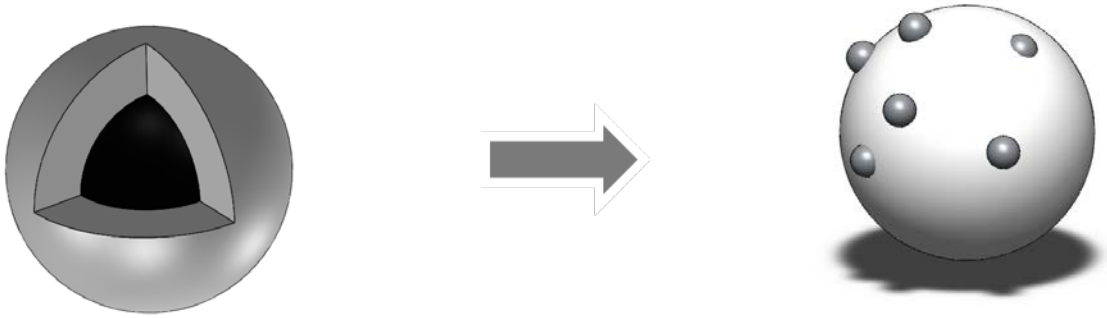

Figure 48. A schematic of the silver decoration on the ZnO hollow microspheres

To further compare gas sensing properties of different morphologies of NiO, flake-like NiO particles were prepared by a simple precipitation method. For the synthesis, nickel nitrate hexahydrate ($Ni(NO_3)_2 \cdot 6H_2O$, Alfa Aesar) and sodium hydroxide (NaOH, Sigma-Aldrich) were used as starting materials. The solution was mixed in DI water and kept in a hot water bath (Iso Temp 202, Fisher Scientific) at 75 °C for 3 hours and dried overnight. The resulting precipitates were collected and washed several times with DI water. After drying, precipitates were calcined with a tube furnace (Lindberg/Blue M) at 300 °C for 1 hour.

7.2.2 Preparation of electrodes

Prior to gas sensing measurement, a Pt electrode with an interdigitated pattern, using a stainless steel shadow mask, was deposited on a polyimide substrate by sputter deposition. Each sensing material, ZnO (hollow microspheres) and NiO (cubes, rods, and flakes), was then coated by electrophoretic deposition. The electrophoretic deposition setup used an interdigitated platinum

electrode as a working electrode and a stainless steel plate (1 cm × 1 cm × 0.25 mm) as a counter electrode. For suspensions, each sensing material, ZnO hollow microspheres, NiO flakes, NiO cubes, and NiO rods, was uniformly dispersed in ethanol by ultrasonication. The deposition was carried out at 50 V for 5 min at room temperature, resulting in a thin uniform layer of a sensing material.

7.2.3 Gas sensing measurement

Gas sensing properties were measured in a sensing chamber with flowing synthetic air, a mixture of 20% oxygen and 80% nitrogen, and characterized using 25 - 200 ppm of ethanol or acetone gas at 200 - 350 °C. Sensing response was recorded by using a Keithley Digital Sourcemeter (model 2400) and an automated data acquisition system.

7.3 Results and discussion

7.3.1 ZnO porous and hollow microspheres and their gas sensing properties

Figure 49 shows the XRD pattern of silver decorated ZnO hollow microspheres.

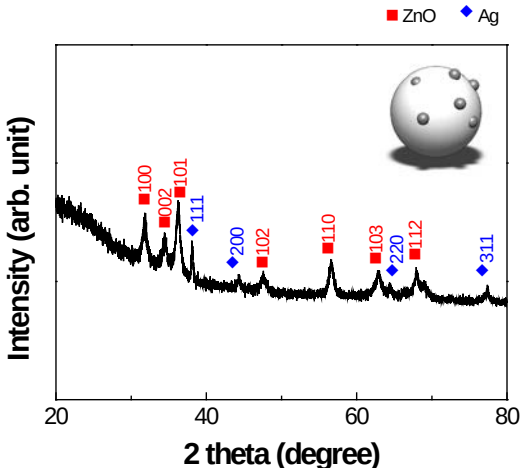

Figure 49. XRD pattern of Ag decorated ZnO hollow microspheres.

As shown in Figure 49, the diffraction peaks indicated a mixed crystal phases of ZnO and Ag. The peaks coincided with ZnO phase (XRD JCPDS data file No. 36–1451) and the rest of the peaks were indexed to Ag (XRD JCPDS data file No. 36–1451). No other phases corresponded to impurity. Figure 50 shows the EDS elemental mapping of the Ag decorated ZnO hollow microspheres. The signals of Ag were detected on the surface of the ZnO hollow microspheres.

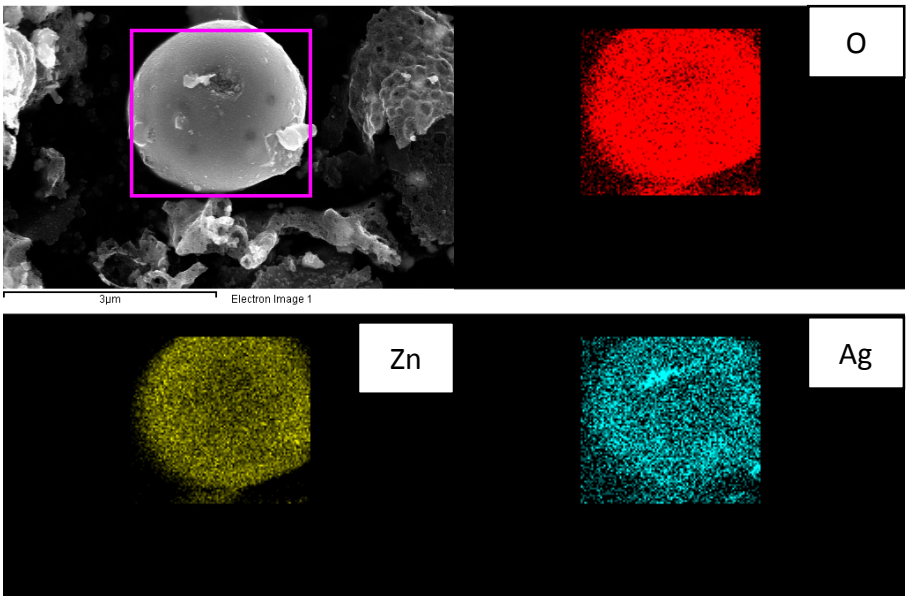

Figure 50. EDS elemental mapping of Ag decorated ZnO hollow microspheres.

The ethanol gas sensing characteristics of ZnO hollow microsphere films by EPD were studied by measuring resistance change. Figure 51 shows the resistance change of ZnO films against 100 ppm of ethanol with increasing temperature, 200-350 °C. Their gas response rates (R) were determined as the ratio of the resistance measured in detecting gas (Rg) to that measured in air (Ra). The optimum working temperature of this sensing system was determined to be 300 °C. This trend corresponds to the behaviors of semiconductor oxide gas sensors [44, 46]. A competition exists between slow kinetics at low temperatures and enhanced desorption at high

temperatures. Metal oxide gas sensors show a maximum gas response at certain operating temperatures; the maximum gas response of ethanol is obtained around 300 °C [131-135].

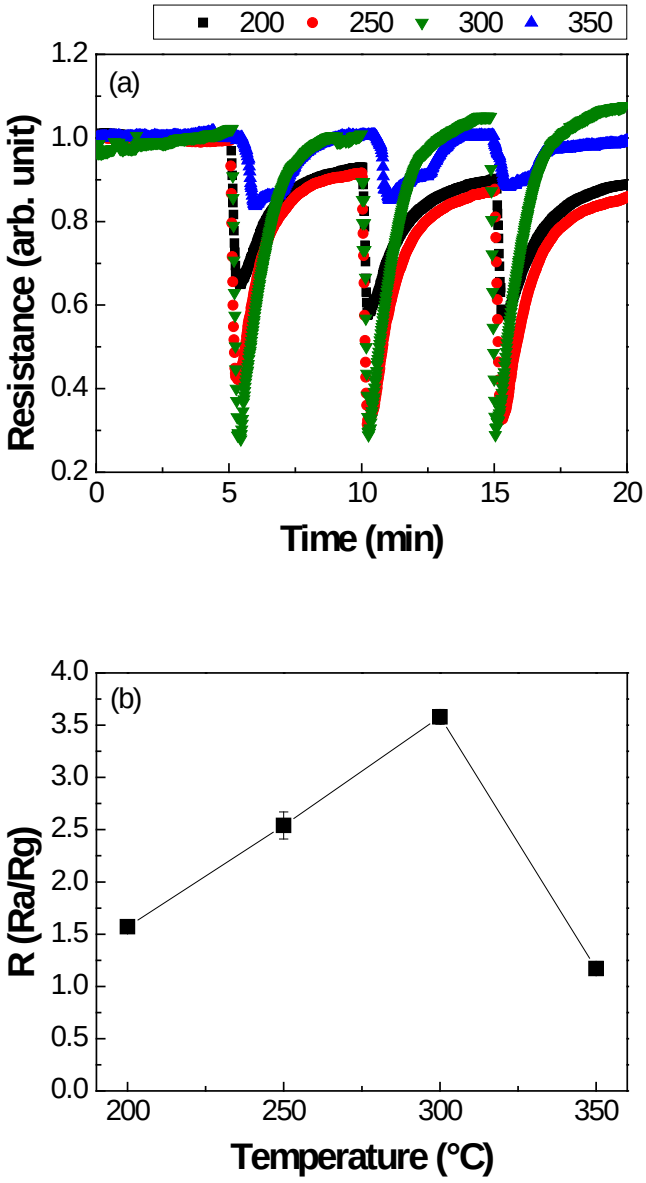

Figure 51. (a) Resistance change profile of ZnO hollow microsphere films against ethanol with increasing temperature and (b) comparison of gas response rate at different temperatures.

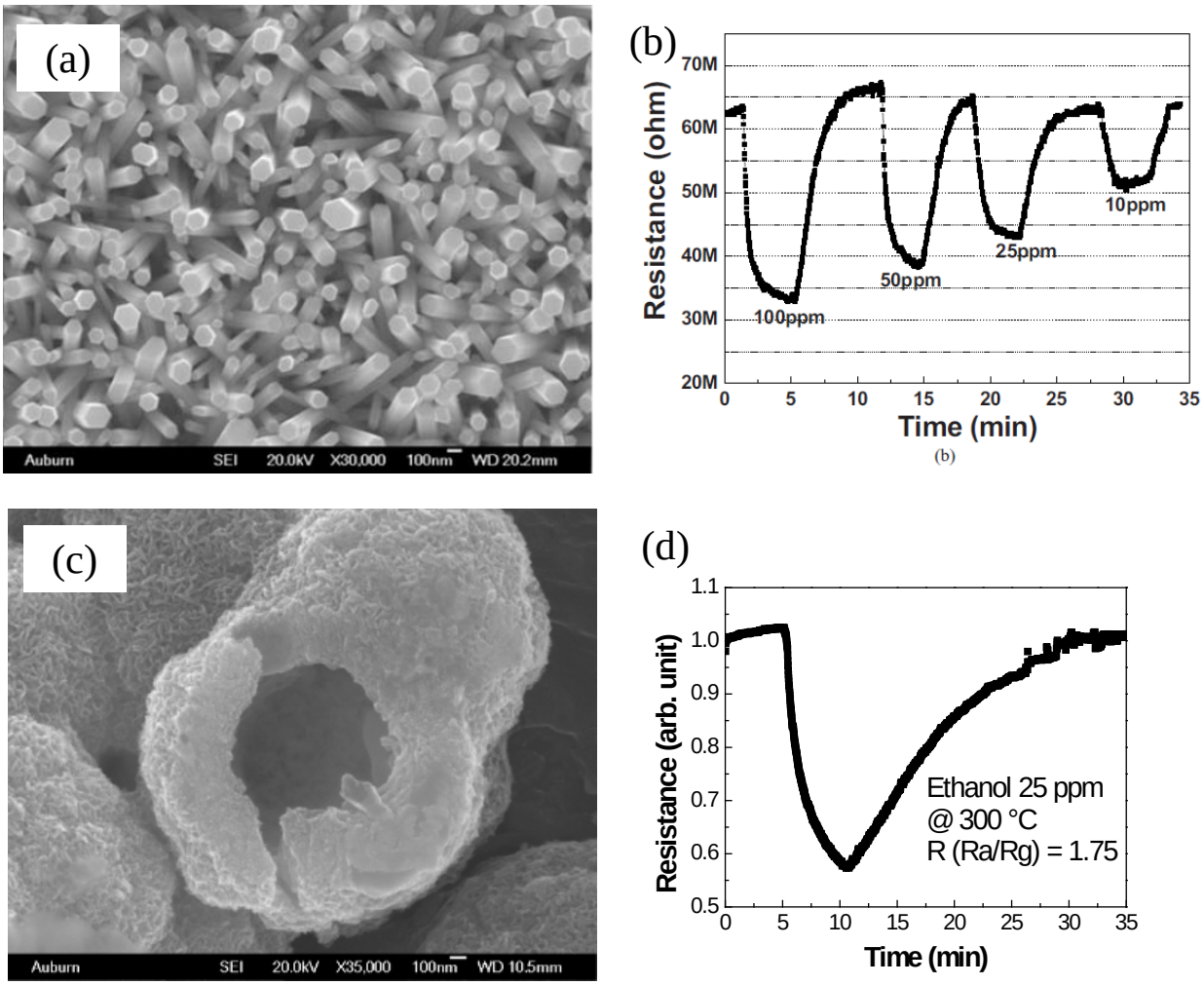

Figure 52. (a) SEM image of ZnO nanorods [1], (b) Resistance change profile of ZnO nanorods against different concentration of ethanol at 300℃ [1], (c) SEM image of ZnO hollow microspheres, and (d) Resistance change profile of ZnO hollow microspheres against 25 ppm of ethanol at 300℃.

As shown in Figure 52, the R ratio of hollow microspheres was compared to that of nanorods. The R of ZnO hollow microsphere films against 25 ppm of ethanol at 300 °C was 1.75, as shown in Figure 52 (d). In the previous study from this group, the R of ZnO nanorods at the same

condition was less than 1.5, as shown in Figure 52 (b) [1]. This difference can be explained by the porous structure and larger surface-to-volume ratio of ZnO hollow microspheres.

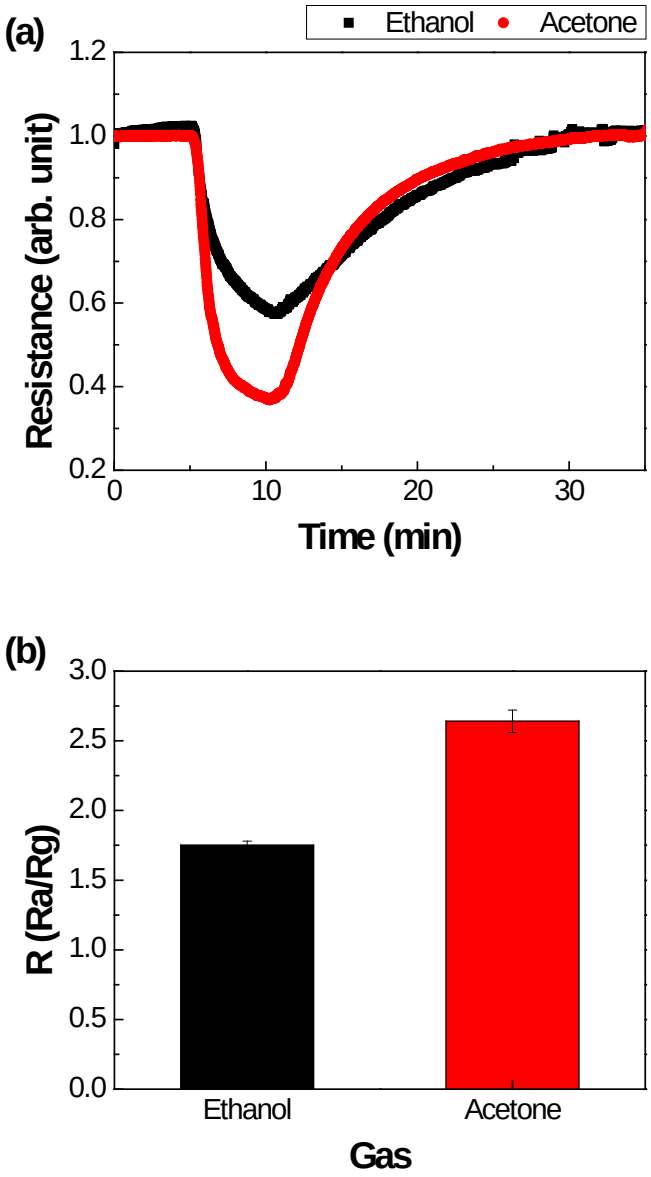

Figure 53. (a) Resistance change profile of ZnO hollow microsphere films against ethanol and acetone and (b) comparison of gas response rate with different gases.

Figure 53 shows the resistance change of ZnO films against 25 ppm of ethanol and acetone gases at 300 °C. ZnO hollow microspheres show good response with ethanol and acetone gases as well as a higher response rate than other structures.

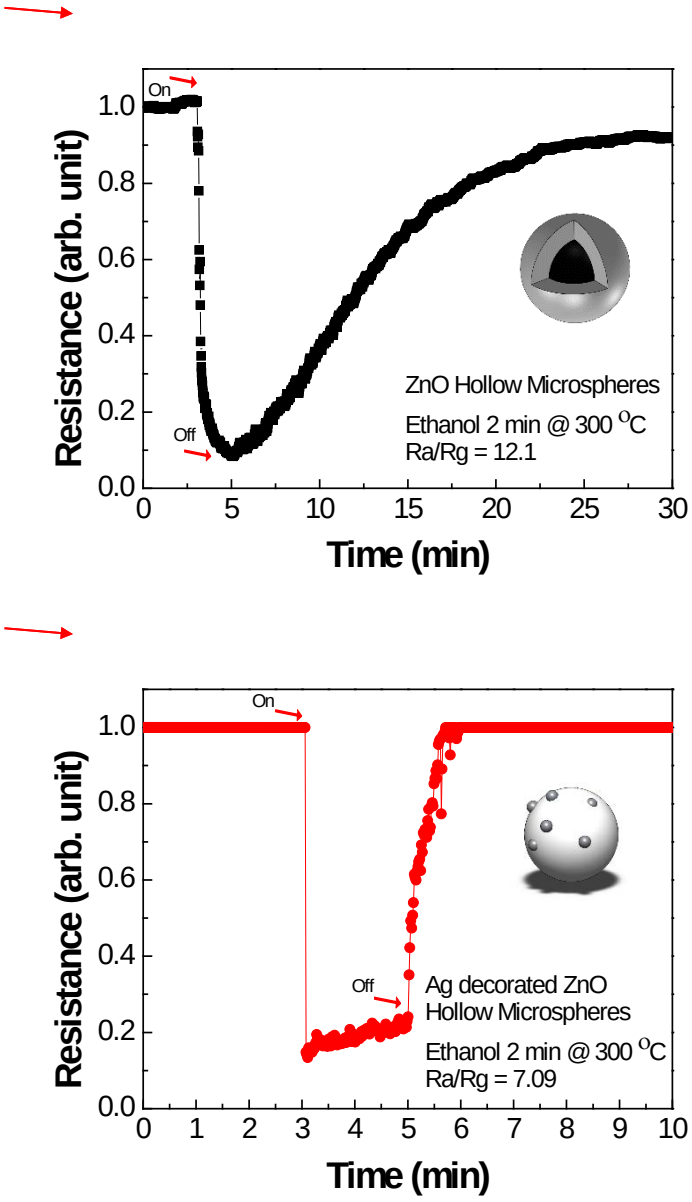

Figure 54. Resistance change profile of (a) ZnO hollow microspheres against ethanol and (b) Ag decorated ZnO hollow microspheres.

The effect of silver catalyst was studied as shown in Figure 54. In Figure 54 (a), ZnO hollow microspheres showed good response with ethanol. But as shown in Figure 54 (b), decorating Ag on the surface of ZnO hollow microspheres resulted in a rapid response rate and significantly reduced recovery time. The improvement of the ZnO hollow microspheres' sensitivity upon Ag addition can be explained as a "chemical" process [44]. This process is related to the effective dissociation catalytic ability of Ag. Ag can dissociate more oxygen than ZnO, so more absorbed oxygen species, O^{2-} and O^{-}, can react with ethanol gas than with the pristine ZnO. Also, the active surface area can be increased by the decoration of Ag.

7.3.2 Different morphologies of NiO and their gas sensing properties

In order to further investigate the morphological influence on properties, ethanol gas sensing characteristics of NiO films coated by EPD were investigated by measuring resistance change. Figure 55 shows the resistance change of NiO films against 100 ppm of ethanol with increasing temperature, 200-400 °C. NiO is a p-type semiconductor. As shown in Figure 55 (a), the resistance increased when the NiO films were exposed to ethanol gas through the elimination of the adsorbed oxygen species. The films' gas response rates were determined as the ratio of the resistance measured in detecting gas (R_g) to that measured in air (R_a). As shown in Figure 55, better gas response was obtained at 300 °C. The values of gas response rate in this work are comparable with previously reported values [96, 124, 135]. A competition exists between slow kinetics at low temperatures and enhanced desorption at high temperatures. Metal oxide gas sensors show a maximum gas response at certain operating temperatures; the maximum gas response of ethanol is obtained around 300 °C [131-135]. The ethanol detecting reaction on the surface of NiO [129] is shown as follows:

$$C_2H_5OH_{ads} + O^-_{ads} \leftrightarrow H_2O + CO_2 + e^-, \quad \text{(Equation 14)}$$

$$C_2H_5OH_{ads} + O^{2-}_{ads} \leftrightarrow H_2O + CO_2 + 2e^-, \quad \text{(Equation 15)}$$

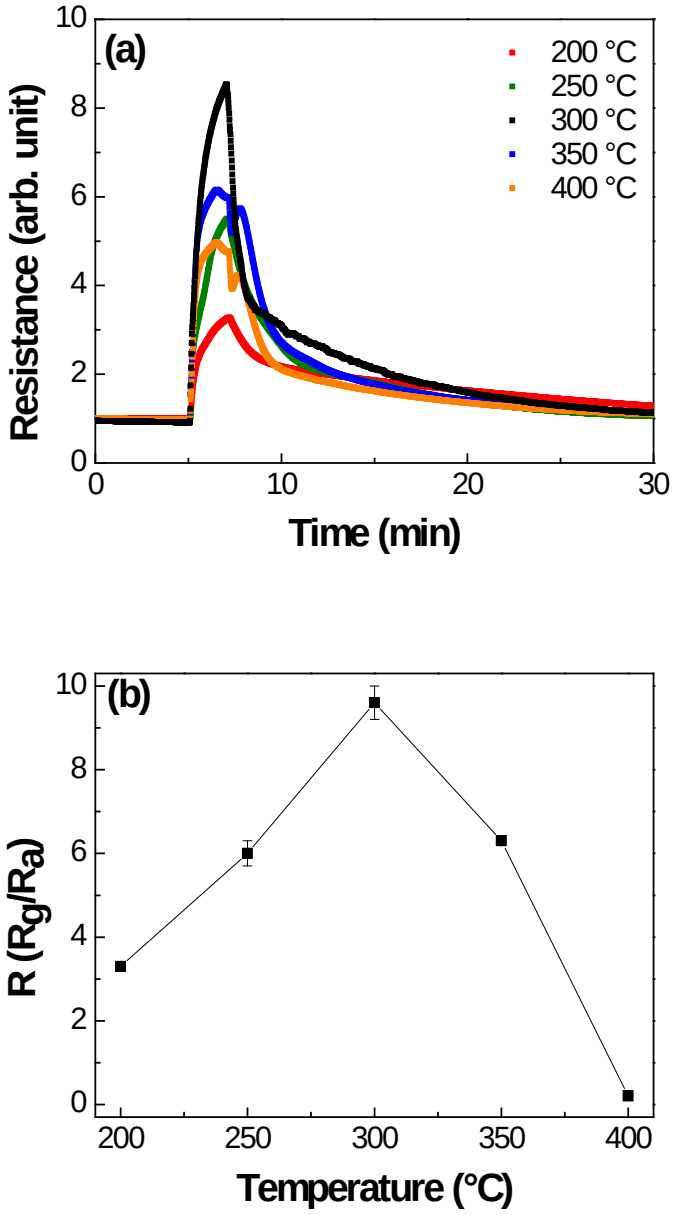

Figure 55. (a) Resistance change profile and (b) ratio of resistance of NiO.

During reaction, ethanol gas consumes adsorbed oxygen species, O^{2-} and O^{-}, on the NiO surface. At higher operating temperatures, the interaction between NiO and ethanol forms more oxygen species and obtains enough energy to overcome the activation energy. However, due to the difficulty of exothermic ethanol gas adsorption, the rate of response is degraded above 300 °C. Therefore, 300 °C is the optimum operating temperature.

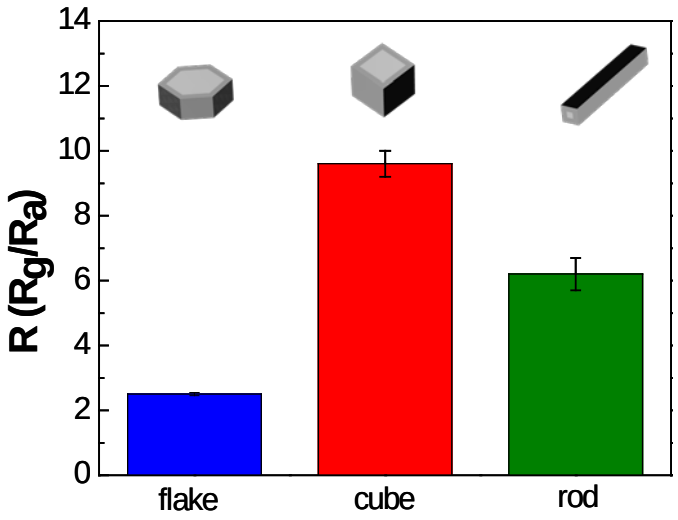

Figure 56. Ratio of resistance of different morphologies of NiO.

Figure 56 shows the resistance change of NiO films with different morphologies of samples against 100 ppm of ethanol gas. As shown in Figure 56, the highest gas response was obtained with cube-like NiO particles synthesized without TEA. Since the gas sensing sensitivity is largely related to the surface reactions, the surface area to volume ratios of the sensing materials is an important factor. The gas sensing sensitivity results shown in Figure 56 corresponded to the

BET surface area because of the larger surface area of a smaller particle size and uniformly coated layer without aggregation of particles.

7.4 Summary and conclusions

ZnO hollow microspheres were prepared using a precipitation method. After calcination at 500 °C for 1 hour, the as-precipitated particles were transformed from amorphous zinc citrate to crystalline zinc oxide. In addition, to study the effect of silver as a catalyst, silver particles were decorated on the surface of ZnO hollow microspheres by dispersing in silver nitrate solution. ZnO hollow microsphere films fabricated by electrophoretic deposition were utilized for a gas sensor. When ethanol and acetone, the target gases, were measured in synthetic air by ZnO sensors at different temperatures, the highest sensing response was observed at 300 °C. The improved sensing behavior of ZnO hollow microsphere may be due primarily to its large surface-to volume ratio. The response and recovery time was significantly reduced by silver decoration on ZnO hollow microspheres.

Different morphologies of NiO were prepared using by a hydrothermal method. After calcination at 300 °C for 1 hour, as-precipitated particles were transformed from nickel oxalate to the pure nickel oxide phase. NiO films fabricated by electrophoretic deposition were utilized for ethanol gas sensors. 100 ppm of ethanol gas in synthetic air was measured by NiO sensors at different temperatures. The best gas response was obtained at 300 °C. NiO particles synthesized without TEA showed a higher gas response due to the high surface area.

Chapter 8. Conclusion and future work

8.1 Conclusion

Prior to AC-EPD of aqueous suspensions, the dominant parameters, zeta potential and electric field, of DC-EPD have been studied with ZnO nanoparticles suspended in ethanol to understand and develop the kinetics of AC-EPD. Smaller particle size promoted zeta potential of particles, which is directly proportional to particle mobility. Thus, higher deposition rates were achieved with smaller particles. Also, the deposition weight showed a linear relationship with the electric field, which is a driving force of particle movement. Thus, an increased electric field controlled by applied voltage resulted in a higher deposition rate. The dried morphology of the ZnO nanoparticle layers showed more uniform packing at smaller size and lower applied voltage.

A cost-effective and clean EPD process was achieved by adding water. When ZnO nanoparticles suspended in a mixture of ethanol and water systems were used, the EPD result showed a maximum as a function of added water amount. The charging agent effect of H^+ ion by water electrolysis competes with the decrease of particle movement due to high conductivity of the suspension. Water as an additive had comparable deposition kinetics to a polymer additive.

To achieve an environmentally benign aqueous EPD system, this research developed approaches for an aqueous EPD process conducted with AC electric fields, which can reduce the gas bubbles formed by the decomposition of water. The effect of frequency, which is a key parameter, on the kinetics of AC-EPD was compared with ZnO in aqueous suspensions and ethanol suspensions. AC-EPD with an aqueous system showed the maximum deposition yield because the reduced wave

cycles at low frequency caused electrolysis of water and too rapid vibration of particles at high frequency caused insufficient deposition time. However, for ethanol systems, low frequency had no significant effect on the deposition yield.

EPD was performed to deposit ZnO nanoparticles on conductive fabrics and plates from a ZnO-ethanol suspension system. Deposition behavior of ZnO nanoparticles was examined by varying applied voltage and compared using a kinetic equation. The deposition rate increased as particle size decreased due to an enhanced zeta potential. Although the deposition weight showed a linear relationship with applied voltage, the rough surface or larger surface area of woven fabric yielded higher weight gain than did a flat plate substrate.

The dried morphology of ZnO nanoparticle layers showed uniform at lower applied voltage, but higher voltage corresponding to faster deposition rate caused cracks on the surface during drying. ZnO layers without preferred orientation were confirmed by XRD. Such variation in the particle packing density influenced the dielectric properties. Smaller particle size gave a denser structure in the deposited ZnO layer, and the denser structure also enhanced the dielectric constant.

An UV-Vis DRS showed good UV blocking properties and energy bandgap comparable to previously reported values. PL and Raman spectra also showed similar results with bulk ZnO. Although the values in PL, UV, and Raman spectra were slightly shifted compared with bulk ZnO, this difference can be attributed to smaller particle size and defects in the as-deposited ZnO layer.

EPD can be an effective method for uniform deposition of ZnO nanoparticles onto fabrics at lower temperatures. This EPD method will be useful for developing multifunctional devices on flexible substrates.

Synthesis of ZnO and NiO was studied with controlling isotropy and porosity to apply the in-situ EPD process. Hierarchically structured ZnO was synthesized by a simple precipitation with the addition of sodium citrate. A simple hydrothermal method was successfully implemented to synthesize NiO with tailored morphology using TEA.

When citrate ion was added to a solution for a precipitation method, isotropic porous and hollow microsphere ZnO was fabricated. After calcination at 500 °C for 1 hour, as-precipitated particles were transformed from amorphous zinc citrate to polycrystalline ZnO phase. The citrate ions participated in the reaction and formed porous and hollow microspheres with a significantly large surface area. In addition, to study the effect of silver as a catalyst, silver particles were decorated on the surface of ZnO hollow microspheres by dispersing in silver nitrate solution.

When TEA was added to a solution for a hydrothermal method, highly anisotropic needle-like NiO particles were grown. After calcination at 300 °C for 1 hour, as-synthesized precipitates were transformed from NiC_2O_4 to the pure NiO phase. The presence of TEA may promote the formation of NiC_2O_4 with a higher aspect ratio. In addition, to study the effect of morphology, flake-like NiO was prepared by a precipitation method.

ZnO hollow microsphere films fabricated by electrophoretic deposition were utilized for a gas sensor. When ethanol and acetone, the target gases, were measured in synthetic air by ZnO sensors at different temperatures, the highest sensing response was observed at 300 °C. The improved sensing behavior of ZnO hollow microspheres may be due primarily to large surface-to volume ratio. The response and recovery time was significantly reduced by silver decoration on ZnO hollow microspheres.

Different morphologies of NiO films fabricated by electrophoretic deposition were utilized for ethanol gas sensors. Ethanol gas in synthetic air was measured by NiO sensors at different

temperatures, and better gas response was obtained at 300 °C. The highest gas response was obtained with cube-like NiO particles synthesized without TEA due to their high surface area.

8.2 Future work

Thus far, hierarchically structured ZnO and NiO have been researched by using a simple synthesis method. The specific surface area of hierarchical nanostructure should be applied to VOCs sensor devices because of the improved sensitivity. However, in-situ EPD should be further studied with the goal of simplifying the process and better controlling the deposited layers. Also, even though the sensitivity was improved, metal oxide gas sensors designed for daily use need lower operating temperatures and lower detectable gas concentration. Thus, more studies will be required to power the operation temperature and diluted concentration of target gases. Moreover, it would be interesting to study gas sensors with nanostructured p-n junction devices because such devices would have merits in both surface to volume ratio and energy barrier for the gas reactions.

Bibliography

1. Ahn, H., et al., *Vertically aligned zno nanorod sensor on flexible substrate for ethanol gas monitoring.* Electrochemical and Solid-State Letters, 2010. **13**(11): p. J125-J128.
2. Corni, I., M.P. Ryan, and A.R. Boccaccini, *Electrophoretic deposition: From traditional ceramics to nanotechnology.* Journal of the European Ceramic Society, 2008. **28**(7): p. 1353-1367.
3. Wang, Y.C., I.C. Leu, and M.H. Hon, *Kinetics of electrophoretic deposition for nanocrystalline zinc oxide coatings.* Journal of the American Ceramic Society, 2004. **87**(1): p. 84-88.
4. Besra, L., C. Compson, and M. Liu, *Electrophoretic Deposition of YSZ Particles on Non-Conducting Porous NiO–YSZ Substrates for Solid Oxide Fuel Cell Applications.* Journal of the American Ceramic Society, 2006. **89**(10): p. 3003-3009.
5. Besra, L. and M. Liu, *A review on fundamentals and applications of electrophoretic deposition (EPD).* Progress in materials science, 2007. **52**(1): p. 1-61.
6. Boccaccini, A.R., et al., *Electrophoretic deposition of carbon nanotubes.* Carbon, 2006. **44**(15): p. 3149-3160.
7. Park, S. and S. Jayaraman, *Smart textiles: Wearable electronic systems.* MRS bulletin, 2003. **28**(08): p. 585-591.
8. Bae, J., et al., *Fiber Supercapacitors Made of Nanowire-Fiber Hybrid Structures for Wearable/Flexible Energy Storage.* Angewandte Chemie International Edition, 2011. **50**(7): p. 1683-1687.

9. Park, H., et al., *Growth of nanostructured ZnO on wearable fabrics for functional garment.* Materials Letters, 2014. **118**: p. 47-50.

10. Ahn, H., et al., *Effect of annealing and argon-to-oxygen ratio on sputtered SnO 2 thin film sensor for ethylene gas detection.* Materials Chemistry and Physics, 2010. **124**(1): p. 563-568.

11. Dirksen, J.A., K. Duval, and T.A. Ring, *NiO thin-film formaldehyde gas sensor.* Sensors and Actuators B: Chemical, 2001. **80**(2): p. 106-115.

12. Hübner, M., et al., *Influence of humidity on CO sensing with p-type CuO thick film gas sensors.* Sensors and Actuators B: Chemical, 2011. **153**(2): p. 347-353.

13. Miao, B., et al., *Characterization and gas-sensing properties of NiO nanowires prepared through hydrothermal method.* Physica E: Low-dimensional Systems and Nanostructures, 2013. **52**: p. 40-45.

14. Rout, C.S., et al., *Hydrogen and ethanol sensors based on ZnO nanorods, nanowires and nanotubes.* Chemical Physics Letters, 2006. **418**(4): p. 586-590.

15. Varghese, O., et al., *Gas sensing characteristics of multi-wall carbon nanotubes.* Sensors and Actuators B: Chemical, 2001. **81**(1): p. 32-41.

16. Guo, W., et al., *Gas-sensing property improvement of ZnO by hierarchical flower-like architectures.* Materials Letters, 2011. **65**(23): p. 3384-3387.

17. Kim, H.-J., et al., *Ultraselective and sensitive detection of xylene and toluene for monitoring indoor air pollution using Cr-doped NiO hierarchical nanostructures.* Nanoscale, 2013. **5**(15): p. 7066-7073.

18. Kuang, D.-B., et al., *Fabrication of novel hierarchical β-Ni (OH) 2 and NiO microspheres via an easy hydrothermal process.* The Journal of Physical Chemistry C, 2009. **113**(14): p. 5508-5513.

19. Ouedraogo, B. and O. Savadogo, *Electrophoretic Deposition of Alumina and Nickel Oxide Particles.* Journal of Scientific Research and Reports, 2013. **2**(1): p. 190-205.

20. Hamaker, H., *Formation of a deposit by electrophoresis.* Transactions of the Faraday Society, 1940. **35**: p. 279-287.

21. Zhang, Z., Y. Huang, and Z. Jiang, *Electrophoretic Deposition Forming of SiC-TZP Composites in a Nonaqueous Sol Media.* Journal of the American Ceramic Society, 1994. **77**(7): p. 1946-1949.

22. Ammam, M., *Electrophoretic deposition under modulated electric fields: a review.* RSC Advances, 2012. **2**(20): p. 7633-7646.

23. Chávez-Valdez, A. and A.R. Boccaccini, *Innovations in electrophoretic deposition: Alternating current and pulsed direct current methods.* Electrochimica Acta, 2012. **65**: p. 70-89.

24. Koura, N., et al., *Preparation of various oxide films by an electrophoretic deposition method: a study of the mechanism.* Japanese Journal of Applied Physics, 1995. **34**(3R): p. 1643.

25. Uchikoshi, T., et al., *Dense, bubble-free ceramic deposits from aqueous suspensions by electrophoretic deposition.* Journal of Materials Research, 2001. **16**(02): p. 321-324.

26. Tang, F., T. Uchikoshi, and Y. Sakka, *Electrophoretic deposition behavior of aqueous nanosized zinc oxide suspensions.* Journal of the American Ceramic Society, 2002. **85**(9): p. 2161-2165.

27. Verde, M., et al., *Electrophoretic Deposition of Transparent ZnO Thin Films from Highly Stabilized Colloidal Suspensions.* Journal of colloid and interface science, 2012. **373**(1): p. 27-33.

28. Lima, M.D., et al., *Thin, conductive, carbon nanotube networks over transparent substrates by electrophoretic deposition.* Journal of Materials Chemistry, 2008. **18**(7): p. 776-779.

29. Zhang, J., et al., *Functional interphases with multi-walled carbon nanotubes in glass fibre/epoxy composites.* Carbon, 2010. **48**(8): p. 2273-2281.

30. Hasan, S.A., et al., *Electrophoretic deposition of CdSe nanocrystal films onto dielectric polymer thin films.* Thin Solid Films, 2009. **517**(8): p. 2665-2669.

31. Heidari, E.K., et al., *WO< sub> 3</sub>-based NO< sub> 2</sub> sensors fabricated through low frequency AC electrophoretic deposition.* Sensors and Actuators B: Chemical, 2010. **146**(1): p. 165-170.

32. Riahifar, R., et al., *A new technique for micro-patterning of nanoparticles on non-conductive substrate by low frequency AC electrophoresis.* Journal of Materials Science: Materials in Electronics, 2011. **22**(9): p. 1218-1221.

33. Cimitan, S., et al., *Solvothermal synthesis and properties control of doped ZnO nanoparticles.* Journal of Colloid and Interface Science, 2009. **329**(1): p. 73-80.

34. Singh, O., N. Kohli, and R.C. Singh, *Precursor controlled morphology of zinc oxide and its sensing behaviour.* Sensors and Actuators B: Chemical, 2013. **178**: p. 149-154.

35. Zheng, M., et al., *Fabrication and optical properties of large-scale uniform zinc oxide nanowire arrays by one-step electrochemical deposition technique.* Chemical Physics Letters, 2002. **363**(1): p. 123-128.

36. Choi, K.-S., et al., *Electrochemical synthesis of nanostructured ZnO films utilizing self-assembly of surfactant molecules at solid-liquid interfaces.* Journal of the American Chemical Society, 2002. **124**(42): p. 12402-12403.

37. Lyu, S.C., et al., *Low-temperature growth of ZnO nanowire array by a simple physical vapor-deposition method.* Chemistry of Materials, 2003. **15**(17): p. 3294-3299.

38. Yoshino, Y., et al., *Optimization of zinc oxide thin film for surface acoustic wave filters by radio frequency sputtering.* Vacuum, 2000. **59**(2): p. 538-545.

39. Cho, S., S.-H. Jung, and K.-H. Lee, *Morphology-controlled growth of ZnO nanostructures using microwave irradiation: from basic to complex structures.* The Journal of Physical Chemistry C, 2008. **112**(33): p. 12769-12776.

40. Zhang, Q., et al., *Diagnosis of diabetes by image detection of breath using gas-sensitive laps.* Biosensors and Bioelectronics, 2000. **15**(5): p. 249-256.

41. Moorhead, K.T., et al., *Classifying algorithms for SIFT-MS technology and medical diagnosis.* Computer methods and programs in biomedicine, 2008. **89**(3): p. 226-238.

42. de Lacy Costello, B., et al., *The characteristics of novel low-cost sensors for volatile biomarker detection.* Journal of breath research, 2008. **2**(3): p. 037017.

43. Kim, H.-J. and J.-H. Lee, *Highly sensitive and selective gas sensors using p-type oxide semiconductors: overview.* Sensors and Actuators B: Chemical, 2014. **192**: p. 607-627.

44. Wang, C., et al., *Metal oxide gas sensors: sensitivity and influencing factors.* Sensors, 2010. **10**(3): p. 2088-2106.

45. Meher, S.K., P. Justin, and G. Ranga Rao, *Microwave-mediated synthesis for improved morphology and pseudocapacitance performance of nickel oxide.* ACS Applied Materials & Interfaces, 2011. **3**(6): p. 2063-2073.

46. Huang, J., et al., *Fabrication and gas-sensing properties of hierarchically porous ZnO architectures.* Sensors and Actuators B: Chemical, 2011. **155**(1): p. 126-133.

47. Kim, H.-R., et al., *Ultra-fast responding and recovering C 2 H 5 OH sensors using SnO 2 hollow spheres prepared and activated by Ni templates.* Chemical Communications, 2010. **46**(28): p. 5061-5063.

48. Fukada, Y., et al., *Electrophoretic deposition—mechanisms, myths and materials.* Journal of Materials Science, 2004. **39**(3): p. 787-801.

49. Hamaker, H. and E. Verwey, *Part II.—(C) Colloid stability. The role of the forces between the particles in electrodeposition and other phenomena.* Transactions of the Faraday Society, 1940. **35**: p. 180-185.

50. Grillon, F., D. Fayeulle, and M. Jeandin, *Quantitative image analysis of electrophoretic coatings.* Journal of Materials Science Letters, 1992. **11**(5): p. 272-275.

51. Sarkar, P. and P.S. Nicholson, *Electrophoretic deposition (EPD): mechanisms, kinetics, and application to ceramics.* Journal of the American Ceramic Society, 1996. **79**(8): p. 1987-2002.

52. Ma, J. and W. Cheng, *Electrophoretic deposition of lead zirconate titanate ceramics.* Journal of the American Ceramic Society, 2002. **85**(7): p. 1735-1737.

53. Tabellion, J. and R. Clasen, *Electrophoretic deposition from aqueous suspensions for near-shape manufacturing of advanced ceramics and glasses—applications.* Journal of Materials Science, 2004. **39**(3): p. 803-811.

54. von, B.H. and J. Hausselt, *Ceramic microstructures by electrophoretic deposition of colloidal suspensions*, 2002, ELECTROCHEMICAL SOCIETY INC. p. 78-85.

55. Sakurada, O., et al., *Bubble-free electrophoretic deposition of aqueous zirconia suspensions with hydroquinone.* Journal of Materials Science, 2004. **39**(5): p. 1845-1847.

56. Besra, L., et al., *Experimental verification of pH localization mechanism of particle consolidation at the electrode/solution interface and its application to pulsed DC electrophoretic deposition (EPD).* Journal of the European Ceramic Society, 2010. **30**(5): p. 1187-1193.

57. Naim, M.N., et al., *Electrical-driven disaggregation of the two-dimensional assembly of colloidal polymer particles under pulse DC charging.* Advanced Powder Technology, 2010. **21**(5): p. 534-541.

58. Nold, A. and R. Clasen, *Bubble-free electrophoretic shaping from aqueous suspension with micro point-electrode.* Journal of the European Ceramic Society, 2010. **30**(14): p. 2971-2975.

59. Neirinck, B., et al., *Aqueous electrophoretic deposition in asymmetric AC electric fields (AC–EPD).* Electrochemistry Communications, 2009. **11**(1): p. 57-60.

60. Yue, C.-F.J., D. Kumar, and R.K. Singh, *Fabrication of Ag-sheathed Bi–Sr–Ca–Cu–O thick films by a novel ac-electric field assisted electrophoretic deposition method.* Physica C: Superconductivity, 1999. **314**(3): p. 291-298.

61. Raissi, B., E. Marzbanrad, and A. Gardeshzadeh, *Particle size separation by alternating electrophoretic deposition.* Journal of the European Ceramic Society, 2009. **29**(15): p. 3289-3291.

62. Vetter, K.J., *Electrochemical kinetics; theoretical and experimental aspects*1967, New York, United States: Academic Press.

63. Oddy, M. and J. Santiago, *A method for determining electrophoretic and electroosmotic mobilities using AC and DC electric field particle displacements.* Journal of Colloid and Interface Science, 2004. **269**(1): p. 192-204.

64. Yoshioka, T., et al., *AC electrophoretic deposition of organic–inorganic composite coatings.* Journal of Colloid and Interface Science, 2013. **392**: p. 167-171.

65. Raju, K. and D.H. Yoon, *Electrophoretic deposition of BaTiO3 in an aqueous suspension using asymmetric alternating current.* Materials Letters, 2013. **110**(0): p. 188-190.

66. Raju, K., H.-W. Yu, and D.-H. Yoon, *Aqueous electrophoretic deposition of SiC using asymmetric AC electric fields.* Ceramics International, 2014.

67. Gardeshzadeh, A.R., et al., *Fabrication of resistive CO gas sensor based on SnO2 nanopowders via low frequency AC electrophoretic deposition.* Journal of Materials Science: Materials in Electronics, 2009. **20**(2): p. 127-131.

68. Riahifar, R., et al., *Sorting ZnO particles of different shapes with low frequency AC electric fields.* Materials Letters, 2011. **65**(4): p. 632-635.

69. Wei, C., et al., *The separation of different conducting multi-walled carbon nanotubes by AC dielectrophoresis.* Diamond and Related Materials, 2009. **18**(2): p. 332-336.

70. Ozhukil Kollath, V., et al., *AC vs. DC electrophoretic deposition of hydroxyapatite on titanium.* Journal of the European Ceramic Society, 2013. **33**(13): p. 2715-2721.

71. Djurišić, A.B. and Y.H. Leung, *Optical properties of ZnO nanostructures.* Small, 2006. **2**(8-9): p. 944-961.

72. Meulenkamp, E.A., *Synthesis and growth of ZnO nanoparticles.* The Journal of Physical Chemistry B, 1998. **102**(29): p. 5566-5572.

73. Wang, H., et al., *Growth mechanism of different morphologies of ZnO crystals prepared by hydrothermal method.* Journal of Materials Science & Technology, 2011. **27**(2): p. 153-158.

74. Tian, Z.R., et al., *Complex and oriented ZnO nanostructures.* Nature materials, 2003. **2**(12): p. 821-826.

75. Liang, J., et al., *Hydrothermal growth and optical properties of doughnut-shaped ZnO microparticles.* The Journal of Physical Chemistry B, 2005. **109**(19): p. 9463-9467.

76. Cho, S., et al., *Formation of amorphous zinc citrate spheres and their conversion to crystalline ZnO nanostructures.* Langmuir, 2010. **27**(1): p. 371-378.

77. Zhang, H., et al., *Controllable growth of ZnO microcrystals by a capping-molecule-assisted hydrothermal process.* Crystal growth & design, 2005. **5**(2): p. 547-550.

78. Liang, J., et al., *Malate-assisted synthesis of ZnO hexagonal architectures with porous characteristics and photoluminescence properties investigation.* The Journal of Physical Chemistry C, 2007. **111**(3): p. 1113-1118.

79. Li, F., et al., *Single-Crystal Hexagonal Disks and Rings of ZnO: Low-Temperature, Large-Scale Synthesis and Growth Mechanism.* Angewandte Chemie International Edition, 2004. **43**(39): p. 5238-5242.

80. Peng, Y., et al., *Polymer-controlled crystallization of zinc oxide hexagonal nanorings and disks.* The Journal of Physical Chemistry B, 2006. **110**(7): p. 2988-2993.

81. Kim, C., et al., *Whispering-gallery-modelike-enhanced emission from ZnO nanodisk.* 2006.

82. Li, G.-J., et al., *Preparation and characteristics of nanocrystalline NiO by organic solvent method.* Materials Letters, 2001. **51**(4): p. 325-330.

83. Wu, M.-S. and H.-H. Hsieh, *Nickel oxide/hydroxide nanoplatelets synthesized by chemical precipitation for electrochemical capacitors.* Electrochimica Acta, 2008. **53**(8): p. 3427-3435.

84. Xiang, L., X. Deng, and Y. Jin, *Experimental study on synthesis of NiO nano-particles.* Scripta Materialia, 2002. **47**(4): p. 219-224.

85. Deng, X. and Z. Chen, *Preparation of nano-NiO by ammonia precipitation and reaction in solution and competitive balance.* Materials Letters, 2004. **58**(3): p. 276-280.

86. Wu, L., et al., *Synthesis and characteristics of NiO nanowire by a solution method.* Materials Letters, 2004. **58**(21): p. 2700-2703.

87. Zhou, G.-T., et al., *Preparation and characterization of nanoplatelets of nickel hydroxide and nickel oxide.* Materials Chemistry and Physics, 2006. **98**(2): p. 267-272.

88. Spinner, N. and W.E. Mustain, *Effect of nickel oxide synthesis conditions on its physical properties and electrocatalytic oxidation of methanol.* Electrochimica Acta, 2011. **56**(16): p. 5656-5666.

89. Choopun, S., E. Wongrat, and N. Hongsith, *Metal-oxide nanowires for gas sensors*2012: INTECH Open Access Publisher.

90. Xie, Q., et al., *Template-free synthesis of zinc citrate yolk–shell microspheres and their transformation to ZnO yolk–shell nanospheres.* Journal of Materials Chemistry, 2012. **22**(27): p. 13541-13547.

91. Wang, D., et al., *Template-free synthesis and gas sensing properties of hierarchical hollow ZnO microspheres.* CrystEngComm, 2013. **15**(37): p. 7438-7442.

92. Lee, J.-H., *Gas sensors using hierarchical and hollow oxide nanostructures: overview.* Sensors and Actuators B: Chemical, 2009. **140**(1): p. 319-336.

93. Li, X., et al., *Template-free microwave-assisted synthesis of ZnO hollow microspheres and their application in gas sensing.* CrystEngComm, 2013. **15**(15): p. 2949-2955.

94. Rao, J., et al., *Construction of hollow and mesoporous ZnO microsphere: a facile synthesis and sensing property.* ACS Applied Materials & Interfaces, 2012. **4**(10): p. 5346-5352.

95. Liu, B., et al., *Synthesis and enhanced gas-sensing properties of ultralong NiO nanowires assembled with NiO nanocrystals.* Sensors and Actuators B: Chemical, 2011. **156**(1): p. 251-262.

96. Lin, L., et al., *Synthesis of NiO nanostructures from 1D to 3D and researches of their gas-sensing properties.* Materials Research Bulletin, 2013. **48**(2): p. 449-454.

97. Kim, K.-M., et al., *Selective detection of NO2 using Cr-doped CuO nanorods.* Sensors, 2012. **12**(6): p. 8013-8025.

98. Na, C.W., H.-S. Woo, and J.-H. Lee, *Design of highly sensitive volatile organic compound sensors by controlling NiO loading on ZnO nanowire networks.* RSC Advances, 2012. **2**(2): p. 414-417.

99. Chen, A. and P. Holt-Hindle, *Platinum-based nanostructured materials: synthesis, properties, and applications.* Chem. Rev, 2010. **110**(6): p. 3767-3804.

100. Chung, Y., et al., *Electrophoretic deposition behavior of ZnO nanoparticles and their properties on conductive fabrics.* Journal of Ceramic Processing Research, 2014. **15**(5): p. 331-335.

101. Chung, Y., et al., *Growth and dielectric properties of ZnO nanoparticles deposited by using electrophoretic deposition.* Journal of the Korean Physical Society, 2015. **66**(9): p. 1359-1363.

102. Talebi, T., B. Raissi, and A. Maghsoudipour, *The role of addition of water to non-aqueous suspensions in electrophoretically deposited YSZ films for SOFCs.* International Journal of Hydrogen Energy, 2010. **35**(17): p. 9434-9439.

103. Gardeshzadeh, A.R., B. Raissi, and E. Marzbanrad, *Preparation of Si powder thick films by low frequency alternating electrophoretic deposition.* Journal of Materials Science, 2008. **43**(7): p. 2507-2508.

104. Chávez-Valdez, A., M. Herrmann, and A. Boccaccini, *Alternating current electrophoretic deposition (EPD) of TiO< sub> 2</sub> nanoparticles in aqueous suspensions.* Journal of Colloid and Interface Science, 2012. **375**(1): p. 102-105.

105. Boccaccini, A.R. and I. Zhitomirsky, *Application of electrophoretic and electrolytic deposition techniques in ceramics processing.* Current Opinion in Solid State and Materials Science, 2002. **6**(3): p. 251-260.

106. Farnoush, H., J.A. Mohandesi, and D.H. Fatmehsari, *Effect of Particle Size on the Electrophoretic Deposition of Hydroxyapatite Coatings: A Kinetic Study Based on a Statistical Analysis.* International Journal of Applied Ceramic Technology, 2013. **10**(1): p. 87-96.

107. Boccaccini, A.R. and P.A. Trusty, *Electrophoretic deposition infiltration of metallic fabrics with a boehmite sol for the preparation of ductile-phase-toughened ceramic composites.* Journal of materials science, 1998. **33**(4): p. 933-938.

108. Vorob'eva, M., et al., *Preparation of catalyst carriers on the basis of alumina supported on metallic gauzes.* Applied Catalysis A: General, 2000. **199**(2): p. 257-261.

109. Yang, R.D., et al., *Photoluminescence and micro-Raman scattering in ZnO nanoparticles: The influence of acetate adsorption.* Chemical physics letters, 2005. **411**(1): p. 150-154.

110. Kamalasanan, M. and S. Chandra, *Sol-gel synthesis of ZnO thin films.* Thin Solid Films, 1996. **288**(1): p. 112-115.

111. Morales, A.E., E.S. Mora, and U. Pal, *Use of diffuse reflectance spectroscopy for optical characterization of un-supported nanostructures.* Revista Mexicana de Fisica S, 2007. **53**(5): p. 18.

112. Cun, W., et al., *Preparation, characterization and photocatalytic activity of nano-sized ZnO/SnO< sub> 2</sub> coupled photocatalysts.* Applied Catalysis B: Environmental, 2002. **39**(3): p. 269-279.

113. Yakuphanoglu, F., *Electrical characterization and device characterization of ZnO microring shaped films by sol–gel method.* Journal of Alloys and Compounds, 2010. **507**(1): p. 184-189.

114. Sato, N., et al., *Effect of particle size reduction on crack formation in electrophoretically deposited YBCO films.* Physica C: Superconductivity, 2001. **357**: p. 1019-1022.

115. Boccaccini, A., U. Schindler, and H.-G. Krüger, *Ceramic coatings on carbon and metallic fibres by electrophoretic deposition.* Materials Letters, 2001. **51**(3): p. 225-230.

116. Wang, S. and R.A. Dryfe, *Graphene oxide-assisted deposition of carbon nanotubes on carbon cloth as advanced binder-free electrodes for flexible supercapacitors.* Journal of Materials Chemistry A, 2013. **1**(17): p. 5279-5283.

117. Fan, Z. and J.G. Lu, *Zinc oxide nanostructures: synthesis and properties.* Journal of Nanoscience and Nanotechnology, 2005. **5**(10): p. 1561-1573.

118. Wang, Y., I.-C. Leu, and M.-H. Hon, *Dielectric property and structure of anodic alumina template and their effects on the electrophoretic deposition characteristics of ZnO nanowire arrays.* Journal of applied physics, 2004. **95**(3): p. 1444-1449.

119. Yang, Y., et al., *Size dependence of dielectric constant in a single pencil-like ZnO nanowire.* Nano letters, 2012. **12**(4): p. 1919-1922.

120. Penn, S.J., et al., *Effect of porosity and grain size on the microwave dielectric properties of sintered alumina.* Journal of the American Ceramic Society, 1997. **80**(7): p. 1885-1888.

121. Xiong, G., et al., *Photoluminesence and FTIR study of ZnO nanoparticles: the impurity and defect perspective.* physica status solidi (c), 2006. **3**(10): p. 3577-3581.

122. Wang, X., et al., *Preparation and characterization of ZnO hollow spheres and ZnO-carbon composite materials using colloidal carbon spheres as templates.* The Journal of Physical Chemistry C, 2007. **111**(18): p. 6706-6712.

123. Liu, B. and H.C. Zeng, *Hollow ZnO microspheres with complex nanobuilding units.* Chemistry of Materials, 2007. **19**(24): p. 5824-5826.

124. Sahu, R.K., et al., *Microwave-Assisted Synthesis of Magnetic Ni Wire from a Metal− Organic Precursor Containing Ni (II) and Triethanolamine.* Crystal Growth and Design, 2008. **8**(10): p. 3754-3760.

125. Kajbafvala, A., et al., *Nanostructure sword-like ZnO wires: rapid synthesis and characterization through a microwave-assisted route.* Journal of Alloys and Compounds, 2009. **469**(1): p. 293-297.

126. Wang, J. and D. Bai, *Network TiO2 Nanowires for Dye-Sensitized Solar Cells.* Journal of The Electrochemical Society, 2014. **161**(5): p. H265-H268.

127. Castro-Hurtado, I., et al., *Properties of NiO sputtered thin films and modeling of their sensing mechanism under formaldehyde atmospheres.* Acta Materialia, 2013. **61**(4): p. 1146-1153.

128. Hotovy, I., et al., *Preparation of nickel oxide thin films for gas sensors applications.* Sensors and Actuators B: Chemical, 1999. **57**(1): p. 147-152.

129. Brilis, N., et al., *Development of NiO-based thin film structures as efficient H 2 gas sensors operating at room temperatures.* Thin Solid Films, 2007. **515**(24): p. 8484-8489.

130. Li, G., et al., *A facile synthesis method for Ni (OH) 2 ultrathin nanosheets and their conversion to porous NiO nanosheets used for formaldehyde sensing.* RSC Advances, 2012. **2**(33): p. 13018-13023.

131. Rao, B.B., *Zinc oxide ceramic semi-conductor gas sensor for ethanol vapour.* Materials Chemistry and Physics, 2000. **64**(1): p. 62-65.

132. Jinkawa, T., et al., *Relationship between ethanol gas sensitivity and surface catalytic property of tin oxide sensors modified with acidic or basic oxides.* Journal of Molecular Catalysis A: Chemical, 2000. **155**(1): p. 193-200.

133. Hongsith, N., et al., *Ethanol sensor based on ZnO and Au-doped ZnO nanowires.* Ceramics International, 2008. **34**(4): p. 823-826.

134. Zhang, Y., et al., *Fabrication and ethanol-sensing properties of micro gas sensor based on electrospun SnO 2 nanofibers.* Sensors and Actuators B: Chemical, 2008. **132**(1): p. 67-73.

135. Cho, N.G., et al., *Gas sensing properties of p-type hollow NiO hemispheres prepared by polymeric colloidal templating method.* Sensors and Actuators B: Chemical, 2011. **155**(1): p. 366-371.